Synthesis, Characterization and Electronic Structure Modulation of Perovskite Oxides for Photocatalytic Applications

A Dissertation Submitted to the
Indian Institute of Technology Guwahati
As Partial Fulfillment for the Degree of

DOCTOR of PHILOSOPHY

by

Anindya Sundar Patra

Department of Chemistry
Indian Institute of Technology Guwahati
Guwahati – 781039, Assam, India

May 2018

Synthesis, Characterization and Electronic Structure Modulation of Perovskite Oxides for Photocatalytic Applications

A Dissertation Submitted to the
Indian Institute of Technology Guwahati
As Partial Fulfillment for the Degree of

DOCTOR of PHILOSOPHY

by

Anindya Sundar Patra

Roll No. 126122032

Department of Chemistry
Indian Institute of Technology Guwahati
Guwahati – 781039, Assam, India
May 2018

STATEMENT

I hereby declare that this thesis entitled, "**Synthesis, Characterization and Electronic Structure Modulation of Perovskite Oxides for Photocatalytic Applications"** is the outcome of research work carried out by me under the supervision of Prof. Mohammad Qureshi, at the Department of Chemistry, Indian Institute of Technology Guwahati, Assam, India, for the award of the degree of Doctor of Philosophy.

In keeping with the general practice of reporting scientific observations, due acknowledgement has been made whenever work described here has been based on the findings of other investigators. To the best of my knowledge, the set of work described on this thesis is original and has not been submitted elsewhere for any degree or diploma.

Guwahati
May, 2018

Anindya Sundar Patra
(Candidate)
Department of Chemistry
IIT Guwahati
Guwahati- 781039, Assam
India

Dr. Mohammad Qureshi
Professor
Department of Chemistry
Indian Institute of Technology, Guwahati
781039 – India
Tel: +91 – 361 – 2582320
Fax: +91 – 361 – 2582349
Email: mq@iitg.ernet.in

Certificate

Certified that the work described in this thesis entitled "**Synthesis, Characterization and Electronic Structure Modulation of Perovskite Oxides for Photocatalytic Applications**" by Mr. Anindya Sundar Patra, Department of Chemistry, Indian Institute of Technology Guwahati has been carried out under my supervision and has not been submitted elsewhere for a degree or diploma.

Guwahati
May 2018

Mohammad Qureshi
(Thesis supervisor)
Department of Chemistry
IIT Guwahati
Guwahati – 781039, Assam
India

ACKNOWLEDGEMENTS

This thesis might not have seen through its completion unless I had the direct or indirect support, grace, and inspiration of many persons around me. Words are inadequate to express my gratitude to many people with whom I have spent memorable times and I wish to express few words of appreciation to all the persons who actually made this thesis a reality and made my stay at IITG a treasured experience.

First and foremost, with the deepest sense of gratitude, I wish to express my sincere thanks to my supervisor, Prof. Mohammad Qureshi for supporting me throughout this thesis with his adept guidance, encouragement, constructive criticism, innovative and technical ideas. I am grateful to him for giving me the freedom to pursue my own ideas and I find myself privileged to work with him.

I thank my doctoral committee members, Dr. Chivukula V. Sastri, Prof. Parameswar Krishnan Iyer, Prof. Aditya Narayan Panda, and Dr. Uttam Manna for periodically assessing my work and the insightful advice and helpful suggestions during the Ph.D. course. I am grateful to the faculty and staff members at the Department of Chemistry, IIT Guwahati for providing a wonderful working environment during this period.

I would like to thank my all my senior group members, Dr. Dipankar Barpuzary, Dr. Tridip Ranjan Chetia, Dr. Momina Khannam, and my present group members Shaad, Avishek, Tushar, Adit, Suhaib, Moite, Sourabh and Manoj for their timely help, cooperation and for creating an enjoyable atmosphere in the lab. I am thankful to Gaurangi for her constant support, assistance in experiments, and carefully correcting my manuscripts.

I wish to express my sincere gratitude to IIT Guwahati for all the facilities that were made available to me and the Ministry of Human Resource Development (MHRD), India for the financial support. I would like to thank Department of Physics, and Department of Chemical engineering of IIT Guwahati; ACMS IIT Kanpur for

assistance and instrumentation facilities. I am thankful to scientific officers and all the operators of various instruments at Central Instruments Facility (CIF), IITG for their time and help in characterizing my samples.

I want to thank Dr. Mahuya De and Dr. N. Vinothkumar, Department of Chemical Engineering, IITG, for their help in photocatalytic studies in the early stage of my research. I also thank Prof. Shane Ardo, (University of California, Irvine) and Dr. Ranjan Kumar Sahu (CSIR-National Metallurgical Laboratory, Jamshedpur, India) for XPS analysis of my samples and their valuable discussions and inputs in my work.

Stay at IITG has been a memorable part of my life from both professional and personal point of view. I have met many wonderful people here. I feel lucky and treasure my friendship with Dr. Utpal Nath, Dr. Shubhadip Das, Dr. Subhashis Jana, Dr. Ashim Paul, Uday for the wonderful moments we have spent together. I also owe my obligations to Dr. Deep Joshi, Hiranya, Dr. Suman Kalyan Das, Dr. Sanjib Nayak, Ram, Bibhash da, Rana, Prasenjit, Supriyo, Avik, my batch mates, seniors, and juniors of Ph. D. fraternity of the Chemistry department for their help and support.

I take this opportunity to express my sincere thanks to all my teachers starting from primary to masters for helping and motivating me in every respect of life and academics. Their teaching and guidance actually an asset in every step of my life.

Last but not the least; I am indebted to my parents and family members for their blessings, unconditional love, and encouragements. Their constant support and care allow me to pursue my dreams. Without them, this thesis would never have been written.

Anindya

Dedicated to
My
Beloved Parents

Thesis Title:	Synthesis, Characterization and Electronic Structure Modulation of Perovskite Oxides for Photocatalytic Applications
Name of the Candidate:	Mr. Anindya Sundar Patra
Registration Number:	126122032
Thesis Supervisor:	Prof. Mohammad Qureshi
Department:	Chemistry
Institute:	Indian Institute of Technology Guwahati, Assam-781039

Chapter 1 presents a literature review, basic concepts, and challenges of photocatalytic water splitting and dye degradation. A brief overview of the synthesis and band engineering of photocatalysts/perovskite oxides and their application in photocatalytic activities are included. Based on the literature review, the motivation behind the thesis has been defined.

Chapter 2 describes standard synthetic protocols used in the thesis for different perovskite oxides and their composites with carbonaceous materials via solid-state, hydrothermal and chemical oxidation routes. A detailed description of our photocatalytic reactor and gas detection are included. Experimental water oxidation/reduction and dye degradation procedure are discussed.

Chapter 3 presents the doping of $LaMnO_3$ (LMO) with ruthenium at different levels and understanding the change in the crystal and electronic structure, thereby correlating them to photocatalytic properties. Owing to the similarity in the redox levels and their sizes, ruthenium has been chosen to alter the electronic structure of LMO and studies their structure-property correlation in terms of their photocatalytic activity. In octahedral geometry, the ionic radii of Mn (III) and Mn (IV) are 65 pm and 52 pm respectively, whereas that of Ru (IV) and Ru (V) are 62 pm and 56 pm. The redox values for Mn (III) ↔ Mn (IV) is 1.02 eV and that of Ru (IV) ↔ Ru (V) is 1.07 eV. In this work, we have doped Ru in Mn site of LMO and studied their efficacy in photocatalytic oxygen production from water and dye degradation. Ruthenium doping alters the crystal structure of the parent LMO due to the induced chemical pressure of larger ion, Ru (IV), which facilitates the bond angle close to 180° among Mn (III)–

O–Mn (IV) plane resulting in an easy extraction of population leading to the enhanced photocatalytic activity. Rietveld refinements reveal that the parent compound LMO crystallizes in rhombohedral phase, while with an increase in the doping concentration of ruthenium, the phase of the compounds changed from rhombohedral to cubic. Percentage contribution of each phase has been estimated using the sixth-order polynomial and pseudo-Voigt function. Structure-property correlation of the compounds is presented based on Rietveld refinement combined with the experimental data. As-prepared compounds show an efficient photocatalytic oxygen gas production from water without using any co-catalyst or sacrificial reagents. Among the five compositions, $LaMn_{0.7}Ru_{0.3}O_3$ shows highest O_2 production efficiency (4.73 mmol/g/h) with ~7.43% of AQY value. These ruthenium doped compositions also exhibit superior dye degradation properties, studied by taking the industrial dye, methyl orange (MO) as the model compound. This increase in photocatalytic efficiency of the materials is due to the presence of phase barrier between rhombohedral and cubic phases, which reduces charge carrier recombination, and the decrease in the band gap of the materials when doped with Ru.

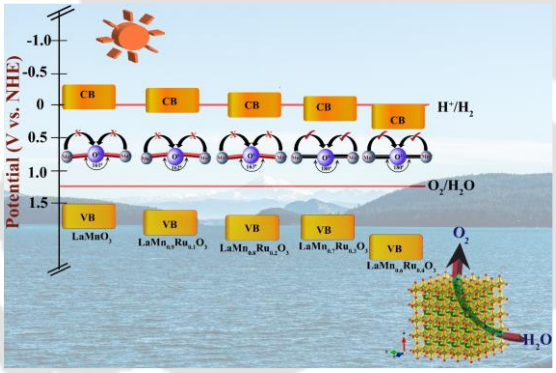

Phys. Chem. Phys. Chem. **2017**, *19*, 12167.

Chapter 4 presents the doping of lanthanum manganite with strontium at different levels and understanding the change in the electronic structure, thereby correlating them to photocatalytic properties. The larger size of Sr than that of La induces internal chemical pressure in the lattice, leading to a change in phase. Changes in the electronic structure with doping of Strontium has been studied using powder X-ray and X-ray Photoelectron Spectroscopy (XPS). XPS analysis shows a mixed valent Mn (III) / Mn (IV) in both parent and the doped systems, $LaMnO_3$ and $La_{0.7}Sr_{0.3}MnO_3$. As Mn (III) is known to show a strong

Jahn – Teller effect, an electron from Mn (III) will favorably transfer from Mn (III) to Mn (IV), leading better transport of electrons in the system, making it conductive at room temperature. From powder X-ray diffraction data we have found that parent compound crystallizes in rhombohedral phase. $LaMnO_3$ crystallizes in rhombohedral phase when it has oxygen non-stoichiometry in its lattice and to neutralize the charge imbalance, a fraction of Mn (III) is converted to Mn (IV). From four probe resistivity measurements, we have found that $La_{0.7}Sr_{0.3}MnO_3$ has the lowest resistivity of 0.118 Ω cm among all synthesized compounds. It is well known that Mn 3d orbitals in the ground state has a strong contribution to the electronic structure and thereby altering the manganese electronic state one can influence its conducting properties. We have observed that with progressive doping, a strong correlation between structure and photocatalytic properties exists. A 30 atom% Sr-doped lanthanum manganite shows maximum photocatalytic efficacy owing to the favorable Mn(III)–O–Mn(IV) hopping pathway, leading to the conductivity, as proposed by famous Zener double exchange model. Further, the efficacy of $La_{1-x}Sr_xMnO_3$ (x = 0.0 – 0.5) systems can be enhanced by coupling with 1 wt% of graphene oxide (GO). Respective mechanism and photocatalytic evaluation of the compositions are reported and documented. The calculated AQY values of $La_{0.7}Sr_{0.3}MnO_3$ is ~7% whereas $La_{0.7}Sr_{0.3}MnO_3$ – GO is ~8%.

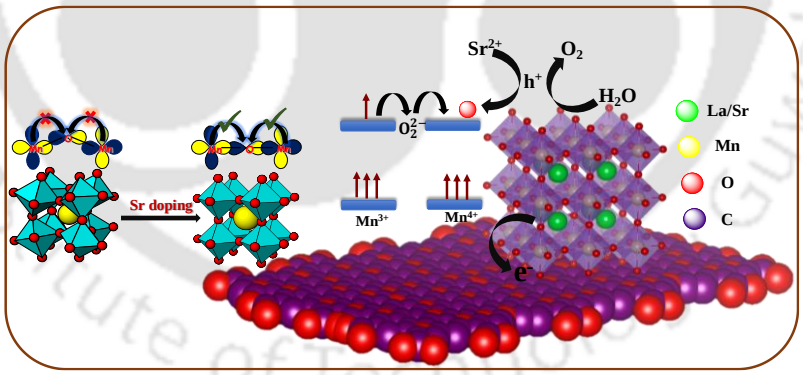

Mater. Lett. **2014**, *131*, 125.

Chapter 5 presents the effect of Ce doping and oxygen vacancies in efficient hydrogen production of $BaZrO_{3-\delta}$ (BZO). Because of the low in cost and ability to form stable redox couple Ce (III)/Ce (IV), which have diverse optical properties and high efficiency in photocatalytic processes, we have modulated the electronic structure of BZO by Ce doping

in the site of Zr. In this chapter, the influence of cerium doping and oxygen vacancies on the photocatalytic properties of BZO hollow nanospheres has been studied. Compounds synthesized by a template-free route are composed of hollow nanospheres generated by Ostwald ripening of spherical nanospheres, which are formed by agglomeration of nanoparticles. The high alkaline condition during the hydrothermal condition leads to the formation of oxygen vacancies and lattice disorder in the compounds, confirmed by UV-visible diffuse reflectance spectroscopy (UV-Vis DRS), X-ray photoelectron spectroscopy (XPS) and electron spin resonance (ESR) analysis. Combination of oxygen vacancies, lattice disorder and progressive doping of Ce onto BZO, $BaZr_{1-x}Ce_xO_3$ (x = 0.0 – 0.04), creates additional energy levels below the conduction band of BZO thereby reducing its band gap. The photocatalytic efficacy of the compounds is examined by H_2 generation from water reduction. In this study, $BaZr_{0.97}Ce_{0.03}O_3$ shows the highest efficiency (823 $\mu molh^{-1}g^{-1}$) in photocatalytic H_2 production among all five synthesized samples. The synergistic effect of lowering of band gap due to Ce doping and the presence of oxygen vacancies are the reasons behind the enhanced photocatalytic efficacy of $BaZr_{1-x}Ce_xO_3$ (x = 0.0 – 0.04) under UV-visible light irradiation.

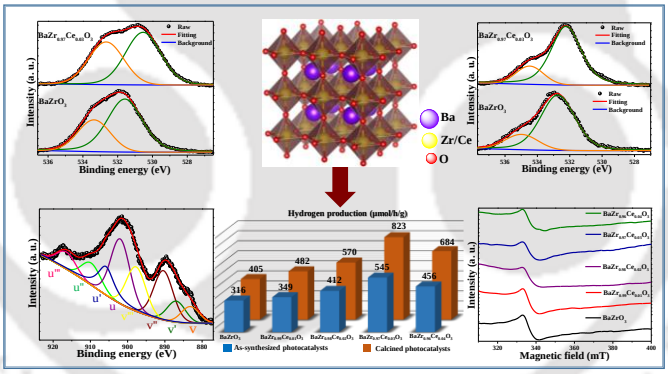

(Manuscript under communication)

Chapter 6 presents the effect of carbon dots (CDs) and presence of oxygen vacancies on the photocatalytic properties of hydrothermally synthesized $BaZrO_{3-\delta}$ (BZO) hollow nanospheres. Making composites with a different weight percentage of CDs enhance the light absorption onset of the catalysts. In addition, the high charge transfer capacity of CDs reduce the charge carrier recombination of BZO. The photocatalytic efficacy of the compounds is examined by photocatalytic H_2 generation from water reduction and methylene blue (MB) dye degradation. In this study, 3 wt% CD_BZO (3C_BZO) shows the highest efficiency (670

$\mu molh^{-1}g^{-1}$) in photocatalytic H_2 production and dye degradation among all five synthesized samples with a different loading percentage of CDs. The synergistic effect of enhancement of light absorption along with high photogenerated charge carrier transfer efficiency in the presence of CDs and the presence of oxygen vacancies are the reasons behind the enhanced photocatalytic efficacy of *x* wt. % CDs_BZO ($x = 0 – 4$) under UV-visible light.

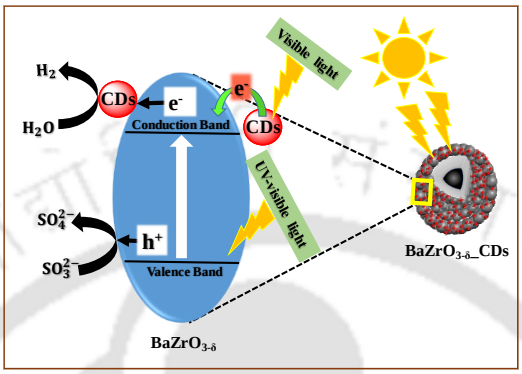

(Manuscript under communication)

Chapter 7 presents a brief overview and future scope of this thesis.

Chapter 1

Introduction

This Chapter describes the basic concepts of the photocatalytic water oxidation, water reduction and dye degradation. The number of possible ways to enhance the photocatalytic water oxidation and water reduction efficiency of semiconductor photocatalysts are discussed. Brief discussions about perovskite oxides and literature survey on their photocatalytic water oxidation and water reduction are also included.

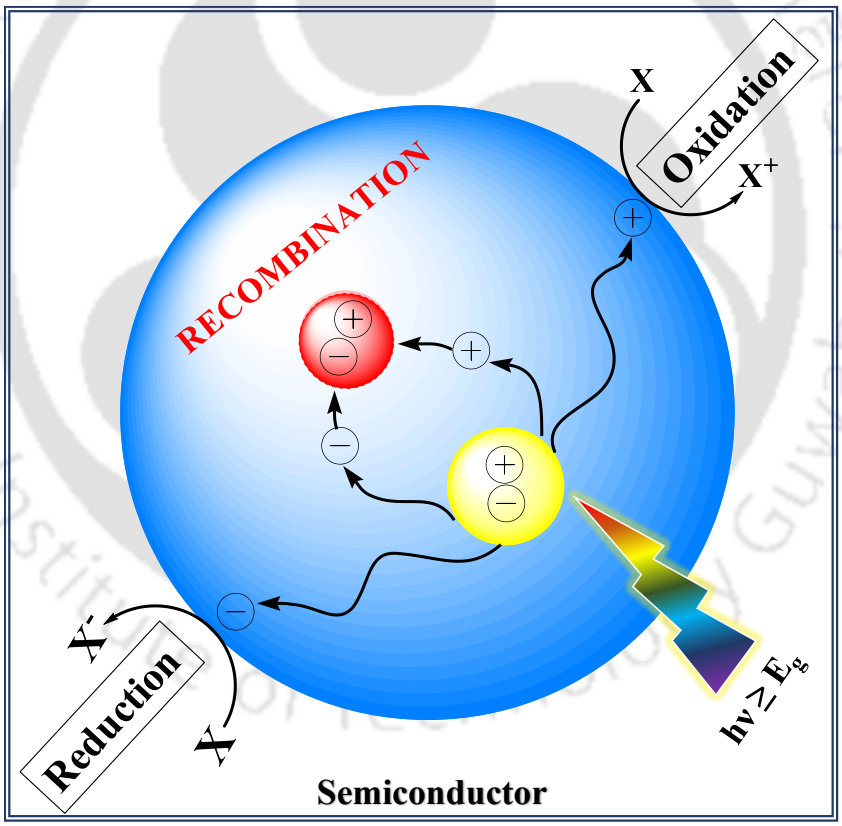

1.1 AN OVERVIEW OF ENERGY DEMAND AND HYDROGEN PRODUCTION

Since the inception of fire to the beginning of the industrial age with the invention of steam engine, fossil fuels or carbonaceous materials are the main resources of the power source and human development. In the present century, increase in global population and rising living standard ramps up energy demands. In 2015, total world energy consumption was 575 quadrillion British thermal units (Btu) whereas in 2040 the projected energy consumption will be around 736 quadrillion Btu.[1] Figure **1.1(A)** shows the trend of total global energy consumption and estimated energy demand in near future and Figure **1.1(B)** shows the total global energy supply by fuel in 2015.

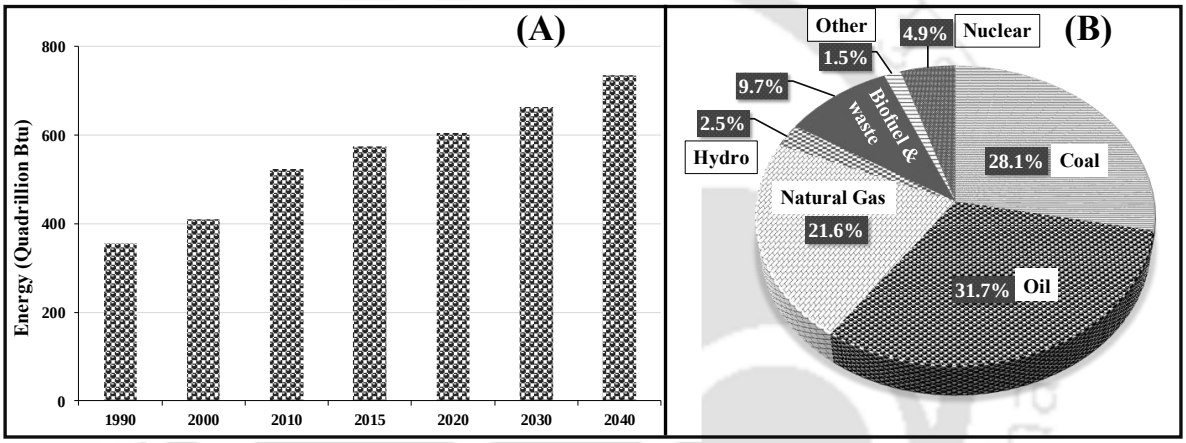

Figure 1.1 (A) Represents the present trend of global energy consumption (in quadrillion British thermal units) and estimated global energy demand in near future and (B) shows the total global energy supply by fuel in 2015. (Data adapted from: (A) http://www.eia.gov/forecasts/ieo/ and (B) http://www.iea.org/statistics/)[1, 2]

It is projected that 77% of the energy demand of mankind in 2040 will primarily be supplied by fossil fuels.[1] The burning of fossil fuels emits greenhouse gases such as; CO_2 and several pollutants to the atmosphere, which are major threats to the environment. On the other hand, fossil fuels are depleting very fast and to alleviate the rising energy demand and threats posed by increasing pollution level, improvement of environmentally benign renewable energy sources are keenly sought. Among several renewable energy sources, hydrogen is one of the most promising energy carriers due to its very high energy content per unit mass and gives away only heat and water when burned. Hydrogen can be generated in several ways and according to the used raw materials; the processes can be sub-divided into two main categories, such as fossil fuels and renewable energies. From fossil fuels, hydrogen can be

generated by hydrocarbon reforming and pyrolysis methods and from renewable sources, hydrogen is produced mainly by electrochemical, photochemical, thermochemical or biological methods from water and biomass.[3, 4] Presently, almost 95% of global hydrogen production is obtained from fossil fuels and steam reforming process is the most used method to produce hydrogen from fossil fuels, whereas only 4% is produced from electricity and only 1% is produced from biomass.[5, 6]

Hydrogen produced from hydrocarbon reforming needs expensive setup, high temperature and produce harmful CO_2 or CO gases. Hence, in order to produce hydrogen from the environmentally benign process, photochemical processes are one of the viable solutions. In photochemical processes, sunlight is one of the main components and the Sun is a most profuse source of energy on earth. The energy reaches to the earth surface in 1 h is more than the total energy requirement of the planet in one year (17.4 TW in 2017).[7, 8] Among photochemical processes, photocatalytic hydrogen production from water is fascinating due its simple setup, high activity, and low cost.

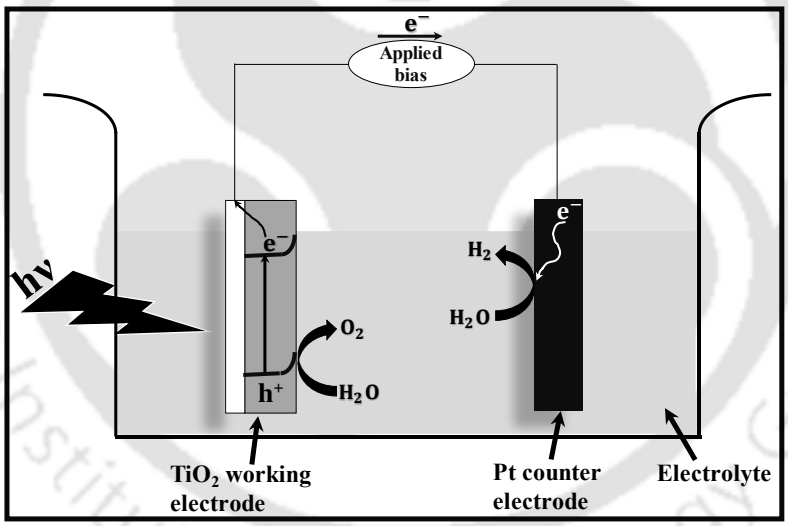

Figure1.2 Schematic representation of a photoelectrochemical water splitting cell.[9]

The seminal work on photoelectrochemical water splitting was reported by Honda and Fujishima in 1972.[9] They have used n-type TiO_2 anode and Pt dark cathode in aqueous solution. When UV light shined the TiO_2 electrode, photogenerated electron and holes are produced. The water was simultaneously oxidized and reduced by the holes on the TiO_2 electrode and the electrons on the Pt electrode, respectively, with the assistance of some applied bias. This whole process is represented schematically in Figure **1.2**. In 1980 first report on powdered photocatalytic water splitting with stoichiometric H_2 and O_2 evolution

was reported by Lehn and co-workers, Domen and co-workers and Sato and White.[10 – 12] Since this breakthrough, a numerous research have been conducted in semiconductor-based water splitting in order to explore a possible solution for rising world energy crisis.[13, 14]

1.2 GENERAL MECHANISM FOR SEMICONDUCTOR PHOTOCATALYSIS AND WATER SPLITTING

Semiconductors are made of non-overlapping valence band and conduction band and there is a distinct difference between these two levels, called band gap of the semiconductor. When a semiconductor is illuminated by light with an energy equal or more than its band gap energy then electrons from the valence band of the semiconductor will get excited and move to its conduction band leaving an equivalent number of holes behind in the valence band. This phenomenon is called photoexcitation of a semiconductor. These photogenerated charge carriers are unstable and have high tendency to recombine, giving away the input energy in the form of heat energy without any chemical reaction. Nonetheless, the photogenerated charge carriers with suitably high lifetime and mobility can get separated and reach the surface of the semiconductor by avoiding recombination where they can undergo several redox reactions with the surface adsorbed species, such as water or other organic and inorganic moieties. These redox reactions are the preliminary steps in photocatalytic water splitting and organic dye degradation.[7] Like bulk charge carrier recombination, separated electrons and holes can get recombined near semiconductor surface also. A schematic of the general mechanism for semiconductor photocatalysis is illustrated in Figure **1.3**.

In heterogeneous photochemical water splitting, the main component is the UV–visible light absorbing material and the photocatalysts can be used in two different reaction setups with identical basic principle – (a) photoelectrochemical cells and (b) powdered photocatalytic systems. In photoelectrochemical water splitting, two electrodes named as- working electrode and counter electrode are dipped into an aqueous electrolyte solution. The working electrode containing a film or layer of the photocatalyst is exposed to light. While, in powdered photocatalytic water splitting, photocatalysts are suspended in water and the aqueous suspension is irradiated with suitable light. Hence, in powdered photocatalysis configuration each and every photocatalyst particles act as microphotoelectrodes in which both water oxidation and reduction reactions are taking place. Although in powdered photocatalytic water splitting process it is difficult to separate the produced H_2 and O_2 gases which may initiate the back reaction, still this process is advantageous over photoelectrochemical water

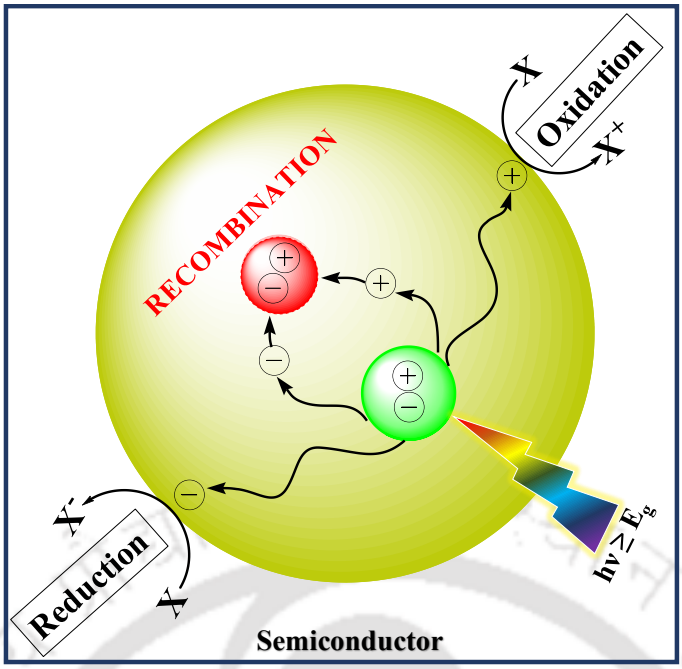

Figure 1.3 Graphical representation of the general mechanism for semiconductor photocatalysis.

splitting as the former process is easy to perform for large-scale application due the simplicity and less expensive reaction setup than the later process.

Thermodynamically, overall water splitting into H_2 and O_2 involving the transfer of multiple electrons, is an uphill process as it requires high positive change in Gibb's free energy ($\Delta G°$) of 237 $kJmol^{-1}$ or 1.23 eV.[13]

$$H_2O \longrightarrow H_2 + \frac{1}{2} O_2 \; ; \; \Delta G° = +237 \text{ kJ/mol}$$

To overcome this high-energy barrier in water splitting, photon energy and suitable semiconductors are utilized. Therefore, the minimum required band gap of the photocatalyst should be ≥ 1.23 eV ($\lambda \leq 1000$ nm) to generate H_2 and O_2 from overall water splitting. Hence, to utilize the visible light of the solar spectrum, the band gap of the material should be less than 3 eV. The overall water splitting process is shown below:

$$\text{Photocatalyst} + \text{light} \longrightarrow h^+_{VB} + e^-_{CB}$$

$$\text{Oxidation: } H_2O + 2h^+_{VB} \longrightarrow 2H^+ + \frac{1}{2}O_2$$

$$\text{Reduction: } 2H^+ + 2e^-_{CB} \longrightarrow H_2$$

$$\text{Overall reaction: } H_2O \longrightarrow H_2 + \frac{1}{2} O_2$$

In powdered photocatalytic water splitting, employed photocatalyst materials must be able to satisfy some important properties such as- (1) absorption ability of suitable solar energy to produce photogenerated charge carriers and separation of these charge carriers, (2) appropriate valence band and conduction band positions for water splitting, (3) minimum bulk and surface charge carrier recombination, and (4) photostability and stability in aqueous solution.[8] Apart from these above-mentioned properties, a photocatalyst must have few additional characteristics for efficient water splitting, such as suitable crystal structure, high crystallinity, high surface area, optimized particle size etc. It is known that different crystal structure of a material has different activity towards water splitting. For an example, anatase form is more efficient than rutile TiO_2 in photocatalytic water splitting under same conditions.[14] A photocatalyst with high crystallinity has less number of defect states, which act as charge carrier recombination sites, in its lattice. A high surface area can offer more reactive sites for surface redox reactions and can enhance the efficiency of a photocatalyst in photocatalytic process. Another way to enhance the efficiency of a photocatalyst can be achieved by reducing its particle size. In smaller particles, charge carriers have to travel comparatively less distance to reach the photocatalyst surface during their lifetime to initiate the surface redox reactions than that of their larger counterparts.[15] By adopting this approach, the surface recombination of the charge carriers can be minimized. The particle size of the photocatalyst should be smaller than the charge carrier diffusion length to have effective charge carrier dynamics.[16] A schematic illustration of photocatalytic water splitting on semiconductor photocatalyst is shown in Figure **1.4**.

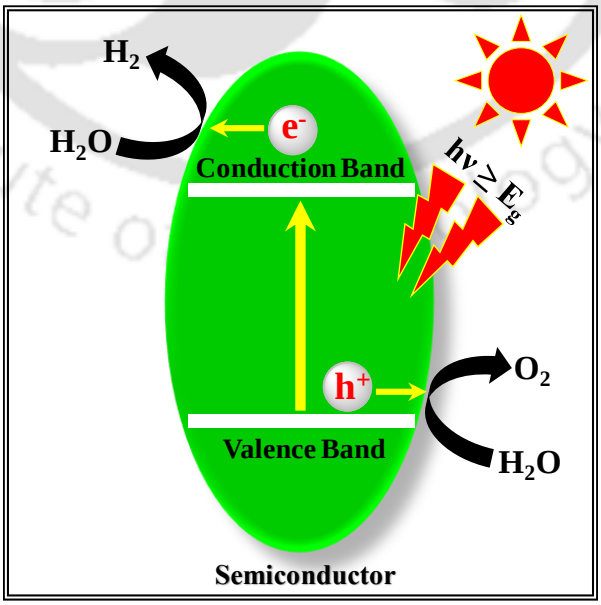

Figure 1.4 Schematic of photocatalytic water splitting by a semiconductor photocatalyst.

1.2.1 Photocatalytic H_2 or O_2 Evolution from Water Reduction or Water Oxidation

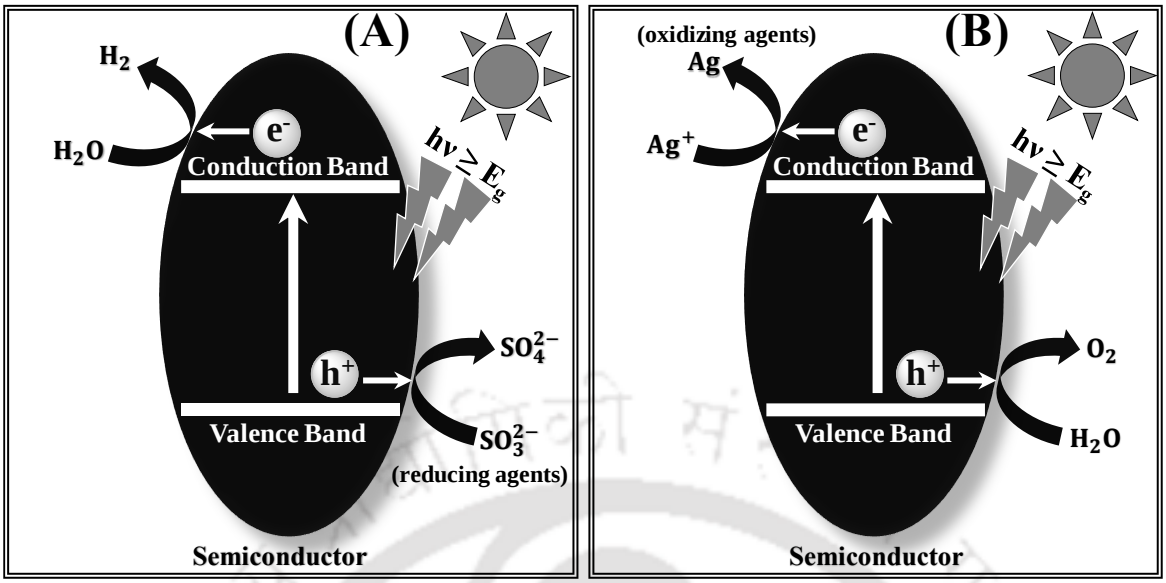

Figure 1.5 (A) Photocatalytic hydrogen production and (B) photocatalytic oxygen production by semiconductors in presence of sacrificial reagents.

In artificial photosynthesis a photocatalyst can produce O_2 and H_2 from water if the valence band maxima of the material is more positive than the redox potential of H_2O/O_2 (1.23 V vs. NHE) and the conduction band minima of the material is more negative than the redox potential of H^+/H_2 (0 V vs. NHE). The photocatalytic activity of a photocatalyst is often evaluated in the presence of some sacrificial reagents to produce either H_2 or O_2. These sacrificial reagents could be electron acceptors (oxidizing reagents viz. Ag^+, Fe^{3+}) or hole acceptors (reducing agents, viz. alcohol, sulfides, sulfites, etc.). When hole-scavenging reagents are used in water reduction reaction, the photogenerated holes are consumed by them, thereby reduce the charge carrier recombination probability between electrons and holes and in turn enhances the H_2 evolution. Similarly, when electron scavenging reagents are used in water oxidation reaction, the photogenerated electrons are consumed by them and thereby reducing the charge carrier recombination probability between electrons and holes and in turn enhances the O_2 evolution. The schematic for the production of H_2 and O_2 in presence of sacrificial reagents are illustrated in Figure **1.5**. Although, the photocatalytically H_2 and O_2 generation from water in the presence of sacrificial reagents are considered as half-reactions or semi reactions of water splitting, these reagents are generally used to assess the catalytic activity of the photocatalysts.[17 – 20]

1.2.2 Importance of O_2 Production from Photocatalytic Water Splitting

Among these above mentioned two half-reactions, photocatalytic water oxidation or O_2 generation is one of the most challenging and even termed as the "bottleneck" of overall photocatalytic water splitting efficiency.[21] The main challenge behind the photocatalytic water oxidation is the need of very high activation energy and four positively charged holes at a point of time. Hence, it is very crucial to enhance O_2 evolution to boost the photocatalytic H_2 evolution efficiency.

1.3 STRATEGIES TO DEVELOP EFFICIENT PHOTOCATALYSTS

A wide range of metal oxide and perovskite oxide materials have been explored in recent past for photocatalytic water splitting. Among them, some are UV light active due to their large band gap and some are visible light active because of their small band gap. The contribution of UV light in the solar spectrum is only ~ 4 – 6%, whereas visible light contributes almost 43% of the solar spectrum. Due to this reason, researchers are very keen to develop materials which have their absorption onset in the visible region of the solar spectrum. In past few decades, several methods have been developed to design and synthesize efficient visible light active photocatalysts. The mostly used methodologies are-

1. Band gap engineering of a photocatalyst by metal or non-metal ion doping
2. Surface sensitization
3. Band gap engineering by synthesizing intermediate band gap material from a mixture of wide band gap and narrow band gap materials
4. Enhancing H_2 and O_2 evolution by introducing cocatalysts, etc.

1.3.1 Band Gap Engineering of a Material by Metal or Non-metal Ion Doping

Band gap modulation of wide band gap semiconductors is an efficient way to develop efficient visible light active semiconductors for photocatalytic water splitting. In an oxide semiconductor, the valence band is mainly derived from the 2p orbital of the oxygen atom, whereas the lower unoccupied molecular orbitals of metal cation mainly form the conduction band. A visible light active photocatalyst can be designed by doping suitable foreign elements onto a wide band gap semiconductor. When a wide band gap semiconductor is doped by metal cation, an impurity energy level is formed within the forbidden band of the semiconductor and reduce its band gap, as shown in Figure **1.6(A&B)**. Depending upon the nature of the dopant, the formed impurity energy levels can serve as either donor or acceptor level within the forbidden band gap of the semiconductor. Although the impurity levels reduce the

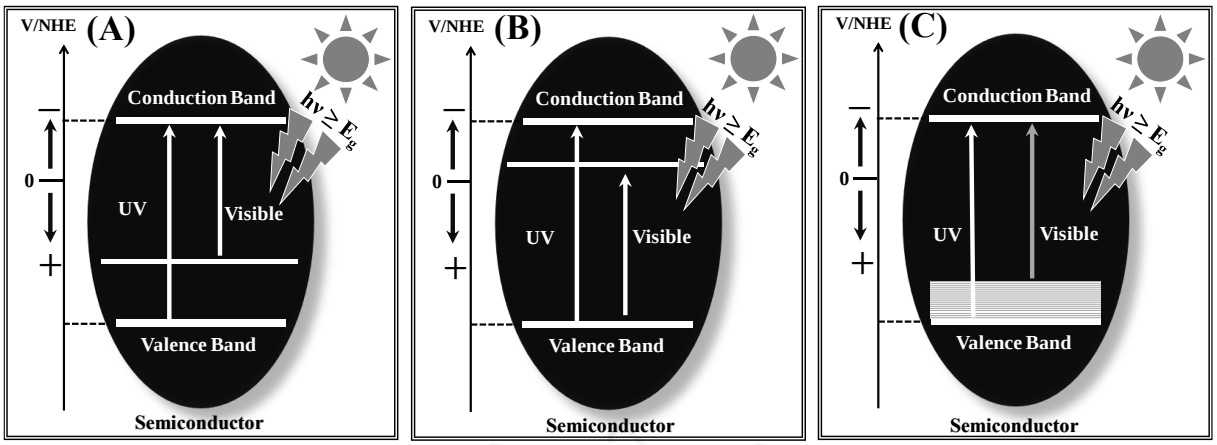

Figure 1.6 Narrowing of band gap of a wide band gap semiconductor by (A – B) cation doping and (C) anion doping.

effective band gap of a wide band gap semiconductor, sometimes these levels act as recombination sites for photogenerated charge carriers and thereby reduce the catalytic activity. Therefore, it is important to optimize the nature and extent of doping elements to design an efficient photocatalyst. A considerable amount of literature is available where enhanced photocatalytic activity has been achieved by narrowing the band gap of several wide band gap semiconductors because of cation doping. Borgarello *et al.* have shown enhanced photocatalytic hydrogen evolution from Cr^{5+} doped TiO_2.[22] In a similar fashion, enhanced photocatalytic hydrogen evolution has been reported in Ti^{3+} doped TiO_2, Cu doped ZnO, Cu doped $CaTiO_3$, Ru, Rh, Ir doped $SrTiO_3$ systems.[23 – 30]

Another methodology to develop visible light active photocatalyst is doping of non-metal ion in wide band gap semiconductor. The band gap of wide band gap oxide semiconductor can be narrowed by partially substituting oxygen atom from the semiconductor lattice by suitable non-metal ions (such as C, N. S. etc), In this method, the valence band edge of the semiconductor is upshifted due to the non-metal ion doping. Narrowing of the band gap of a wide band gap semiconductor is shown in Figure **1.6(C)**. Unlike metal ion doping, non-metal ion doping forms very less number of recombination centers and found to be more effective in photocatalysis. A number of literature are available where enhanced photocatalytic activity has been achieved by narrowing the band gap of several wide band gap semiconductors as a result of anion doping. Nishijima *et al.* has designed S doped TiO_2 photocatalyst and shown its enhanced hydrogen evolution efficiency compared to bare TiO_2.[31] In a similar way, enhanced photocatalytic hydrogen evolution has been reported in N doped TiO_2, S, N co-doped TiO_2, Ca, N co-doped $LaTiO_3$ systems.[32 – 34]

1.3.2 Semiconductor Surface Sensitization

In 1991, the seminal work on dye-sensitized solar cells by O'Regan and Grätzel has emerged a new route to design visible light active photocatalysts from wide band gap semiconductor by dye sensitization.[35 – 39] Upon light irradiation, a layer of photoexcited chromophores or dye molecules adsorbed onto the wide band gap semiconductor inject photogenerated electrons into the conduction band of the semiconductor. By this process, the population of electrons in the conduction band of the semiconductor enhances which triggers the photocatalysis process. By accepting electrons from the electron donating materials in the aqueous medium, the oxidized dye molecules are reduced and regenerated, simultaneously.[40, 41] A schematic of photocatalytic water splitting from the dye-sensitized semiconductor is shown in Figure **1.7(A)**.

Another way to design a visible light responsive wide band gap semiconductor is by making a composite with the semiconductor of narrow band gap – which has its conduction band maxima at comparatively higher negative value. Upon visible light absorption, the photoexcited narrow band gap semiconductor can inject electrons into the conduction band of the wide band gap semiconductor, resulting in high electron population in the wide band gap semiconductor. A schematic of photocatalytic water splitting from semiconductor composite is shown in Figure **1.7(B)**. In the quest to design visible light active photocatalyst for photocatalytic H_2 production from water, several semiconductor alloys have been reported in recent past, such as $BaZrO_3$-$BaTaO_2N$, $(AgNbO_3)_{0.75}(SrTiO_3)_{0.25}$, Bi_2O_3-Bi:$NaTaO_3$, Cr:$Gd_2Ti_2O_7$-$GdCrO_3$, etc.[42 – 45]

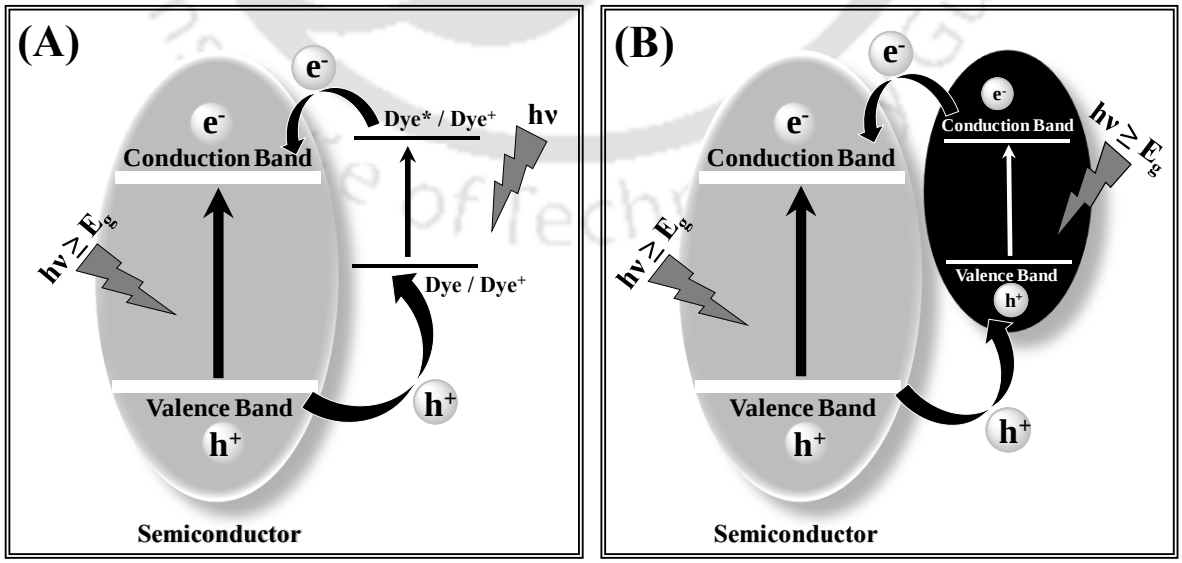

Figure 1.7 Schematic representation of semiconductor sensitization of a wide band gap semiconductor by (A) dye molecules and (B) narrow band gap semiconductor.

1.3.3 Band Gap Engineering by Designing Semiconductor Alloy

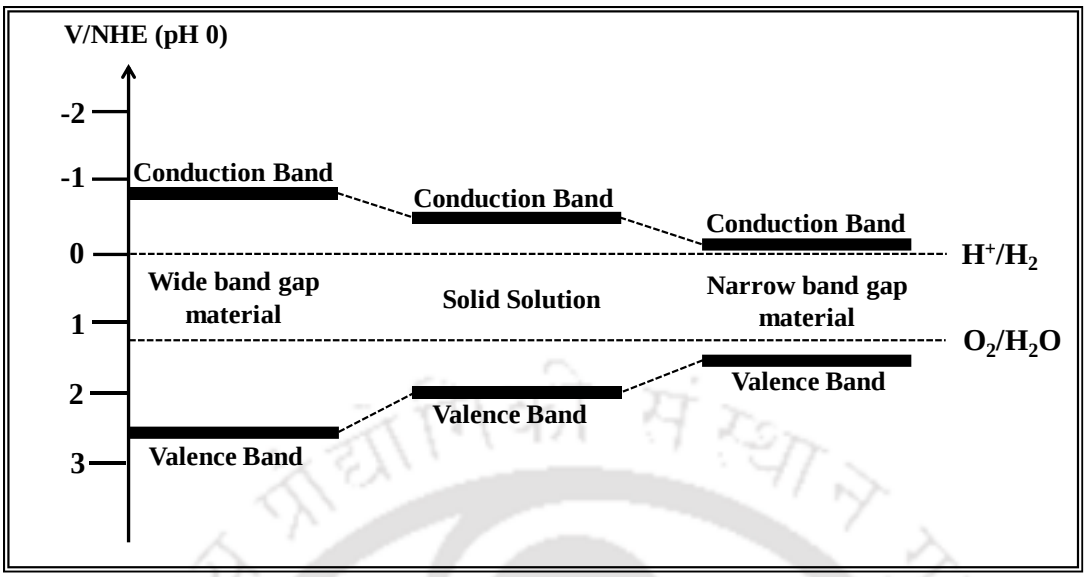

Figure 1.8 Schematic of formation of a semiconductor alloy from a wide and narrow band gap semiconductor.

The absorption onset of a wide band gap semiconductor can be extended to the visible light region by forming a solid solution with a narrow band-gap semiconductor. By mixing different proportions of wide and narrow band gap semiconductor with an alike lattice structure, the band gap and band position of the desired semiconductor solution can be optimized. [46 – 51] Figure **1.8** depicts the formation of a solid solution from a wide and narrow band gap semiconductor. Some examples of semiconductor solid solutions are – $(Ga_{1-x}Zn_x)(N_{1-x}O_x)$, $Cd_xZn_{1-x}S$, $ZnS\text{-}AgInS_2$ etc. [52 – 54]

1.3.4 Enhancing H_2 or O_2 Evolution by Introducing Cocatalysts

Instead of using some sacrificial reagents for specific half-reactions, the rate of H_2 and O_2 evolution of most of the semiconductors are not too high due to the slow surface reaction rate of the charge carriers. Hence, to increase the reaction rate of the charge carriers on the photocatalyst surface, several noble metals or metal oxides are used as an efficient cocatalyst for either H_2 or O_2 evolution. Noble metal (Pt, Pd, Ru, Rh) loaded onto the surface of a semiconductor can efficiently trap the photogenerated electrons which reached the photocatalyst surface due to the lower Fermi energy level of the noble metal compared to the photocatalyst.[55] This process reduces electron-hole recombination and increase the photocatalytic efficiency of the catalyst. Apart from noble metals, several other compounds

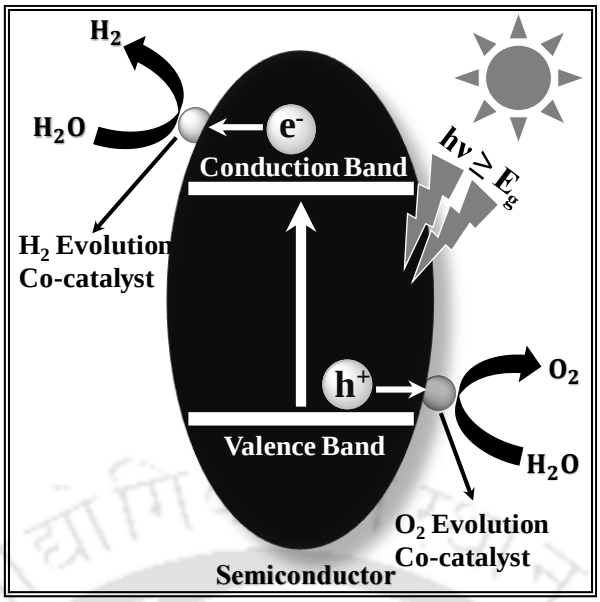

Figure 1.9 Graphical representation of photocatalytic H_2 and O_2 evolution from water splitting by employing cocatalysts.

act as efficient cocatalyst in photocatalysis process such as MoS_x, Co- Pi, FeOOH, NiO, etc.[56 – 59] A schematic of photocatalytic H_2 and O_2 evolution by employing cocatalysts onto a semiconductor material is shown in Figure **1.9**.

1.4 PEROVSKITE OXIDES

One popular class of binary metal oxides are inorganic perovskite materials having $CaTiO_3$ crystal structure generally represented as ABO_3, where A is a larger lanthanide, alkaline, or rare-earth metal ion and B is a relatively smaller transition metal ion. These materials form a three-dimensional structure. Perovskite oxides can be categorized into two classes – (1) simple perovskites (ABO_3) and (2) complex perovskites (double and layered perovskites). In ABO_3, the larger A-site cation is 12–fold coordinated with oxygen ions, resides on the corners of the unit cell and the smaller B-site cation is 6–fold coordinated with oxygen ions resides at the center of the octahedron to form a BO_6 unit with face-sharing O atoms.[60] Perovskites are stable and fine-tuning their electronic structure is facile through incorporation of appropriate atoms, by virtue of its structural tolerance.[7] The ideal perovskite oxides have the cubic phase with $Pm\bar{3}m$ space group. A unit cell of a cubic ABO_3 lattice is shown in Figure **1.10**. Most of the metal elements in the periodic table can form stable perovskite oxides. Furthermore, owing to their structural tolerance, perovskite oxides can withstand a significant amount of impurities or doping, including sub-stoichiometric oxygen in their crystal lattice, which in turn can modify their optical property and catalytic effectiveness. [61] A range of such

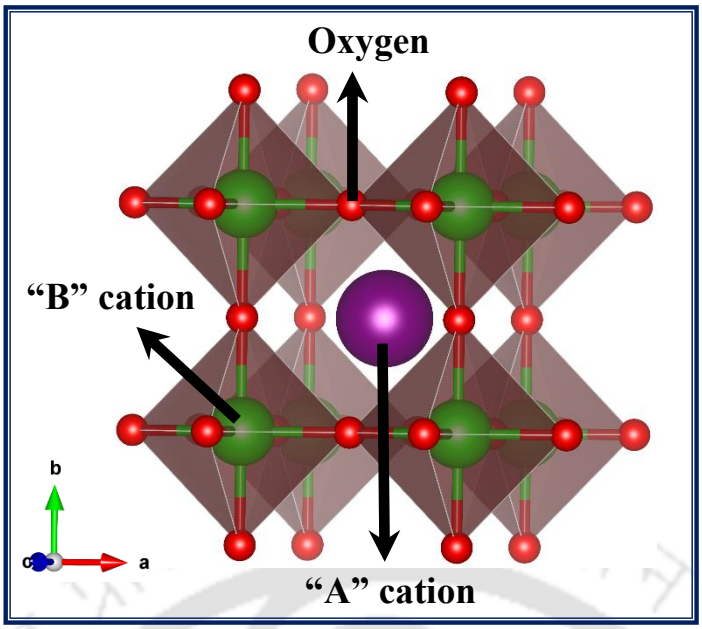

Figure 1.10 Schematic illustration of a unit cell of cubic perovskite oxide.

oxide materials can be designed with structural formula $A_{1-x}A'_xBO_3$, $AB_{1-x}B'_xO_3$ or $A_{1-x}A'_xB_{1-y}B'_yO_3$, where, A′, B′ are foreign elements with different oxidation state and ionic radii and x, y are the amount of substitutions that still satisfy the tolerance factor. [61] Tolerance factor is calculated by using the following formula

$$t = \frac{(r_A + r_O)}{\sqrt{2}(r_B + r_O)}$$

Where, r_A, r_B and r_O are the ionic radii of A, B and oxygen elements, respectively. When the value of *t* is close to 1, then ideal perovskite structure will form, whereas, when the value of *t* is less than 1, then it will form distorted perovskite structures.

Apart from the ideal cubic structure, perovskite oxides can exhibit certain degrees of distortion owing to the different ionic radii and valence of the constituent elements and ion vacancies inside their lattice, which can form different crystal phases. This lattice distortion has a direct impact on the physical and electronic structure of the material and which can also influence the charge carrier formation, transport, and catalytic activity. [62 – 65] Typically, in ABO_3, the valence band is derived mainly from the 2p orbitals of the oxygen atom and conduction band is derived from the d orbitals of B atom and the extent of hybridization of B–O depends on the electronegativity of the B atom. Hence, the nature of the B-site element essentially controls the electronic property of a perovskite oxide, hence determines the catalytic activity of the perovskite materials. The catalytic activity of a perovskite catalyst

generally determined by the bond strength of B–O bond.[66–68] In 1952, Parravano has reported the catalytic activity of $KNbO_3$, $NaNbO_3$ and $LaFeO_3$ in CO oxidation reaction and since then the use of perovskite oxides in heterogeneous photocatalysis is increased.[69, 70] Recently, numerous perovskite oxides have been synthesized and studied for their photocatalytic properties and some of those are tabulated in Table **1.1**below.

Table 1.1 Summary of photocatalytic H_2 and/or O_2 evolution efficiency of some perovskite oxides from water reduction and/or water oxidation.

Photocatalyst	Preparation Method	O_2 evolution Rate (µmol/h/g)	H_2 evolution Rate (µmol/h/g)	Sacrificial Reagent	Ref.
$NaTaO_3$	HT	—	36750	5% Methanol	71
$NaTaO_3$	SG	1000	2050	—	72
$NaTaO_3$	SS	—	13780	50% Methanol	73
La doped $NaTaO_3$	SS	9660	19800	—	74
La doped $NaTaO_3$	SS, impregnation	3470	7290	—	75
La doped $NaTaO_3$	SG, impregnation	—	26940	10% v/v Methanol	76
$NaTaO_3/Ta_2O_5$	Electrospinning, SG	—	1579	20 vol% Methanol	77
Ca, Sr, Ba doped $NaTaO_3$	SS	13380	27200	—	78
$LiTaO_3$	SS	220	430	—	79
$KTaO_3$	SS	13	29	—	79
Zr doped $KTaO_3$	SS	57.4	122.3	—	80
$AgTaO_3$	SS	63.3	138	—	81
$SrTiO_3$	SS	—	28	—	82
$SrTiO_3$	HT	—	202.6	20% Methanol	83
Cr doped $SrTiO_3$	SG, HT	—	330	20% Methanol	84
Surface Ti^{3+} doped $SrTiO_3$	HT	—	2200	25% Methanol	85
Zn doped $SrTiO_3$	SG	—	732	3% Ethanol	86
Cr/La codoped $SrTiO_3$	HT	—	1089	Methanol/NaOH	87
Cr/N codoped $SrTiO_3$	SG, HT	—	213.4	18.5% Methanol	88
Ba doped $SrTiO_3$/ CdS	ST	—	1816.8	0.35 M Na_2S + 0.25 M Na_2SO_3	89
Metal oxide/CdS/ $SrTiO_3$	Precipitation, impregnation	—	169	25% v/v Methanol	90
Ag_3PO_4/ $SrTiO_3$	HT	1316	—	0.02 M $AgNO_3$	91
$Pt/TiO_{2-x}N_x/SrTiO_3$	SG, photodipositi on	—	1800	25% Methanol	92
TiO_2/ $SrTiO_3$	HT	—	386.6#	Methanol	93
Rh doped $BaTiO_3$	SG	—	308	10% Methanol	94
$CaTiO_3$	HT	20	52	0.2 M NaOH	95
AgCl/Ag/ $CaTiO_3$	HT, chemical deposition	—	226.5	Methanol	96

$BiFeO_3$	HT	400		4 mM $Fecl_3$	97
$LaFeO_3$	SG	—	3315	Ethanol	98
$GaFeO_3$	SG	5	10	—	99
$BaZrO_3$	SS	—	500	—	100
Ta doped $BaZrO_3$	Precipitation	450	900	—	101
Sn doped $BaZrO_3$	SG	185	690	—	102
$SrSnO_3$	SS	113.5	227.2	—	103
$CaSnO_3$	SS	47	92	—	104
$CdS/LaMnO_3$	Reverse micelle	—	595	0.1 M Na_2S + 0.5 M Na_2SO_3	105

*HT- Hydrothermal route; ST- Solvothermal route; SG – Sol-gel route; SS – Solid-state route;

µmol/h

1.5 PHOTOCATALYTIC DYE DEGRADATION

Without clean and potable water, one cannot imagine a life in this world. The quality of water, therefore, one of the most important factors which directly controls the quality of life of human being as well as all living creatures on this planet. Owing to the growth of human population and modern industries, the quality of the surface and groundwater degraded day by day. Apart from the wastewater produced by the domestic use, industrial activity remains the main curse behind the water contamination. One of the main cause of water contamination by industries is the use of excessive dyes. Around 7×10^5 tons of dyes are annually used by industries globally every year and among that almost 15% of dyes directly discharged as industrial effluents. [106] Hence, removal of these harmful and carcinogenic materials from water is a challenging environmental problem.[107] Till date, numerous methods have been tested for dye removal from water stream like adsorption, precipitation, filtration, chlorination, ozonation, biodegradation, advanced oxidation processes etc.[108 – 113] Although each of these processes have their own merits and demerits, advanced oxidation process (AOP) is considered to most efficient among all other methods for water remediation from organic dyes.[114] AOPs can be classified into two categories – (a) non-photochemical AOPs and (b) photochemical AOPs. In AOP, water-soluble compounds are readily oxidized by the in-situ formed hydroxyl radicals by the help of some oxidants (such as oxygen, hydrogen peroxide) or suitable light source with some oxidants or suitable photocatalysts.[115, 116] Among AOP methods, photocatalytic dye degradation is fascinating to explore because of its simplicity in design, low-cost and effectiveness. In general, the organic dyes are degraded by the photocatalysts in photocatalysis process via the following mechanism-

1. On irradiation by light of suitable energy, electron-hole pairs are photogenerated in a semiconductor and negatively charged electrons move to the conduction band while positively charged holes reside in the valence band

2. These electrons from the conduction band and holes from the valence band drifts to the surface of the semiconductor and take part in several redox reactions with the dyes adsorbed onto the semiconductor surface
3. The photogenerated holes (h^+_{VB}) react with H_2O near the catalyst surface to produce hydroxyl ($OH^\bullet$) radicals, while, photogenerated electrons (e^-_{CB}) produce superoxide radical anion ($O_2^{\bullet-}$)
4. These formed hydroxyl radicals combine together to generate hydrogen peroxide
5. H_2O_2 reacts with superoxide radical anion to regenerate hydroxyl ions back
6. Finally, these hydroxyl radicals, which are very strong non-selective oxidants, discolor the adsorbed organic dyes onto the semiconductor surface by breaking them into CO_2 and water

$$\text{Photocatalyst} + h\nu \longrightarrow h^+_{VB} + e^-_{CB}$$

$$h^+_{VB} + H_2O \longrightarrow OH^\bullet + H^+$$

$$e^-_{CB} + O_2 \longrightarrow O_2^{\bullet-}$$

$$OH^\bullet + OH^\bullet \longrightarrow H_2O_2$$

$$H_2O_2 + O_2^{\bullet-} \longrightarrow OH^\bullet + OH^- + O_2$$

$$\text{Dye} + OH^\bullet \longrightarrow CO_2 + H_2O$$

A schematic of photocatalytic dye degradation process is presented in Figure **1.11**.

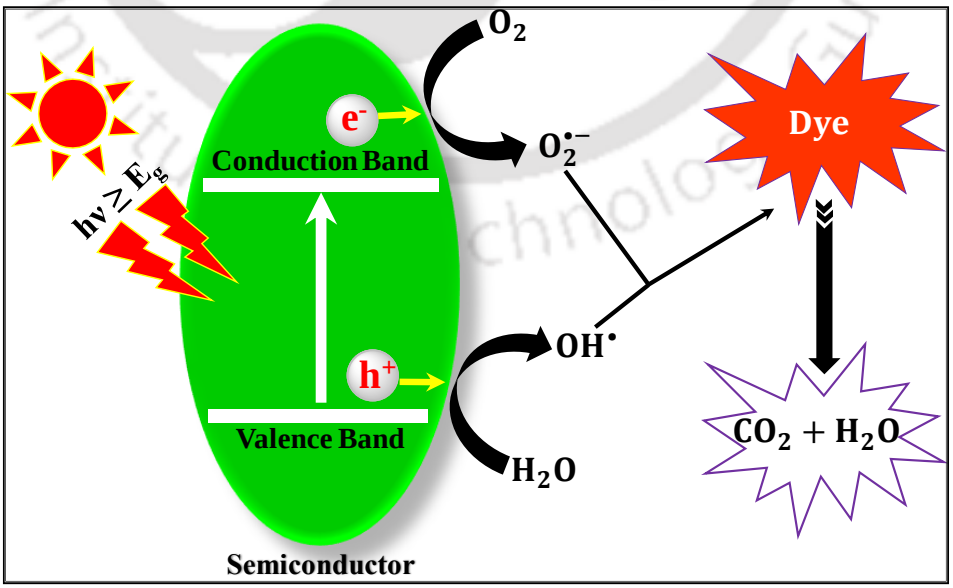

Figure 1.11 Schematic representation of photocatalytic dye degradation.

1.6 MOTIVATION AND OBJECTIVE OF THE PRESENT WORK

Perovskite oxide materials are the promising candidate for photocatalytic water oxidation and reduction owing to their appropriate electronic structure, structural flexibility towards numerous dopants, excellent thermal and chemical stability. Nevertheless, most of the pristine perovskite oxides suffer from either their wide band gap, which limits their light absorption only in the ultraviolet region of the solar spectrum or poor charge carrier drift toward the catalyst surface due to the high charge carrier recombination rate, which limits their photocatalytic effectiveness. Hence, further improvement in the electronic structure of the perovskite oxides is highly sought after. In this regard, the focus of present work is increasing the efficiency of the perovskite oxides in photocatalytic water oxidation and reduction that can be achieved by doping suitable metal ions in their crystal lattice or by coupling them with superior charge carrier transporting materials. The main objectives of the present work are –

- Design and synthesis of several metal ions doped perovskite oxides for effective water oxidation and reduction process
- Understanding the effect of metal ions in perovskite oxide lattice by means of the crystal phase, electronic structure and catalytic activity
- Investigation of the effect of oxygen stoichiometry in phase formation and overall catalytic activities in perovskite oxides
- Coupling wide band gap perovskite oxide material with quantum dots to make them visible light active
- Making composite of perovskite oxide materials with good charge carrier transporting materials to enhance the photogenerated charge carrier separation and overall catalytic activity
- To evaluate the photocatalytic water oxidation and reduction as well as organic dye degradation of synthesized doped and hybrid perovskite oxides

1.7 REFERENCES

1. http://www.eia.gov/forecasts/ieo/
2. http://www.iea.org/statistics/
3. Sathish, M.; Viswanathan, B; Viswanath, R.P. *Appl. Catal., B* **2007**, *74*, 307.
4. Nikolaidis, P.; Poullikkas, A. *Renewable Sustainable Energy Rev.* **2017**, *67*, 597.
5. Hosseini, S. E.; Wahid, M. A. *Renewable Sustainable Energy Rev.* **2016**, *57*,850.

6. Sinigaglia, T.; Lewiski, F.; Martins, M. E. S.; Siluk, J. C. M. *Int. J. Hydrogen Energy* **2017**, *42*, 24597.
7. Yerga, R. M. N.; Galvan, M. C. Á.; del Valle, F.; Mano, J. A. V.; Fierro, J. L. G. *ChemSusChem* **2009**, *2*, 471.
8. Seger, B. *Global Energy Consumption: The Numbers for Now and in the Future.***2016** (https://www.linkedin.com/pulse/global-energy-consumption-numbers-now-future-brian-segar)
9. Fujishima, A.; Honda, K. *Nature* **1972**, *238*, 37.
10. Lehn, J. M.; Sauvage, J. P.; Ziessel, R.; *Nouv. J. Chim.* **1980**, *4*, 623.
11. Domen, K.; Naito, S.; Suma, M.; Onishi, T.; Tamaura, K. *J. Chem. Soc., Chem. Commun.* **1980**, 543.
12. Sato, S.; White, J. M. *Ind. Eng. Chem. Prod. Res. Dev.* **1980**, *19*, 542.
13. Chen, X.; Shen, S.; Guo, L.; Mao, S. S. *Chem. Rev.* **2010**, *110*, 6503.
14. Jhang, J.; Zhou, P.; Liu, J.; Yu, J. *Phys. Chem. Chem. Phys.* **2014**, *16*, 20382.
15. Kubacka, A.; Fernandez-García, M.; Colon, G. *Chem. Rev.* **2012**, *112*, 1555.
16. Ashokkumar, M. *Int. J. Hydrogen Energy* **1998**, *23*, 427.
17. Yoshimura, J.; Ebina, Y.; Kondo, J.; Domen, K.; Tanaka, A. *J. Phys. Chem.* **1993**, *97*, 1970.
18. Kudo, A.; Omori, K.; Kato, H. *J. Am. Chem. Soc.* **1999**, *121*, 11459.
19. Kato, H.; Asakura, K.; Kudo, A. *J. Am. Chem. Soc.* **2003**, *125*, 3082.
20. Kim, H. G.; Hwang, D. W.; Lee, J. S. *J. Am. Chem. Soc.* **2004**, *126*, 8912.
21. Lee, Y.; Suntivich, J.; May, K. J.; Perry, E. E.; Shao-Horn, Y. *J. Phys. Chem. Lett.* **2012**, *3*, 399.
22. Borgarello, E.; Kiwi, J.; Grätzel, M.; Pelizzetti, E.; Visca, M. *J. Am. Chem. Soc.* **1982**, *104*, 2996.
23. Sasikala, R.; Sudarsan, V.; Sudakar, C.; Naik, R.; Panicker, L.; Bharadwaj, S. R. *Int. J. Hydrogen Energy* **2009**, *34*, 6105.
24. Kitano, M.; Takeuchi, M.; Matsuoka, M.; Thomas, J. M.; Anpo, M. *Catal. Today* **2007**, *120*, 133.
25. Dholam, R.; Patel, N.; Adami, M.; Miotello, A. *Int. J. Hydrogen Energy* **2008**, *33*, 6896.
26. Zuo, F.; Wang, L.; Wu, T.; Zhang, Z.; Borchardt, D.;Feng, P. *J. Am. Chem. Soc*. **2010**, *132*, 11856.
27. Kanade, K. G.; Kale, B. B.; Baeg, J.-O.; Lee, S. M.; Lee, C. W.; Moon, S.-J.; Chang, H. *Mater. Chem. Phys*. **2007**, *102*, 98.
28. Zhang, H.; Chen, G.; Li, Y.; Teng, Y. *Int. J. Hydrogen Energy* **2010**, *35*, 2713.
29. Kato, H.; Kudo, A. *J. Phys. Chem. B* **2002**, *106*, 5029.
30. Shen, P.; Lofaro Jr, J. C.; Woerner, W. R.; White, M. G.; Su, D.; Orlov, A. *Chem. Eng. J.* **2013**, *223*, 200.

31. Nishijima, K.; Kamai, T.; Murakami, N.; Tsubota, T.; Ohno, T. *Int. J. Photoenergy* **2008**, 173943.
32. Pany, S.; Parida, K. M. *ACS Sustainable Chem. Eng*. **2014**, *2*, 1429.
33. Kuang, L.; Zhang, W. *RSC Adv.* **2016**, *6*, 2479.
34. Nukumizu, K.; Nunoshige, J.; Takata, T.; Kondo, J. N.; Hara, M.; Kobayashi, H.; Domen, K. *J. Phys. Chem. B* **2003**, *107*, 791.
35. O'Regan, B.; Grätzel, M. *Nature* **1991**, *353*, 737.
36. Abe, R.; Sayama, K.; Sugihara, H. *J. Sol. Energy Eng.* **2005**, *127*, 413.
37. Dhanalakshmi, K.; Latha, S.; Anandan, S.; Maruthamuthu, P. *Int. J. Hydrogen Energy* **2001**, *26*, 669.
38. Youngblood, W. J.; Lee, S. H. A.; Maeda, K.; Mallouk, T. E. *Acc. Chem. Res.* **2009**, *42*, 1966.
39. Maeda, K.; Eguchi, M.; Lee, S. H. A.; Youngblood, W. J.; Hata, H.; Mallouk, T. E. *J. Phys. Chem. C* **2009**, *113*, 7962.
40. Moser, J.; Grätzel, M. *J. Am. Chem. Soc.* **1984**, *106*, 6557.
41. Maeda, K.; Eguchi, M.; Youngblood, W. J.; Mallouk, T. E. *Chem. Mater.* **2008**, *20*, 6770.
42. Maeda, K.; Lu, D.; Domen, K. *ACS Catal.* **2013**, *3*, 1026.
43. Wang, D.; Kako, T.; Ye, J. *J. Phys. Chem. C* **2009**, *113*, 3785.
44. Reddy, K. H.; Martha, S.; Parida, K. M. *RSC Adv.* **2012**, *2*, 9423.
45. Parida, K. M.; Nashim, A.; Mahanta, S. K. *Dalton Trans.* **2011**, 12839.
46. Li, Q.; Meng, H.; Zhou, P.; Zheng, Y.; Wang, J.; Yu, J.; Gong, J. *ACS Catal*. **2013**, *3*, 882.
47. Zhang, X.; Du, Y.; Zhou, Z.; Guo, L. *Int. J. Hydrogen Energy* **2010**, *35*, 3313.
48. Tsuji, I.; Kato, H.; Kudo, A. *Angew. Chem.* **2005**, *117*, 3631.
49. Zhang, K.; Jing, D.; Xing, C.; Guo, L. *Int. J. Hydrogen Energy* **2007**, *32*, 4685.
50. Xing, C.; Zhang, Y.; Yan, W.; Guo, L. *Int. J. Hydrogen Energy* **2006**, *31*, 2018.
51. Yuan, L.; Han, C.; Yang, M. Q.; Xu, Y. *J. Int. Rev. Phys. Chem.* **2016**, *35*, 1.
52. Maeda, K.; Takata, T.; Hara, M.; Saito, N.; Inoue,Y.; Kobayashi, H .; Domen, K. *J. Am. Chem. Soc*. **2005**, *127*, 8286.
53. Zhang, K.; Jing, D.; Xing, C.; Guo, L. J. *Int. J. Hydrogen Energy* **2007**, *32*, 4685.
54. Inoue, Y.; Asai, Y.; Sato, K. *J. Chem. Soc. Faraday Trans.* **1994**, *90*, 797.
55. Chen, X.; Shen, S.; Guo, L.; Mao, S. S. *Chem. Rev*. **2010**, *110*, 6503.
56. Seger, B.; Laursen, A. B.; Vesborg, P. C. K.; Pedersen, T.; Hansen, O.; Dahl, S.; Chorkendorff, I. *Angew. Chem., Int. Ed.* **2012**, *51*, 9128.
57. Zong, X.; Wu, G.; Yan, H.; Ma, G.; Shi, J.; Wen, F.; Wang, L.; Li, C. *J. Phys. Chem. C* **2010**, *114*, 1963.
58. Esswein, A. J.; Surendranath, Y.; Reece, S. Y.; Nocera, D. G. *Energy Environ. Sci.* **2011**, *4*, 499.

59. Chemelewski, W. D.; Lee, H. C.; Lin, J. F.; Bard, A. J.; Mullins, C. B. *J. Am. Chem. Soc.* **2014**, *136*, 2843.
60. Zhu, J.; Li, H.; Zhong, L.; Xiao, P.; Xu, X.; Yang, X.; Zhao, Z.; Li, J. *ACS Catal*. **2014**, *4*, 2917.
61. Peña, M. A.; Fierro, J. L. G. *Chem. Rev.* **2001**, *101*, 1981.
62. Lin, W. H.; Cheng, C.; Hu, C. C.; Teng, H. S. *Appl. Phys. Lett.* **2006**, *89*, 211904.
63. Hu, C. C.; Lee, Y. L.; Teng, H. S. *J. Mater. Chem.* **2011**, *21*, 3824.
64. Li, P.; Ouyang, S. X.; Xi, G. C.; Kako, T.; Ye, J. H. *J. Phys. Chem. C* **2012**, *116*, 7621.
65. Shi, J.; Guo, L. *Prog. Nat. Sci.* **2012**, *22*, 592.
66. Mueller, D. N.; Machala, M. L.; Bluhm, H.; Chueh, W. C. *Nat.Commun.* **2015**, *6*, 6097.
67. Bockris, J. O. 'M.; Otagawa, T.; Young, V. *J. Electroanal. Chem.* **1983**, *150*, 633.
68. Vojvodic, A.; Nørskov, J. K. *Science* **2011**, *334*, 1355.
69. Parravano, G. *J. Chem. Phys.* **1952**, *20*, 342.
70. Parravano, G. *J. Am. Chem. Soc.* **1953**, *75*, 1497.
71. Liu, J. W.; Chen, G.; Li, Z. H.; Zhang, Z. G. *Int. J. Hydrogen Energy* **2007**, *32*, 2269.
72. Hu, C.-C.; Teng, H. *Appl. Catal., A* **2007**, *331*, 44.
73. Meyer, T.; Priebe, J. B.; Silva, R. O.; Junge, T. H.; Bruckner, M. A.; Wohlrab, S. *Chem. Mater.* **2014**, *26*, 4705.
74. Kato, H.; Asakura, K.; Kudo, A. *J. Am. Chem. Soc.* **2003**, *125*, 3082.
75. Iwase, A.; Kato, H.; Kudo, A. *Appl. Catal., B* **2013**, *136*, 89.
76. Husin, H.; Su, W.-N.; Chen, H.-M.; Pan, C.-J.; Chang, S.-H.; Rick, J.; Chuang, W.-T.; Sheu, H.-S.; Hwang, B.-J. *Green Chem.* **2011**, *13*, 1745.
77. Xu, L.; Sun, X.; Tu, H.; Jia, Q.; Gong, H.; Guan, J. *Appl. Catal., B* **2016**, *184*, 309.
78. Iwase, A.; Kato, H.; Kudo, A. *ChemSusChem* **2009**, *2*, 873.
79. Kato, H.; Kudo, A. *J. Phys. Chem. B* **2001**, *105*, 4285.
80. Ishihara, T.; Nishiguchi, H.; Fukamachi, K.; Takita, Y. *J. Phys. Chem. B* **1999**, *103*, 1.
81. Kato, H.; Kobayashi, H.; Kudo, A. *J. Phys. Chem. B* **2002**, *106*, 12441.
82. Kuang, Q.; Yang, S. *ACS Appl. Mater. Interfaces* **2013**, *5*, 3683.
83. Townsend, T. K.; Browning, N. D.; Osterloh, F. E. *ACS Nano* **2012**, *6*, 7420.
84. Yu, H.; Ouyang, S.; Yan, S.; Li, Z.; Yu, T.; Zou, Z. *J. Mater. Chem.* **2011**, *21*, 11347.
85. Tan, H.; Zhao, Z.; Zhu, W.B.; Coker, E. N.; Li, B.; Zheng, M.; Yu, W.; Fan, H.; Sun, Z. *ACS Appl. Mater. Interfaces* **2014**, *6*, 19184.
86. Zou, J. P.; Zhang, L. Z.; Luo, S. L.; Leng, L. H.; Luo, X. B.; Zhang, M. J.; Luo, Y.; Guo, G. C. *Int. J. Hydrogen Energy* **2012**, *37*, 17068.
87. Ouyang, S.; Tong, H.; Umezawa, N.; Cao, J.; Li, P.; Bi, Y.; Zhang, Y.; Ye, J. *J. Am. Chem. Soc.* **2012**, *134*, 1974.

88. Yu, H.; Yan, S.; Li, Z.; Yu, T.; Zou, Z. *Int. J. Hydrogen Energy* **2012**, *37*, 12120.
89. Lei, S. L.; Yu, J.; Bao, S. K.; Zeng, G. S.; Liu, H. L.; Wu, D. D.; Tang, X. H.; Zou, J. P.; Au, C. T. *Appl. Catal., A* **2015**, *493*, 58.
90. Su, E. C.; Yeh, J. M.; Huang, B. S.; Lee, J. T.; Wey, M. Y. *Sol. Energy* **2017**, *147*, 240.
91. Guan, X.; Guo, L. *ACS Catal.* **2014**, *4*, 3020.
92. Huang, B. S.; Su, E. C.; Wey, M. Y. *Chem. Eng. J.* **2013**, *223*, 854.
93. Ng, J.; Xu, S.; Zhang, X.; Yang, H. Y.; Sun, D. D. *Adv. Funct. Mater.* **2010**, *20*, 4287.
94. Maeda, K. *ACS Appl. Mater. Interfaces* **2014**, *6*, 2167.
95. Mizoguchi, H.; Ueda, K.; Orita, M.; Moon, S.-C.; Kajihara, K.; Hirano, M.; Hosono, H. *Mater. Res. Bull.* **2002**, *37*, 2401.
96. Jiang, Z.; Pan, J.; Wang, B.; Li, C. *Appl. Surf. Sci.* **2018**, *436*, 519.
97. Li, S.; Zhang, J.; Kibria, M. G.; Mi, Z.; Chaker, M.; Ma, D.; Nechache, R.; Rosei, F. *Chem. Commun.* **2013**, *49*, 5856.
98. Tijare, S. N.; Joshi, M. V.; Padole, P. S.; Mangrulkar, P. A.; Rayalu, S. S.; Labhsetwar, N. K. *Int. J. Hydrogen Energy* **2012**, *37*, 10451.
99. Dhanasekaran, P.; Gupta, N. M. *Int. J. Hydrogen Energy* **2012**, *37*, 4897.
100. Yuan, Y.; Zhang, X.; Liu, L.; Jiang, X.; Lv, J.; Li, Z.; Zou, Z. *Int. J. Hydrogen Energy* **2008**, *33*, 5941.
101. Khan, Z.; Qureshi, M. *Catal. Commun*. **2012**, *28*, 82.
102. Yuan, Y.; Zhao, Z.; Zheng, J.; Yang, M.; Qiu, L.; Li, Z.; Zou, Z. *J. Mater. Chem.* **2010**, *20*, 6772.
103. Zhang, W. F.; Tang, J.; Ye, J. *Chem. Phys. Lett*. **2006**, *418*, 174.
104. Zhang, W.; Tang, J.; Ye, J. *J. Mater. Res*. **2007**, *22*, 1859.
105. Kida, T.; Guan, G.; Minami, Y.; Ma, T.; Yoshida, A. *J. Mater. Chem.* **2003**, *13*, 1186.
106. Zhao, J.; Wu, T.; Wu, K.; Oikawa, K.; Hidaka, H.; Serpone, N. *Environ. Sci. Technol.* **1998**, *32*, 2394.
107. Spadaro, J. T.; Isabelle, L.; Renganathan, V. *Environ. Sci. Technol.* **1994**, *28*, 1389.
108. Neppolian, B.; Choi, H. C.; Sakthivel, S.; Arabindoo, B.; Murugesan, V. *Chemosphere* **2002**, *46*, 1173.
109. Sakthivel, S.; Neppolian, B.; Shankar, M. V.; Arabindoo, B.; Palanichamy, M.; Murugesan, V. *Sol. Energy Mater. Sol. Cells* **2003**, *77*, 65.
110. So, C. M.; Cheng, M. Y.; Yu, J. C.; Wong, P. K. *Chemosphere* **2002**, *46*, 905.
111. Hu, C.; Yu, J. C.; Hao, Z.; Wong, P. K. *Appl. Catal., B* **2003**, *42*, 47.
112. Minero, C.; Maurino, V.; Pelizzetti, E. *Res. Chem. Intermed.* **1997**, *23*, 291.
113. Chun, H.; Yizhong, W. *Chemosphere* **1999**, *39*, 2107.
114. Augugliaro, V.; Baiocchi, C.; Bianco Prevot, A.; García- López, E.; Loddo, V.; Malato, S.; Marcí, G.; Palmisano, L.; Pazzi, M.; Pramauro, E. *Chemosphere* **2002**, *49*, 1223.

115. Madhavan, J.; Maruthamuthu, P.; Murugesan, S.; Anandan, S. *Appl. Catal.,B* **2008**, *83*, 8.
116. Qi, X. -H.; Zhuang, Y. -Y.; Yuan, Y. -C.; Gu, W. -X. *J. Hazard. Mater*. **2002**, *90*, 51.

Chapter 2

Experimental Section

This Chapter describes the detailed synthetic procedures and characterizations of perovskite oxide photocatalysts and its hybrid photocatalysts. This Chapter also demonstrates the detailed experimental procedure for photocatalytic water oxidation, water reduction and dye degradation. Descriptions of in-house build photocatalytic reactor set up and method for apparent quantum yield (AQY) included here.

2.1 INTRODUCTION

Synthesis of different perovskite oxides, metal ion doped perovskite oxides and their composite with superior electron transporting material like graphene oxide (GO) and carbon dots (CDs) are described in this chapter using conventional solid-state route, ultrasonic dispersion and hydrothermal route, which offers product with good yields and good crystallinity and descent photocatalytic activity.

2.2 CHEMICAL DETAILS

Lanthanum oxide (Sigma Aldrich), manganese acetate (Merck), strontium carbonate (Merck), ruthenium oxide (Alfa Aesar), barium chloride (Merck), zirconium oxychloride octahydrate (Sigma Aldrich), ceric ammonium nitrate (Merck), barium chloride dihydrate (Merck), potassium hydroxide pellets (Merck), sodium sulfide (Sigma Aldrich), sodium sulfite (Sigma Aldrich), glacial acetic acid (Merck), citric acid (Merck), ethylene diamine (Merck), graphite powder (Loba Chemie), sodium nitrate (Merck), hydrogen peroxide (Merck), hydrochloric acid (Merck), ammonium hydroxide (Merck), potassium permanganate (Merck), acetone (Merck), ethanol (TMEDA). All the chemicals were used as received without any purification.

2.3 SYNTHESIS DETAILS

2.3.1 Synthesis of $La_{1-x}Sr_xMnO_3$ (x = 0.0 – 0.5)

Strontium doped lanthanum manganites were prepared by the conventional solid-state route by using high-purity La_2O_3, $Mn(CH_3COO)_2$ and $SrCO_3$. A stoichiometric amount of the reagents were weighed accurately and ground well in an agate mortar and pestle for an hour with the help of acetone and subsequently these homogenously mixed powder of different compositions were kept in different alumina crucibles and kept inside a box furnace and calcined at 1050 °C for 12 h in air at a rate of 5 °C/min. Then the compounds were cooled down to room temperature naturally and ground again. After this process, the compounds were calcined again for 72 h at 1050 °C with several intermediate grinding.

2.3.2 Synthesis of Graphene Oxide (GO)

Graphene oxide was prepared by Hummers method through oxidation of graphite.[1] Initially, at 0 – 5 °C temperature graphite powder (0.5 g) and $NaNO_3$ (0.5g) were mixed in 30 mL of H_2SO_4 (95%). After 30 min of vigorous stirring, 1.5 g of $KMnO_4$ was added very slowly into this reaction mixture. During the addition of $KMnO_4$, the temperature of the reaction mixture

was kept lower than 15 °C. After that, the reaction mixture was vigorously stirred at 35 °C for 7 h and added 50 mL of water into the reaction mixture and the color of the mixture turned faded to brown. Then the temperature was raised to 98 °C and at this temperature, the reaction mixture was stirred for another 6 h. Hence, 50 mL of water was added to this solution and lastly to remove unreacted $KMnO_4$, if any, 1 ml of H_2O_2 (30 wt %) was added to the reaction solution. To purify the reaction mixture, it was washed by centrifuging, rinsing and sonicating with 10% HCl and deionized (DI) water for several times. After centrifugation, the product was dried under vacuum at room temperature. In this process, the as-synthesized GO powders form GO nano sheets upon ultrasonic treatment.

2.3.3 Synthesis of $LaMn_{1-x}Ru_xO_3$ (x = 0.0 – 0.4)

Ruthenium doped lanthanum manganite compounds were prepared by following the conventional solid-state route using high-purity La_2O_3, $Mn(CH_3COO)_2$ and RuO_2. A stoichiometric amount of the reagents were weighed accurately and ground well in an agate mortar and pestle for an hour with the help of acetone and subsequently these homogenously mixed powder of different compositions were kept in different alumina crucibles and kept inside a box furnace and calcined at 1050 °C for 12 h in air at a rate of 5 °C/min. Then the compounds were cooled down to room temperature naturally and ground again. Finally, the compounds were again calcined for 72 h at 1050 °C with several intermediate grinding.

2.3.4 Synthesis of $La_{1-x}Sr_xMnO_3$ (x = 0.0 – 0.5)/GO Composite

$La_{1-x}Sr_xMnO_3$ (x = 0.0 – 0.5)/GO was prepared by mechanical grinding. Briefly, 0.2 g of as prepared $La_{1-x}Sr_xMnO_3$ (x = 0.0 – 0.5) compound was carefully ground with 1 wt% of as-synthesized GO by using agate mortar pestle and the motivation behind the grinding of $La_{1-x}Sr_xMnO_3$ (x = 0.0 – 0.5) and GO is to make uniform contact between them. The obtained powder of $La_{1-x}Sr_xMnO_3$ (x = 0.0 – 0.5)/GO was used for to examine the effect of graphene oxide on photocatalytic water oxidation.

2.3.5 Synthesis of $BaZr_{1-x}Ce_xO_3$ (x = 0.00 – 0.04)

Cerium doped barium zirconate compounds were prepared following a modified hydrothermal method.[2] The reactions were carried out in a stainless-steel autoclave with Teflon liner at 200 °C and autogenous pressure. Briefly, a stoichiometric amount of $BaCl_2 \cdot 2H_2O$, $ZrOCl_2 \cdot 8H_2O$ and $(NH_4)_2Ce(NO_3)_6$ were weighed according to the stoichiometry of $BaZr_{1-x}Ce_xO_3$ (x = 0.00 – 0.04) and transferred to a Teflon made autoclave reactor. A 20 M aqueous KOH solution was prepared in a round-bottomed flask by dissolving

a calculated amount of KOH pellets into milli-Q water. To avoid any inhomogeneous mixing of the reagents, the as-prepared KOH solution was added to the previously taken metal salts and filled the reactor up to 70% of its volume and vigorously stirred for 1 h. Thereafter, these Teflon beakers were sealed inside a stainless steel jacket and kept in a pre-heated electric oven for 24 h at 200 °C. After completion of the reaction, autoclaves were allowed to cool to room temperature. The white precipitate was centrifuged and washed with water, dilute acetic acid and ethanol several times to remove the impurities. Finally, the obtained purified products were dried at 100 °C overnight.

2.3.6 Synthesis of Carbon Dots (CDs)

Water-soluble CDs were prepared by following a facile carbonation process via hydrothermal route. [3] 2.1g of citric acid was dissolved in 20 mL of water in a Teflon made reactor by continuous stirring. After complete dissolution of citric acid in water, 670 µL of ethylene diamine was added dropwise under vigorous stirring. This solution was then placed inside a stainless-steel jacket and kept inside a pre-heated electric oven at 200 °C for 5h. After cooling down to room temperature, the brownish red solution was filtered through a 0.4-micron syringe filter to separate larger particles. This filtrate was then dialyzed by using a dialysis bag (Da = 1000) and Milli-Q water for 1 day to remove unreacted reagents. The water was changed in every 4 h. As-synthesized CDs were collected by drying the dialyzed solution at 80 °C overnight.

2.3.7 Synthesis of Carbon Dots (CDs)_$BaZrO_3$ (BZO) Hybrid Nanomaterials

To prepare *x* wt% CDs_BZO (*x* = 0 – 4) (hereinafter referred to as "*x*C_BZO") hybrid nanomaterials with a different weight percentage of carbon dots, we have taken a certain amount of BZO in a round-bottomed flask and to it added the calculated amount of CDs. These compounds were then dispersed in ethanol at 45 °C for 2 h by sonication. Ethanol was removed in a rotary evaporator to collect the different hybrid compounds.

2.4 PHOTOCATALYTIC ACTIVITY EVALUATION

2.4.1 Photocatalytic Water Oxidation and Reduction

The photocatalytic oxygen evolution reaction from water was carried out in a 100 ml two neck double-walled quartz round-bottomed flask with a water circulation through the outer jacket to maintain the temperature within the reactor. The necks of the reactor were sealed with rubber septum to prevent leakage of the gas produced. The reaction conditions were

maintained at room temperature by continuous water circulation. A 500W tungsten halogen lamp was used as the light source to conduct the photocatalytic reaction. The emission profile of the lamp was confined in between the wavelength ranges 195 – 1100 nm. In a typical photocatalytic experiment, 25 mg of catalyst was dispersed in 50 mL of water (in case of $La_{1-x}Sr_xMnO_3$ (x = 0.0 – 0.5) photocatalysts, we have used 100 mg of catalyst in 25 mL of water).

A 100 mL two-neck double walled quartz round bottomed flask was used for all the photocatalytic H_2 evolution reactions. The reactor was sealed with rubber septum to prevent gas leakage. To conduct the photocatalytic reaction, a 300 W tungsten halogen lamp was used as the light source with emission profile in between the wavelength ranges 195 – 1100 nm. In every photocatalytic experiment, typically 25 mg of catalyst and 0.25 M Na_2SO_3/0.35 M Na_2S mixture as a sacrificial reagent for hole scavenging was dispersed in 50 mL of water using a magnetic stirrer.

The reactor was purged with nitrogen for 10 minutes at a flow rate of 200 mL per minute monitored by a rotameter and consequently, the system was evacuated by a vacuum pump in order to remove the dissolved oxygen and any other gases from inside the reactor. This process was repeated several times before irradiating the system by a tungsten halogen lamp placed 15 cm away from the reactor. During the irradiation, the water suspension was constantly stirred to confirm uniform exposure of the catalyst to the light source. The gas sample was collected every 15 minutes up to 1 hour by a 1mL gastight syringe and was analyzed by gas chromatography, using a thermal conductivity detector (TCD), Molesieve column with nitrogen as the carrier gas. In case of $La_{1-x}Sr_xMnO_3$ (x = 0.0 – 0.5) photocatalysts, we have purged N_2 gas for 30 minutes and collected the evolved gas by inverted burette method. No considerable amount of gas evolution from the photoreactor was observed in absence of either photocatalyst or light irradiation which confirms the role of the photocatalyst in water oxidation/reduction.

The apparent quantum yield (AQY) of the photocatalysts were measured under the same reaction condition and it was calculated using the following equation: [4]

$$\mathrm{AQY} = \frac{\text{Number of reacted electrons}}{\text{Number of incident photons}} \times 100\%$$

$$= \frac{\text{Number of moles of } O_2/2 \times \text{Number of moles of } H_2 \text{ produced in 1 hour}}{\text{Number of incident photons in 1 hour}} \times 100\%$$

2.4.2 Schematic Diagram of Used Photocatalytic Reactor Setup

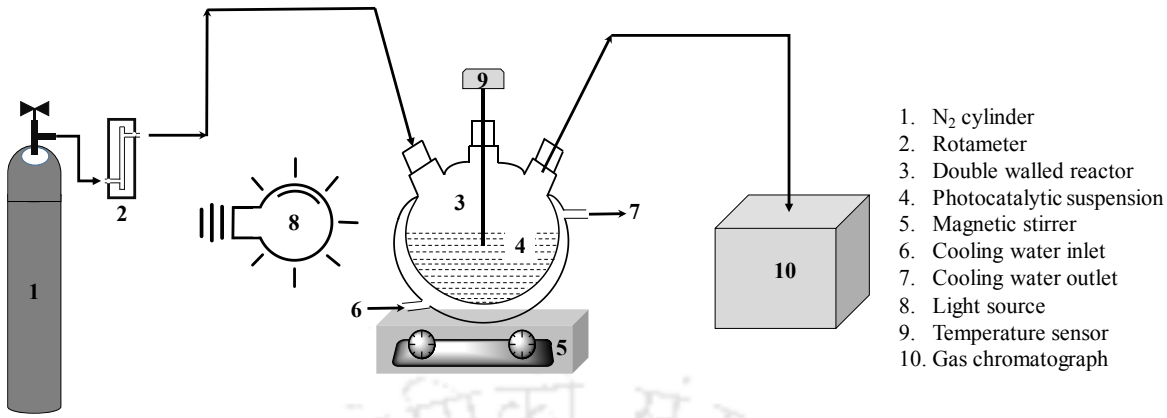

2.4.3 Photocatalytic Methyl Orange (MO) Dye Degradation

The dye degradation efficiency of the catalysts was analyzed by the monitoring the absorbance of MO dye solution. The experiments were carried out in the same reactor in which photocatalytic water oxidation was performed. MO solution at an acidic pH of 2.5 was made by adding the calculated amount of concentrated hydrochloric acid to it. A 50 mL of 10^{-5} M of prepared MO solution was taken inside the reactor and 50 mg of catalyst was added to it and stirred continuously for 15 minutes in dark to attain the adsorption-desorption equilibrium. Hence, the dye mixture was illuminated by the aforesaid 500W tungsten halogen lamp from a distance of 15 cm. Continuous water circulation through the outer jacket of the reactor was carried out to maintain the reaction temperature at room temperature. After illuminating the reactor, 1 ml of the dye solution was taken out from the reactor in every 5 minutes and centrifuged to settle down all the catalyst particles and the dye solution was further filtered through a 0.45µm syringe filter. The electronic absorption spectra of the supernatant dye solution were recorded in the range of 200 – 800 nm. The photocatalytic degradation efficiency was calculated as follows,

$$\text{Efficiency}(\%) = \frac{(C_0 - C)}{C_0} \times 100$$

Where, C_0 is the initial MB dye concentration and C is the MO dye concentration in the filtrates at certain time after light irradiation. [5]

2.4.4 Photocatalytic Methylene Blue (MB) Dye Degradation

Photocatalytic methylene blue (MB) dye degradation experiments were performed in a 100 mL round-bottom quartz flask by illuminating with a 300 W tungsten–halogen lamp kept 15 cm away from the reactor. 50 mg of the photocatalyst was dispersed in 50 mL of 10^{-5} M aqueous MB solution for the photocatalytic dye degradation analysis. The pH of the dye solution was adjusted to 13 by adding required amount of aqueous NH_3 solution. In order to achieve adsorption-desorption equilibrium among the dye, catalyst particles, dissolved oxygen, and atmospheric oxygen, the mixture was stirred for 30 minutes in the dark. During 1 h light irradiation, 2 mL of solution was collected from the photo-reactor in every 15 minutes. The collected dye solutions were centrifuged for 5 minutes to settle the suspended photocatalysts. The electronic absorption spectra of the supernatant dye solution were recorded in the range of 200 – 800 nm. By monitoring change in absorbance at 664 nm, the degradation of MB dye was determined. The photocatalytic degradation efficiency was calculated as follows,

$$\text{Efficiency}(\%) = \frac{(C_0 - C)}{C_0} \times 100$$

Where, C_0 is the initial MB dye concentration and C is the MB dye concentration in the filtrates at certain time after light irradiation. [5]

2.5 CHARACTERIZATION

The synthesized compounds were characterized by using various techniques. The instrumental techniques used in the present investigations comprise of:

1. Powder X-ray diffraction (PXRD) with Brucker D2 Phaser and Rigaku TTRAX III X- ray diffractometer with Cu Kα radiation (α = 1.540 Å) source
2. Fourier transformed infrared spectroscopic (FTIR) study was performed in a PerkinElmer instrument at room temperature with KBr pellet
3. Field emission scanning electron microscopy (FE-SEM), Zeiss Sigma
4. Energy-dispersive X-ray (EDX) spectroscopic analysis INCA, Oxford instruments
5. 200 kV Field emission transmission electron microscope (FE-TEM), JEOL JEM 2100
6. UV-visible diffuse reflectance spectroscopy (UV-Vis DRS) (JASCO V-650 spectrophotometer) with integrating sphere of 150 mm and $BaSO_4$ as an internal reflectance standard; and PerkinElmer Lambda 750 UV-visible spectrometer
7. Perkin Elmer Lambda 25 UV-visible spectrometer

8. Photoluminescence spectra (PL) were recorded in Horiba Scientific Fluoromax-4 spectrophotometer
9. Time-resolved photoluminescence measurements (TRPL) were performed on a LifeSpec II Edinburgh instrument
10. Electron spin resonance (ESR) spectra were measured on X-band Microwave Unit, JES-FA200 ESR spectrometer at room temperature at 100 G amplitude (χ), 9.444 GHz microwave frequency and 100 kHz modulation frequency
11. X-ray photoelectron spectroscopy (XPS) were carried out using a Kratos AXIS Supra photoelectron spectrometer (Used in Chapter **3&5**), a SPECS spectrometer, GmbH, Berlin, Germany (used in Chapter **4**), a PHI 5000 Versa Prob II, FEI Inc. (used in Chapter **6**) with a monochromatized X-ray source of Al-K_α ($h\nu$ = 1486.6 eV)
12. Gas Chromatography (Varian CP 3800 GC (used in Chapter **3**)/ Agilent 7890A GC (used in Chapter **4 – 6**))
13. Laser micro Raman analysis was carried out in a Horiba LabRAM HR spectrometer with a 633 nm laser

2.6 APPARENT QUANTUM YIELD (AQY) CALCULATION

We have calculated the AQY of the photocatalysts by following a method reported by Sasikala *et al*. [4] Total incident light intensity on the reactor was measured using an HTC LX101A lux meter; the lux meter is placed at the center where the reactor is placed for irradiation. Considering the uniform intensity distribution of lamp, a correction for the difference in the area of the sensor of lux meter and the reactor surface area is evaluated. We have evaluated the absorbance onset of all the studied photocatalysts and all these photocatalysts show their absorbance onset within the wavelength range of 200 – (200 + n) nm. Therefore, the fraction of light intensity only in this wavelength region (vary with different samples) is considered for quantum efficiency calculation. The emission profile of the lamp gives the incident light intensity in the range of 200 – 1100 nm. The energy of a single photon of the polychromatic light source is considered as the weighted average energy (E_a) of all the photons in 200 – (200 + n) nm wavelength range. Now, the contribution of the photon of each wavelength λ_i towards the total energy can be calculated as

$$E_i = \frac{I_{\lambda_i}}{I_{total}} \times \frac{hc}{\lambda_i}$$

where $I_{\lambda i}$ is the intensity at wavelength λ_i and I_{total} is obtained from the lamp emission profile by adding the intensities of all photons in the wavelength range of 200 – (200 + n) nm. The weighted average energy of single photon (E_a) is calculated as

$$E_a = \sum_{\lambda=200}^{(200+n)} E_i(\lambda_i)$$

Again, total incident light in 1 h in the wavelength range of 200 – (200 + n) nm (E_m) is given by

$$E_m = \frac{\text{(Total incident light energy in 1h} \times \text{Area under the curve for the wavelength in the wavelength rangeof } 200-(200+n)\text{ nm)}}{\text{Area under the curve for the entire emission profile}}$$

Total number of incident photons (N) in the wavelength range of 200 – (200 + n) nm is given by

$$N = \frac{E_m}{E_a}$$

$$\text{AQY (\%)} = \frac{\text{(No. of moles of } O_2\text{) or (2} \times \text{No. of moles of } H_2\text{) produced in 1 h} \times (6.023 \times 10^{23})}{\text{Total number of incident photons in 1 h}} \times 100$$

2.7 REFERENCES

1. Hummers, W. S.; Offeman, R. E. *J. Am. Chem. Soc.* **1958**, *80*, 1339.
2. Dong, Z.; Ye, T.; Zhao, Y.; Yu, J.; Wang, F.; Zhang, L.; Wang, X.; Guo, S. *J. Mater. Chem.* **2011**, *21*, 5978.
3. Zhu, S.; Meng, Q.; Wang, L.; Zhang, J.; Song, Y.; Jin, H.; Zhang, K.; Sun, H.; Wang, H.; Yang, B. *Angew. Chem. Int. Ed.* **2013**, *52*, 3953.
4. Sasikala, R.; Sudarsan. V.; Sudakar, C.; Naik, R.; Sakuntala, T.; Bharadwaj, S. R. *Int. J. Hydrogen Energy* **2008,** *33*, 4966.
5. Liu, J.; Zhang, L.; Li, N.; Tian, Q.; Zhou, J.; Sun, Y. *J. Mater. Chem. A* **2015**, *3*, 706.

Chapter 3

Modulating the Electronic Structure of Lanthanum Manganite by Ruthenium Doping for Enhanced Photocatalytic Water Oxidation

This chapter presents the synthesis of a new B site doped lanthanum manganite, $LaMn_{1-x}Ru_xO_3$ (x = 0.0-0.4) and its photocatalytic activity for water oxidation as well as dye degradation. The doped compounds are composed of both rhombohedral and cubic phase and in biphasic systems which facilitates the photo generated carrier transfer while reduce electron hole recombination by inhibiting the back electron transfer through the interfacial region. Rietveld refinement studies of the PXRD of the compounds confirms the reduction of lattice distortion as well increase in Mn-O-Mn bond angle to 180° with progressive increase in Ruthenium doping, which facilitates the charge carrier movement of the catalysts. Variations in band gap as well as different redox reactions taking place due to doping are studied.

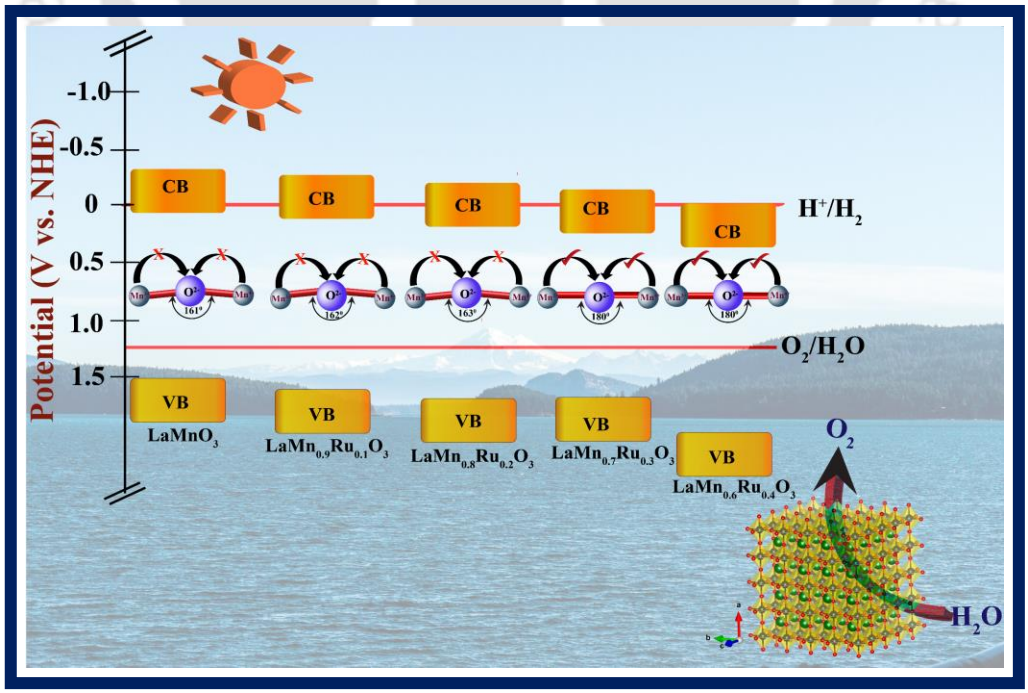

Patra *et al.* *Phys. Chem. Phys. Chem.* **2017**, *19*, 12167.

3.1 INTRODUCTION

To deal with the rising global energy demand, depletion of fossil fuels and rising environment pollution due to excessive use of fossil fuels, alternate environmentally benign and renewable energy resources are highly deemed. Energy harvesting through photocatalytic water splitting to produce H_2 and O_2 gases is a promising option. In this process, the oxygen evolution reaction is one of the main bottlenecks that limits the overall catalytic efficiency of a catalyst.[1, 2] To mitigate this problem, in recent past notable progress has been reported in the quest for efficient photochemical oxygen generating catalysts.[3 – 7] Among all, perovskite oxides have gained lots of interest in the field of oxygen evolution reaction and oxygen reduction reaction since the report of Meadowcroft, in 1970.[8] Perovskite oxides have been extensively used as effective catalysts for hydrogen production, organic pollutant removal, automotive emission control, hydrocarbon oxidation, removal of CO, NO_x, volatile organic compounds etc.[9 – 15] Among perovskite oxides, $LaMnO_3$ (LMO) is one of the extensively explored material in the field of catalysis.[16 – 21] The catalytic activity of $LaMnO_3$ is ascribed to the lattice vacancies or presence of Mn (III)/Mn (IV) average valence of Mn in it.[22, 23] Oxygen stoichiometry also plays an important role in maintaining the occurrence of mixed valence states of Mn (Mn (III)/Mn (IV)) in LMO.[24]

As revealed by many studies, the nature and valence of the B site cation actually control the catalytic properties of the doped perovskite materials as the nature of the B site species actually changes the bond strength between oxygenated species and the B site species.[25 – 27] In photocatalysis processes, Ru is often used as a dopant to modify the crystal structure and electronic structure of a photocatalyst and also increase the photocatalytic activity of the material by reducing the charge carrier recombination.[28, 29] From preceding reports it is known that ruthenium doping at the manganese site influences the crystal structure, electronic transport properties as well as magnetic characteristics of the perovskite manganates.[30] In this chapter, to explore the role of B-site doping in LMO by Ru(IV) in structure, phase formation, and its consequences in photocatalytic properties, we have synthesized $LaMn_{1-x}Ru_xO_3$ (x = 0.0 – 0.4) [where, x is the partial substitution degree of ruthenium] by conventional solid-state synthesis in air.

3.2 EXPERIMENTAL SECTION

3.2.1 Preparation of $LaMn_{1-x}Ru_xO_3$ (x = 0.0 – 0.4)

Ruthenium doped lanthanum manganite compounds were prepared by following previously reported solid-state route using high-purity La_2O_3, $Mn(CH_3COO)_2$ and RuO_2.[31] A stoichiometric amount of the reagents were weighed accurately and ground well in an agate mortar and pestle for an hour with the help of little acetone and subsequently these homogenously mixed powder of the different compositions were kept in different alumina crucibles and kept inside a box furnace and calcined at 1050 °C for 12 h. in air at a rate of 5 °C/min. Then the compounds were cooled down to room temperature naturally and ground again. After this process, the compounds were calcined again for 72 h. at 1050 °C.

3.3 RESULTS AND DISCUSSION

3.3.1 Powder X-ray Diffraction (PXRD) Patterns and Rietveld Refinement

The crystal structure and phase purity of the materials were determined by powder X-ray diffraction (PXRD) patterns. The diffractogram patterns of all the compositions are free from any impurity peaks and are indexed. PXRD patterns for $LaMn_{1-x}Ru_xO_3$ photocatalysts (x = 0.0 – 0.4) have been shown in Figure **3.1**. From the diffractogram, it is verified that the parent compound LMO belongs to the rhombohedral phase with $R\bar{3}c$ space group (no. 167) [JCPDS file: 36–1092]. LMO can attain different crystal phases such as cubic, orthorhombic, rhombohedral, monoclinic or triclinic. The formation of LMO crystal phase is essentially dependent on the synthesis protocol and calcination temperature, which alters the oxygen stoichiometry, thereby influencing the crystal structure parameters.[32] In $LaMn_{1-x}Ru_xO_3$, Ru should exist as Ru (IV) to fulfil the charge neutrality, however, in rhombohedral LMO, Mn exists as a mixture of two oxidation states, Mn (III) ($t_{2g}^3e_g^1$) and Mn (IV) ($t_{2g}^3e_g^0$) as it is known that even without any doping in LMO, it shows wide range of oxygen over stoichiometry leading to the formation of Mn (IV) by oxidation of some of its Mn (III).[33] Substitution of Ru in Mn sites by virtue of its availability of vacant ‘d’ orbital, has the possibility of exhibiting two oxidation states, Ru (IV) ($t_{2g}^4e_g^0$) and Ru (V) ($t_{2g}^3e_g^0$).[34] The redox potentials of Mn (III) ↔ Mn (IV) (1.02 eV) is comparable to that of Ru (IV) ↔ Ru (V) (1.07 eV) which facilitates the mixed valence states in doped LMO viz., Ru (IV) + Mn (IV) → Ru (V) + Mn (III).[35] The ionic radii of six coordinated Mn (III) and Mn (IV) are 65 pm and 52 pm, respectively, whereas the ionic radii of six coordinated Ru (IV) and Ru (V) are 62 pm and 56

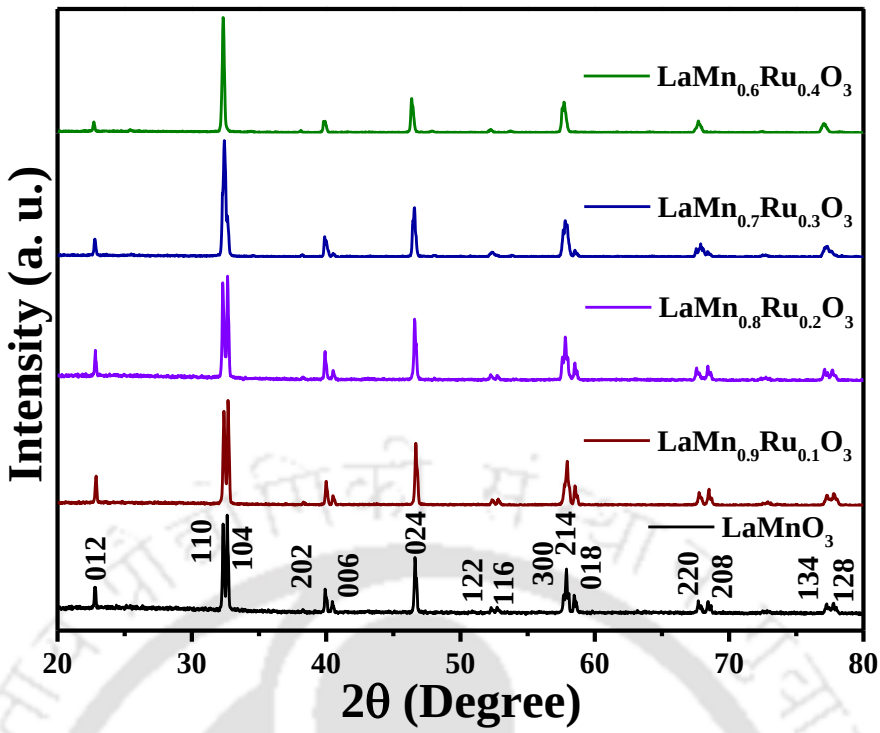

Figure 3.1 Powder X-ray diffraction pattern of all the synthesized $LaMn_{1-x}Ru_xO_3$ (x = 0.0 – 0.4) catalysts.

pm, respectively. Hence, steric effect inside the crystal lattice is induced as well as lattice constants of the crystal increases because of the large ionic size of Ru (IV) /Ru (V) compared to that of the Mn (III) /Mn (IV).[36] Hence, it is clear that because of these aforementioned conversions of charge pairs, the peaks get shifted towards lower 2θ value as well as the volume of the doped materials increases progressively with higher ruthenium doping. Owing to progressive Ru doping, LMO gains weight linearly, hence, crystal structure shifts towards cubic phase to release the induced chemical stress inside the crystal lattice by lowering the distortion of the octahedron.[37] This is being confirmed by the obtained data from the Rietveld refinements of the PXRD patterns of the LMO and Ru doped LMOs (Figure **3.2**). Doublet of the highest intensity peak at around 32.5° corresponding to (hkl) values (110) and (104) gradually merged to one peak with progressive Ru doping in LMO. This phenomenon clearly indicates the presence of a modified crystallographic symmetry in Ru doped LMO leading to the formation of cubic phase, space group $Pm\bar{3}m$ (no. 221) as revealed by Rietveld refinement of the PXRD patterns (Figure **3.2**).

LMO crystallizes in rhombohedral structure with La, Mn and O atoms in the Wyckoff position 6a (0, 0, 0.25), 6b (0, 0, 0) and 18e (0.44110, 0, 0.25) respectively. In the cubic Ru

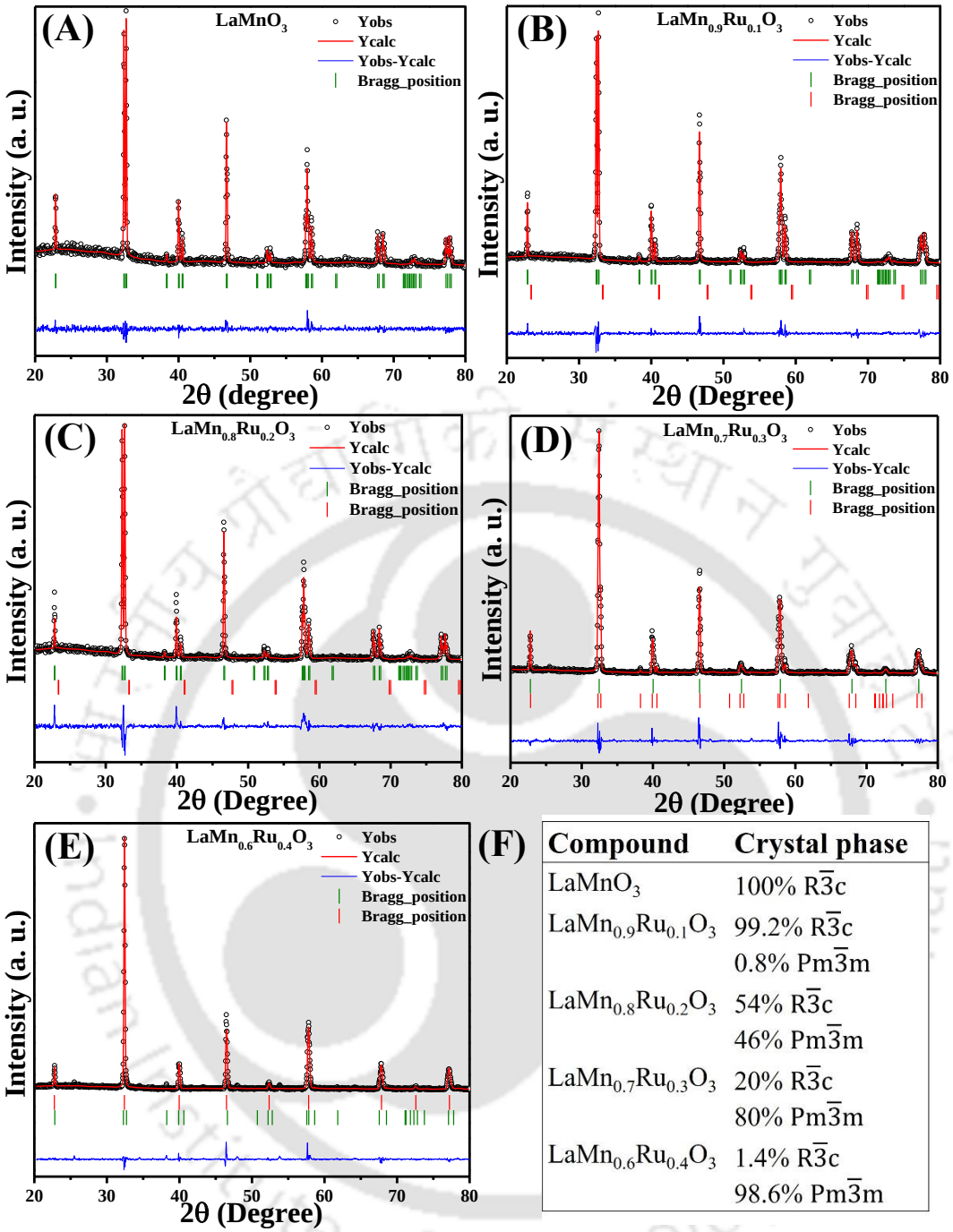

(F)

Compound	Crystal phase
$LaMnO_3$	100% $R\bar{3}c$
$LaMn_{0.9}Ru_{0.1}O_3$	99.2% $R\bar{3}c$
	0.8% $Pm\bar{3}m$
$LaMn_{0.8}Ru_{0.2}O_3$	54% $R\bar{3}c$
	46% $Pm\bar{3}m$
$LaMn_{0.7}Ru_{0.3}O_3$	20% $R\bar{3}c$
	80% $Pm\bar{3}m$
$LaMn_{0.6}Ru_{0.4}O_3$	1.4% $R\bar{3}c$
	98.6% $Pm\bar{3}m$

Figure 3.2 Rietveld refined PXRD profiles of the synthesized samples with nominal compositions corresponding to the following formulas: (A) $LaMnO_3$, (B) $LaMn_{0.9}Ru_{0.1}O_3$, (C) $LaMn_{0.8}Ru_{0.2}O_3$, (D) $LaMn_{0.7}Ru_{0.3}O_3$ and (E) $LaMn_{0.6}Ru_{0.4}O_3$. Vertical sticks denote calculated Bragg positions for rhombohedral and cubic phases, (F) fraction of phases in the synthesized compounds obtained by Rietveld refinement.

doped LMO perovskite structure, the Mn atoms are in the Wyckoff position 1a (0, 0, 0), La in 1b (0.5, 0.5, 0.5), O in 3d (0.5, 0, 0). From the Rietveld refinement of PXRD patterns of all the catalysts, it is confirmed that the parent compound fits rhombohedral phase while with

progressive Ru doping, there exists mixed rhombohedral and cubic phases. Figure **3.2(A – E)** shows the Rietveld refinement of the PXRD patterns of the synthesized $LaMn_{1-x}Ru_xO_3$ (x = 0.0 – 0.4), whereas Figure **3.2F** shows the fraction of rhombohedral and cubic phases in $LaMn_{1-x}Ru_xO_3$ (x = 0.0 – 0.4) obtained from Rietveld refinement. In Table **3.1**, the detailed values of refined lattice parameters, atomic positions of La, Mn/Ru and O of $LaMn_{1-x}Ru_xO_3$ (x = 0.0 – 0.4), values of R_p, R_{wp}, R_{exp} and goodness of fitting (χ^2) are tabulated. The cell parameters and volume of the unit cell of LMO obtained from Rietveld refinement are also shown in Table **3.1**. The cell volume of the cubic phase increases linearly with Ru doping in LMO. In rhombohedral structure, the angle between Mn–O–Mn is 160° – 165°, but in a cubic structure, due to steric pressure induced by the ruthenium doping, it is shifted to 180°. From the refinement of the PXRD data, we get that with an increase in Ru doping in LMO, the ratio of rhombohedral phase to the cubic phase is decreasing proportionally and in $LaMn_{0.6}Ru_{0.4}O_3$ the rhombohedral phase is almost decreased to 1%.

Table 3.1 Structural parameters obtained by Rietveld refinement of the powder X-ray diffraction data of $LaMn_{1-x}Ru_xO_3$ (x = 0.0 – 0.4) catalysts.

$LaMn_{1-x}Ru_xO_3$	**x = 0.0**	**x = 0.1**	**x = 0.2**	**x = 0.3**	**x = 0.4**
Crystal system and space group	$R\bar{3}c$	$R\bar{3}c + Pm\bar{3}m$	$R\bar{3}c + Pm\bar{3}m$	$R\bar{3}c + Pm\bar{3}m$	$R\bar{3}c + Pm\bar{3}m$
% of $R\bar{3}c$ phase	1	0.992	0.54	0.199	0.014
Lattice parameters ($R\bar{3}c$)					
a, Å	5.526	5.527	5.539	5.541	5.542
b, Å	5.526	5.527	5.539	5.541	5.542
c, Å	13.350	13.352	13.356	13.337	13.319
Cell volume, Å^3	353.02	353.234	354.936	354.513	354.355
Lattice parameters ($Pm\bar{3}m$)					
a = b = c, Å	-	3.808	3.831	3.899	3.904
Cell volume, Å^3	-	55.204	56.230	59.263	59.481
Atomic positions ($R\bar{3}c$)					
La					
x	0.0000	0.0000	0.0000	0.0000	0.0000
y	0.0000	0.0000	0.0000	0.0000	0.0000
z	0.2500	0.2500	0.2500	0.2500	0.2500
Mn/Ru					
x	0.0000	0.0000	0.0000	0.0000	0.0000
y	0.0000	0.0000	0.0000	0.0000	0.0000
z	0.0000	0.0000	0.0000	0.0000	0.0000
O					

x	0.44186	0.44506	0.44707	0.42585	0.44110
y	0.0000	0.0000	0.0000	0.0000	0.0000
z	0.2500	0.2500	0.2500	0.2500	0.2500
Atomic positions (*Pm*$\bar{3}$*m*)					
La					
x	-	0.5000	0.5000	0.5000	0.5000
y	-	0.5000	0.5000	0.5000	0.5000
z	-	0. 5000	0. 5000	0. 5000	0. 5000
Mn/Ru					
x	-	0.0000	0.0000	0.0000	0.0000
y	-	0.0000	0.0000	0.0000	0.0000
z	-	0.0000	0.0000	0.0000	0.0000
O					
x	-	0.5000	0.5000	0.5000	0.5000
y	-	0.0000	0.0000	0.0000	0.0000
z	-	0.0000	0.0000	0.0000	0.0000
R_{wp}	31.1	24.4	28.8	25.9	26.6
R_p	42.2	25.3	30.2	25.5	26.4
R_{exp}	17.97	14.55	13.98	11.63	12.47
χ^2	3.0	2.81	4.26	4.96	4.56

3.3.2 X-ray Photoelectron Spectroscopy (XPS) Spectra

The surface properties as well as the different oxidation states of the constituent elements of $LaMnO_3$ and $LaMn_{0.7}Ru_{0.3}O_3$ were investigated by XPS. Figure **3.3** represents (A) XPS survey spectra of $LaMnO_3$, (B) deconvoluted Mn $2p_{3/2}$ peak, inset to (B) shows the Mn 2p core level spectra, (C) deconvoluted Mn 3s core level spectra and (D) deconvoluted O 1s core level spectra of $LaMnO_3$. Whereas, Figure **3.4** represents (A) deconvoluted Mn $2p_{3/2}$ peak, inset to (A) shows the Mn 2p core level spectra, (B) deconvoluted Mn 3s core level spectra, (C) deconvoluted O 1s core level spectra and (D) deconvoluted Ru $3p_{3/2}$ spectra of $LaMn_{0.7}Ru_{0.3}O_3$. We first analyze the O1s XPS spectrum of $LaMnO_3$ and $LaMn_{0.7}Ru_{0.3}O_3$. Deconvolution of O 1s peak shows that this peak consists of three peaks positioned at 529.7 eV, 531 eV and 532.8 eV corresponding to the surface lattice oxygen ($O_{latt.}$), adsorbed oxygen ($O_{ads.}$viz, O^-, O^{2-} or O_2^{2-}) and adsorbed molecular water, respectively.[38] Next we compare the Mn 2p XPS spectrum of $LaMnO_3$ and $LaMn_{0.7}Ru_{0.3}O_3$ in order to obtain the oxidation states of Mn (Figure **3.3(B)** & Figure **3.4(A)** respectively). It is observed that the doublet peak energy separation ($\Delta E_{B.E.}$ = B.E. $2p_{1/2}$ – B.E. $2p_{3/2}$) of $LaMnO_3$ is 11.3 eV which is smaller than the value calculated (11.7 eV) for $LaMn_{0.7}Ru_{0.3}O_3$. This is expected since the spin-orbit

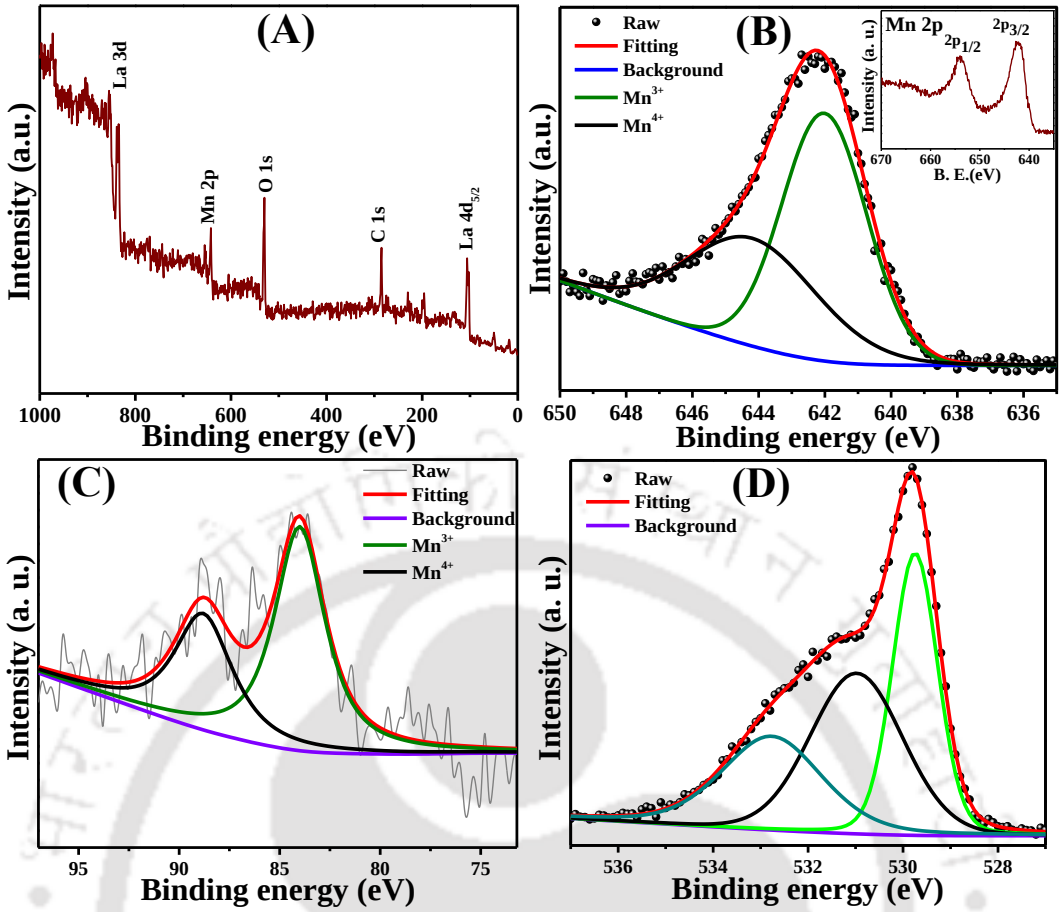

Figure 3.3 (A) XPS survey spectra, (B) deconvoluted Mn $2p_{3/2}$ peak, inset to (B) is the Mn 2p core level spectra, (C) deconvoluted Mn 3s core level spectra and (D) deconvoluted O 1s core level spectra of $LaMnO_3$.

coupling constant of Ru is higher than that of Mn, as a result, the introduction of 30% Ru at the site of Mn in $LaMnO_3$ influences the separation of doublet peak of Mn 2p. Besides, the Mn 2p peak is asymmetric in nature, which suggests Mn exits in the mixed valence state. For the precise evaluation of oxidation state of Mn, we have deconvoluted the Mn $2p_{3/2}$ peak. It is noted from the deconvoluted data that the Mn $2p_{3/2}$ peak consists of two peaks at the position of 642.1 eV and 643.6 eV in the case of $LaMnO_3$ and at the position of 641.9 eV and 643.8 eV for $LaMn_{0.7}Ru_{0.3}O_3$, suggesting Mn exits in mixed valence states of Mn (III) and Mn (IV).[39] Further evidence pertaining to the mixed valence state is supported by the Mn 3s XPS data shown in Figure **3.3(C)** & Figure **3.4(B)** corresponding to the $LaMnO_3$ and $LaMn_{0.7}Ru_{0.3}O_3$, respectively. These peaks could be deconvoluted into two peaks at binding energy (B.E.) = 84 eV and 88.8 eV which proves the average oxidation state of Mn species is about 3.4 in this compound.[40] On the other hand, it is expected that Ru should also exist in the mixed valence state for the charge neutralization of the molecule. In order to examine the

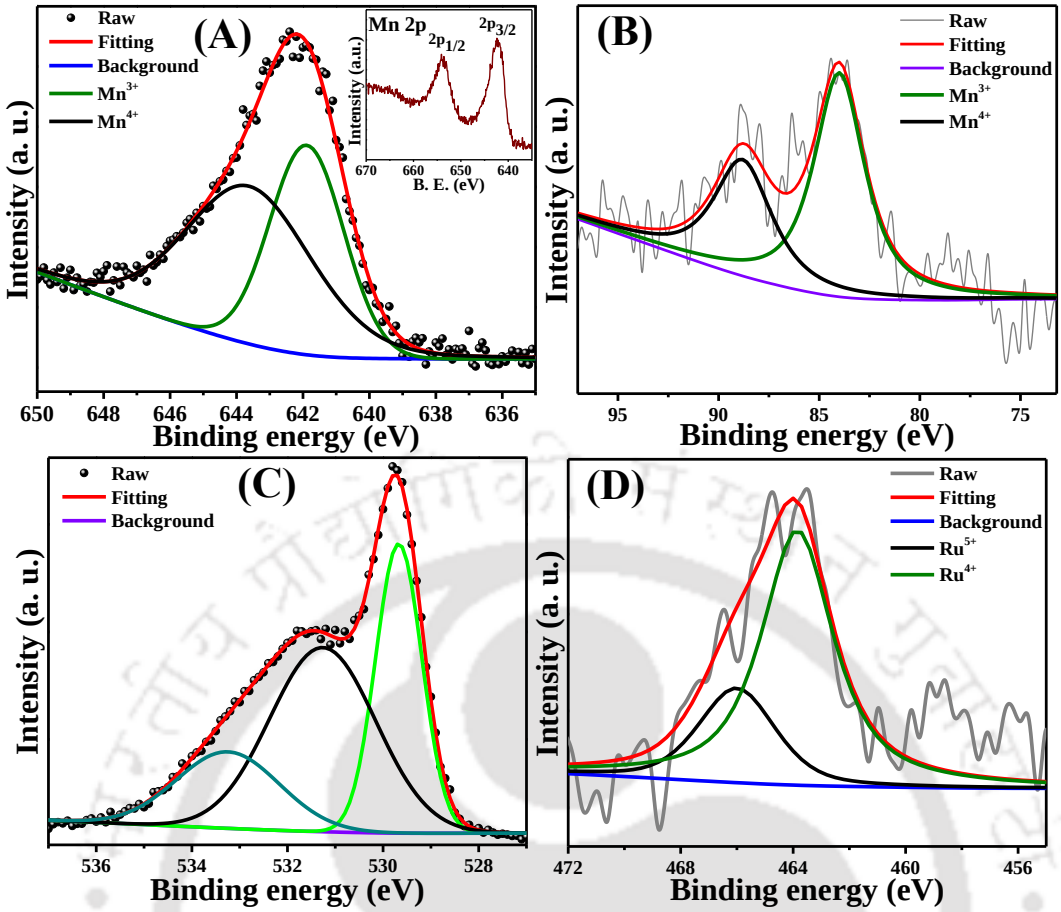

Figure 3.4 (A) Deconvoluted Mn $2p_{3/2}$ peak, inset to (A) is the Mn 2p XPS core level spectra, (B) deconvoluted Mn 3s core level spectra, (C) deconvoluted O 1s core level spectra and (D) deconvoluted Ru $3p_{3/2}$ spectra of $LaMn_{0.7}Ru_{0.3}O_3$.

mixed valence Ru states, the Ru 3p core level spectrum has been investigated. In Figure **3.4(D)**, the data shows that Ru $3p_{3/2}$ XPS peak could be deconvoluted into two peaks with B.E. = 464 eV and 466.1 eV. Such binding energy values indicate that Ru exists in the Ru (IV) and Ru (V) oxidation states.[41] From the above analysis of the XPS data, it can be concluded that both Mn and Ru exit in mixed valence states, Mn (III) /Mn (IV) and Ru (IV) /Ru (V).

3.3.3 Fourier Transform Infrared (FTIR) Spectra

Figure **3.5** shows the FTIR spectra of $LaMn_{1-x}Ru_xO_3$ (x = 0.0 – 0.4). From literature, it is known that the band at 600 cm^{-1} corresponds to the Mn–O bond stretching mode ν_3 of the MnO_6 octahedron with O_6^h symmetry in the $LaMnO_3$,[42] and in these spectra the different vibrational modes of other manganese oxides are not present,[43] hence these synthesized materials are all chemically pure as proven by PXRD and FTIR results.[44, 45] The band at 600

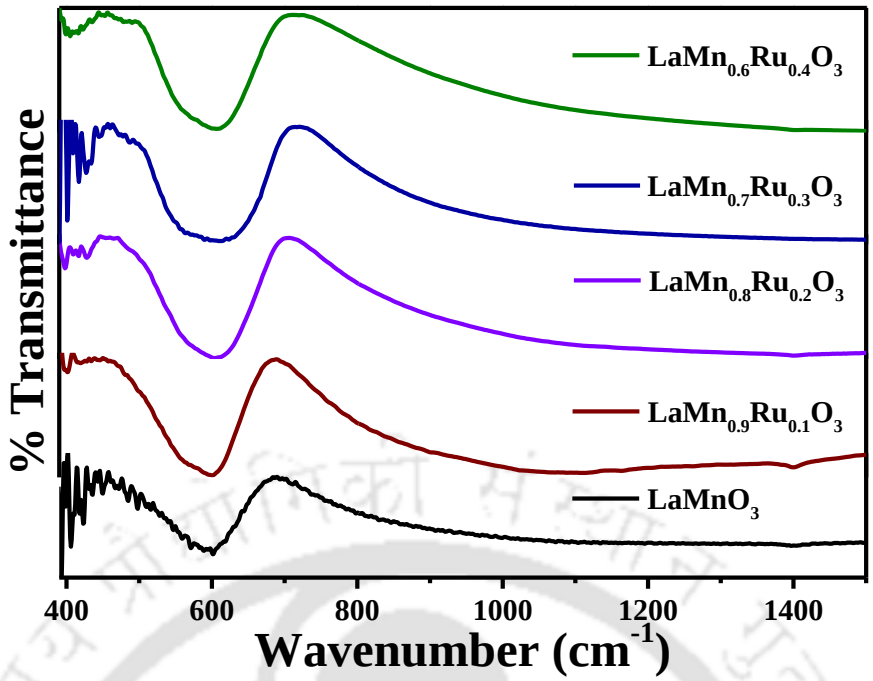

Figure 3.5 Fourier transform infrared spectra of $LaMn_{1-x}Ru_xO_3$ (x = 0.0 – 0.4).

cm^{-1} is progressively red shifted from 600 – 610 cm^{-1} with increase in Ru doping from x = 0.0 – 0.4 in $LaMn_{1-x}Ru_xO_3$. This phenomenon can be explained by the bond force constant. Ruthenium is more electronegative than that of manganese, so the doping of ruthenium can shift the Mn–O band to higher wavenumber by forming Ru–O bond.

3.3.4 Ultraviolet–visible Diffuse Reflectance Spectra and Band Gap Calculation

UV–visible diffuse reflectance spectra of all the synthesized catalysts is shown in Figure **3.6**. All the catalysts show a broad absorption feature in the whole UV-visible and extended to some portion of near IR region, which predicts that the band gap of all the catalysts must be lower than 1.5 eV. Figure **3.7** shows the calculated Tauc plots of the photocatalysts. To determine the exact band gap of semiconductors by using optical absorbance data Tauc et al. introduced a method,[46] which is-

$$(\alpha h\nu)^{\frac{1}{n}} = A(h\nu - E_g)$$

Here, α is absorption coefficient, h is Planck's constant, ν is the photon's frequency, A is a proportionality constant and E_g is the band gap of the semiconductor. The value of the exponent is related to the nature of the electronic transition. In LMO, there exist charge transfer gap (CT gap), hence the value of the exponent is taken as 2.[47] In the plot of $(\alpha h\nu)^2$ vs. hν, the point of intersection of the extrapolated tangent with the X-axis gives the value of the

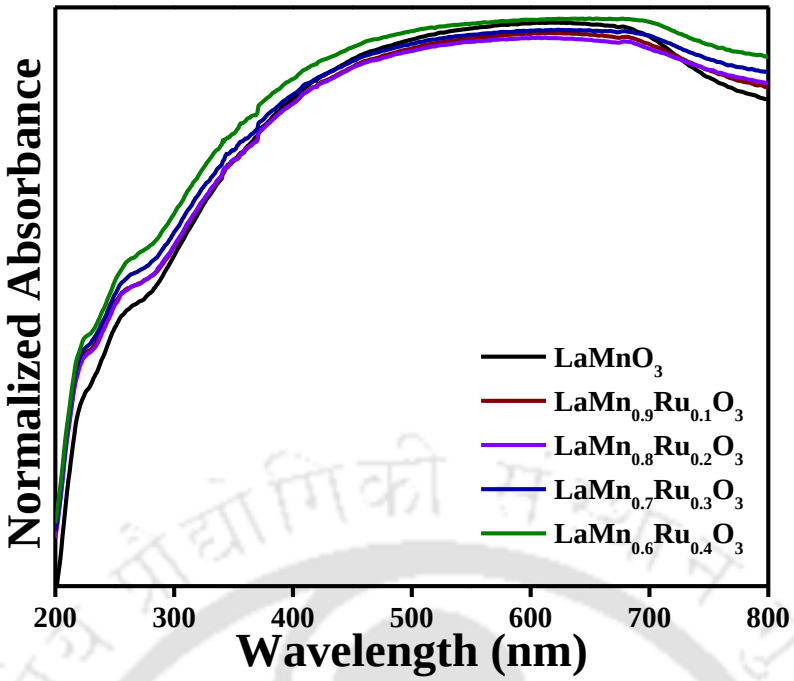

Figure 3.6 UV–visible diffuse reflectance spectra of $LaMn_{1-x}Ru_xO_3$ (x = 0.0 – 0.4).

E_g. The examined calculation is a semi-empirical method, involving some ambiguity, and the band position obtained may be slightly lacking inaccuracy. Nevertheless, the calculated values of the band gap almost match with the previously reported values by T.Arima *et.al.*[47]

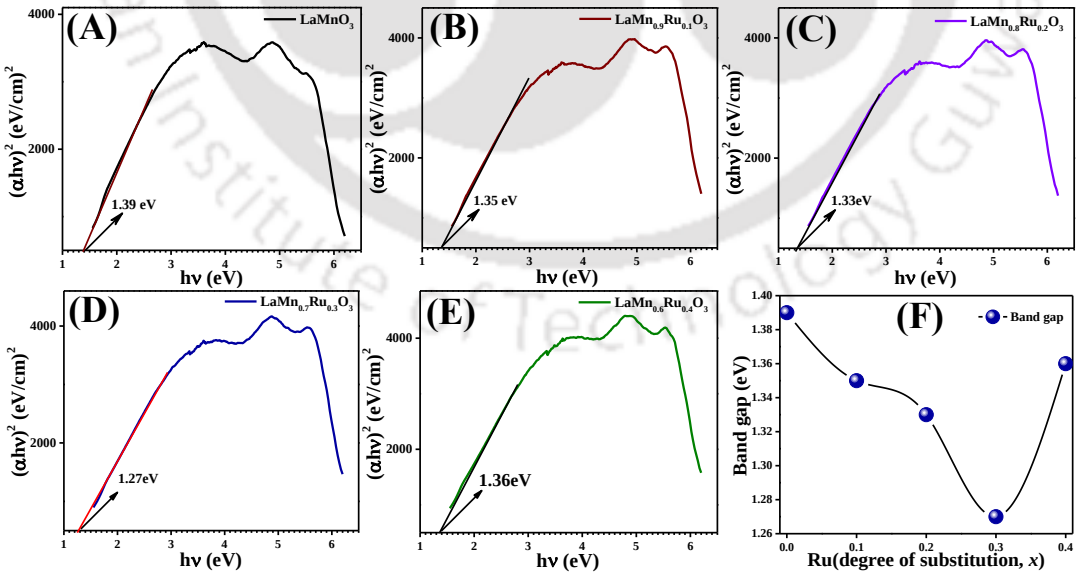

Figure 3.7 Tauc plot and estimated band gap values of (A) $LaMnO_3$, (B) $LaMn_{0.9}Ru_{0.1}O_3$, (C) $LaMn_{0.8}Ru_{0.2}O_3$, (D) $LaMn_{0.7}Ru_{0.3}O_3$, (E) $LaMn_{0.6}Ru_{0.4}O_3$ and (F) Variation of band gap with Ru doping in LMO.

The band gap of the catalysts changes with a progressive increase in doping magnitude of Ru in Mn site of LMO. It is well known from past reports that the valence band of LMO consists of oxygen 2p orbitals, whereas the conduction band is made by Mn 3d orbitals.[48] Hybridization between metal d orbitals and oxygen 2p orbitals occur due to the similarity in energy and spatial overlap of the metal d orbitals and oxygen 2p orbitals. The increase in electronegativity of the metal enhances the magnitude of metal-oxygen hybridization by shifting the metal d orbital and oxygen 2p orbital closer in energy. This strength of hybridization controls the electronic properties of these materials.[49] Ruthenium is more electronegative than manganese. Therefore, with an increase in Ru doping level in LMO creates an additional energy level below the conduction band and lowers the band gap as well. This lowering in the band gap is observed with gradual increase in Ru doping in LMO up to $x = 0.3$. In $LaMn_{1-x}Ru_xO_3$, the number of photons absorbed by the catalysts increases with a decrease in the band gap, which subsequently increases the electron and hole density in the conduction band and valence band respectively. However, for $LaMn_{0.6}Ru_{0.4}O_3$ a sharp increase in band gap is observed. The enhancement of band gap in $LaMn_{0.6}Ru_{0.4}O_3$ could be explained by the Burstein - Moss (B – M) band-filling effect.[50, 51] The Fermi level lies in between the conduction band and valence band in a normal semiconductor. As soon as the doping level exceeds a certain limit which can fill all accessible density of states beneath the conduction band, pushes the Fermi level to higher energy and in that way eliciting an increase in the band gap of the compound.

To understand the change in the VB and CB positions with respect to Ru doping in LMO, we have calculated the VB maxima and CB minima of the catalysts by using the absolute electronegativity values of the individual atoms in $LaMn_{1-x}Ru_xO_3$ ($x = 0.0 – 0.4$). The detailed calculation of the band positions is shown in the next segment (**3.3.5**). The calculated band position and band gap values of each catalyst are shown in Table **3.2**.

3.3.5 Calculation of Band Position

The valence band position of an inorganic semiconductor can be calculated by using the following formulas reported earlier by Xu and Schoonen,[52]

$$E_{VB} = (\chi_M{}^a \chi_X{}^b)^{\frac{1}{a+b}} + \frac{1}{2}E_g - E^e \qquad \text{(i)}$$

$$\chi = \frac{1}{2}(IP + EA) \qquad \text{(ii)}$$

$$E_{CB} = E_{VB} - E_g \qquad \text{(iii)}$$

Where, E_{VB} is the valence band maxima (VBM), E_{CB} is the conduction band minima (CBM), E_g is the estimated band gap of the semiconductor evaluated from the Tauc plot, E^e is the energy of free electrons on the hydrogen scale (− 4.5 eV), χ_M and χ_X are the absolute electronegativities of *M* and *X* atoms, respectively, χ is the electronegativity of the individual atoms of the multi-atomic semiconductor, calculated by using equation (ii), [53] IP is the ionization potential and EA is the electron affinity values of each atom.

Table 3.2 Calculated values of the valence band, conduction band positions, and the band gap values of $LaMn_{1-x}Ru_xO_3$ (x = 0.0 – 0.4).

Compound	Valence band maxima(eV)	Conduction band minima (eV)	Band gap (eV)
$LaMnO_3$	1.501	0.111	1.39
$LaMn_{0.9}Ru_{0.1}O_3$	1.51	0.160	1.35
$LaMn_{0.8}Ru_{0.2}O_3$	1.529	0.199	1.33
$LaMn_{0.7}Ru_{0.3}O_3$	1.528	0.258	1.27
$LaMn_{0.6}Ru_{0.4}O_3$	1.602	0.242	1.36

3.3.6 Material Morphology and Elemental Analysis

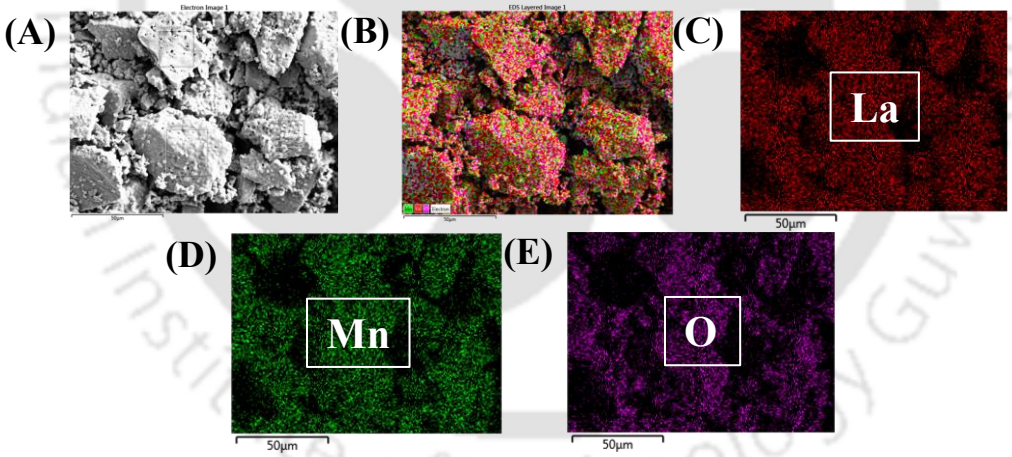

Figure 3.8 (A) FESEM image of $LaMnO_3$, (B) EDX mapping of (A), elemental distribution of (C) La, (D) Mn, and (E) O in (B).

The morphology of the prepared $LaMnO_3$ and $LaMn_{0.7}Ru_{0.3}O_3$ compounds was observed by field emission scanning electron microscopic (FESEM) images. These compounds show similar kind of morphologies with significant amount of aggregation and form large clusters that is well known for these kind of compounds made by conventional solid-state route. The FESEM image of $LaMnO_3$ and $LaMn_{0.7}Ru_{0.3}O_3$ is shown in Figure **3.8(A)** and Figure **3.9(A)**. It is clearly visible that in these compounds the particles are aggregate to form clusters.

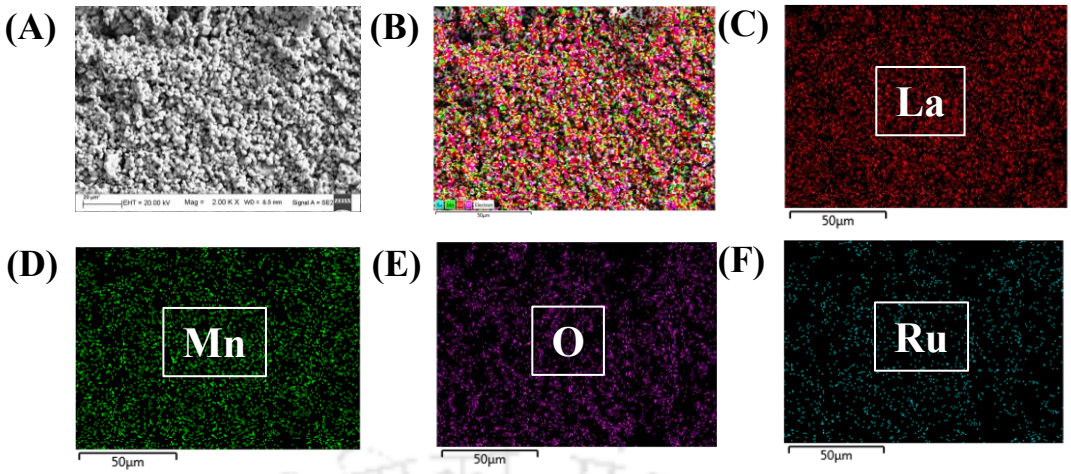

Figure 3.9 (A) FESEM image of $LaMn_{0.7}Ru_{0.3}O_3$, (B) EDX mapping of (A), elemental distribution of (C) La, (D) Mn, (E) O and (F) Ru in (B).

To check for the homogeneous elemental distribution in the compounds, energy-dispersive X-ray (EDX) spectroscopic mapping was carried out. Figure **3.8(B)** shows the elemental distribution of the parent compound $LaMnO_3$ and Figure **3.8(C – E)** show the distribution of La, Mn, and O, respectively in the Figure **3.8(B)** scan area. It is observed that all the elements are evenly distributed throughout the sample. Figure **3.9(B)** shows the elemental distribution of the best performing compound $LaMn_{0.7}Ru_{0.3}O_3$ and Figure **3.9(C – F)** show the distribution of La, Mn, O and Ru respectively in the Figure **3.9B** scan area. It is observed that all the elements are evenly distributed throughout the sample.

3.3.7 Photocatalytic Water Oxidation and Dye Degradation

In the artificial photosynthesis, top edge of valence band has to be more positive than the redox potential of H_2O/O_2 (1.23 V vs. NHE), whereas, the bottom edge of conduction band of the photocatalyst has to be more negative than the redox potential of H^+/H_2 (0 V vs. NHE) for efficient hydrogen and oxygen generation from water.[31] It is noteworthy that in $LaMn_{1-x}Ru_xO_3$ (x = 0.0 – 0.4), the valence band is lying well below the oxidation potential of H_2O/O_2 which enables oxygen production favorably. Movement of holes to the surface reaction sites of the photocatalyst depends on the transport phenomenon of the system. The availability of photogenerated charge carriers in perovskite materials depends on the Mn–O–Mn bond alignment, where the bond angle should be 180° for a feasible charge transfer. The Rietveld refined data of the PXRD patterns of the synthesized $LaMn_{0.7}Ru_{0.3}O_3$ shows that the main phase is cubic (80%) with only 20% of rhombohedral phase. From the Tauc plots, we have seen that $LaMn_{0.7}Ru_{0.3}O_3$ has the lowest band gap (1.27eV) among all $LaMn_{1-x}Ru_xO_3$

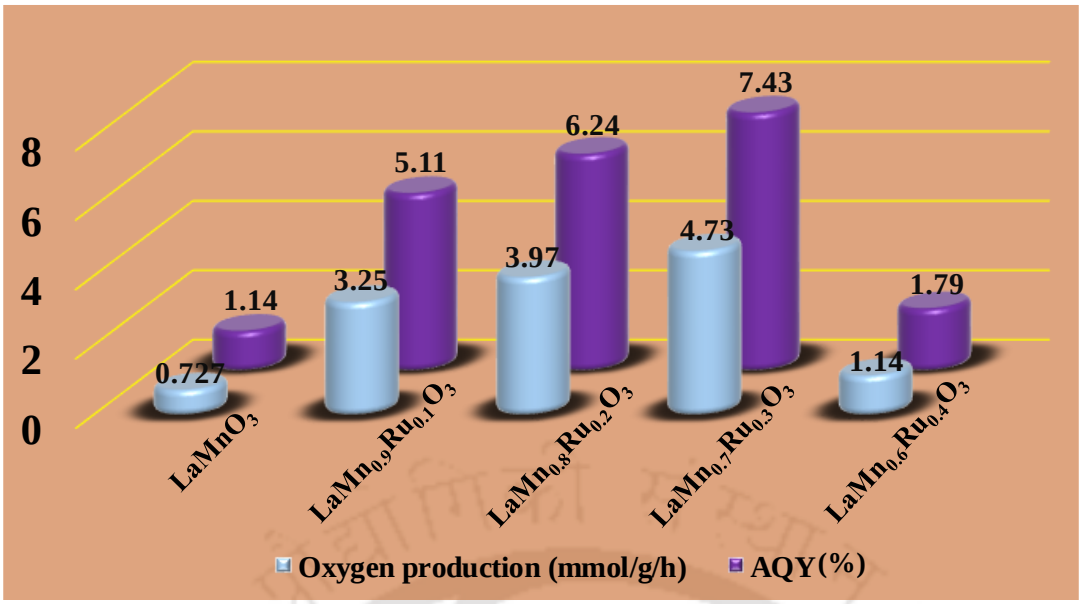

Figure 3.10 Photocatalytic oxygen production values of $LaMn_{1-x}Ru_xO_3$ (x = 0.0 – 0.4) under visible light irradiation and their respective AQY values.

(x = 0.0 – 0.4). A decrease in band gap enhances the amount of light absorption of the photocatalyst, while, the presence of two different phases in a compound may facilitate the photogenerated charge carrier transfer and reduce electron-hole recombination by inhibiting the back electron transfer through the interfacial region.[54] In this study, $LaMn_{0.7}Ru_{0.3}O_3$ acts as the best performing catalyst to produce the highest amount of oxygen from water owing to the lowest band gap and presence of 20% of rhombohedral phase along with 80% of cubic phase, which may serve as the best interfacial barrier for electron and hole recombination among all the synthesized catalysts. Figure **3.10** shows the photocatalytic oxygen production and calculated AQY values of $LaMn_{1-x}Ru_xO_3$ (x = 0.0 – 0.4). $LaMn_{0.7}Ru_{0.3}O_3$ shows highest photocatalytic activity in oxygen production at a rate of 4.73 mmol/h/g in comparison to $LaMnO_3$ (0.727 mmol/h/g), $LaMn_{0.9}Ru_{0.1}O_3$ (3.25 mmol/h/g), $LaMn_{0.8}Ru_{0.2}O_3$ (3.97 mmol/h/g) and $LaMn_{0.6}Ru_{0.4}O_3$ (1.14 mmol/h/g). The as calculated AQY of $LaMn_{0.7}Ru_{0.3}O_3$ is ~7.43% which is also highest among all other catalysts, viz., $LaMnO_3$ (~1.14%), $LaMn_{0.9}Ru_{0.1}O_3$ (~5.11%), $LaMn_{0.8}Ru_{0.2}O_3$ (~6.24%) and $LaMn_{0.6}Ru_{0.4}O_3$ (~1.79%).

In general, the photocatalytic dye degradation takes place by the following mechanism.[55, 56] When photocatalyst absorbs light of suitable energy, it creates photogenerated electrons (e^-_{CB}) and holes (h^+_{VB}) by promoting electron from the valence band to the conduction band leaving hole in the valence band. These photogenerated electrons and holes with sufficient lifetime and velocity reaches to the catalyst surface to undergo redox reactions with the species near

the surface. Photogenerated holes (h^{+}_{VB}) react with H_2O near the catalyst surface to produce hydroxyl ($OH^{\cdot}$) radicals, while, photogenerated electrons (e^{-}_{CB}) produce superoxide radical anion ($O_2^{\cdot -}$). Hydrogen peroxide is formed by the combination of these newly formed $OH^{\cdot}$ radicals, which in turn produce $OH^{\cdot}$ radicals by reacting with $O_2^{\cdot -}$. And mainly these $OH^{\cdot}$ radicals are responsible for the decomposition and discoloration of the organic dye.

Figure **3.11** shows the efficiency of photocatalytic methyl orange (MO) dye degradation of $LaMn_{1-x}Ru_xO_3$ (x = 0.0 – 0.4) at pH 2.5. It is well known that MO is a very stable dye under normal conditions and tough to degrade or decolor it. In recent past, few research groups have shown that in acidic pH MO dye decolors easily than in alkaline or neutral pH in the presence of a photocatalyst.[57, 58] Hence, we carried out the dye degradation experiment at an acidic pH of 2.5. The plot of ratio of residual concentration (C) to initial concentration (C_0) versus time of all the compositions are shown in Figure **3.11**. Prior to illumination, the catalyst in the dye solution was allowed to stir in the dark for 15 minutes in order to obtain adsorption-desorption equilibrium. The decrease in concentration of the dye solution due to adsorption prior to irradiation is plotted as −15 to 0 minutes in the time scale in Figure **3.11**. The change in concentration after irradiation is shown after 0 minute. It is observed that the dye solution is

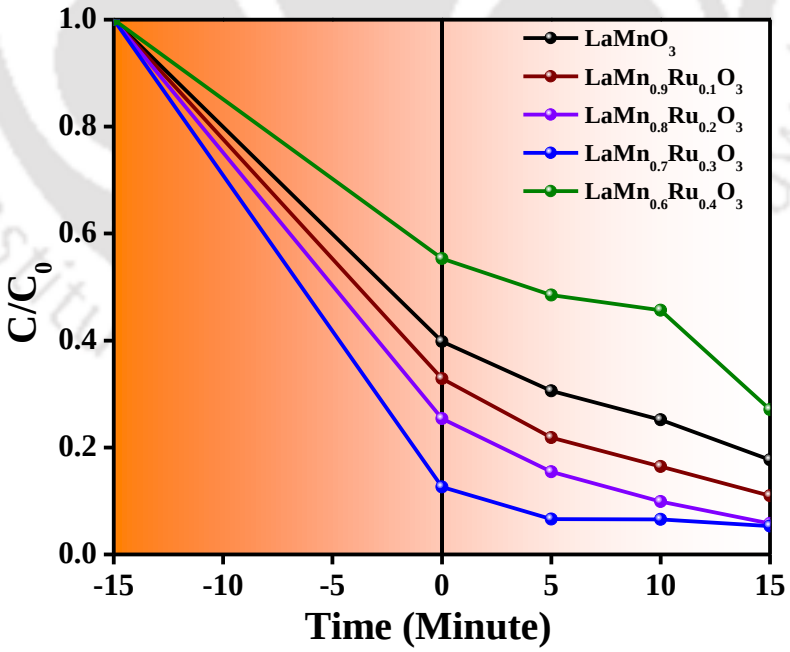

Figure 3.11 Photocatalytic MO dye degradation of $LaMn_{1-x}Ru_xO_3$ (x = 0.0 – 0.4) at pH 2.5.

almost completely degraded in 15 minutes. It is seen that the catalyst with composition $LaMn_{0.7}Ru_{0.3}O_3$ shows the highest efficiency in dye degradation which is due to the lowest band gap as well as presence of two phases (80% of cubic and 20% of rhombohedral) which can facilitate superior surface reactions by photogenerated carriers by suppressing the recombination effect.

3.4 CONCLUSIONS

In summary, this work reports for the first time the synthesis of $LaMn_{1-x}Ru_xO_3$ ($x = 0.0 – 0.4$) and its use as a photocatalyst for water oxidation as well as dye degradation. The PXRD results show that the doped compounds have both rhombohedral and cubic phases. Rietveld refinement studies of the PXRD of the compounds confirm the reduction of lattice distortion as well increase in Mn–O–Mn bond angle to 180° with a progressive increase in ruthenium doping, which facilitates the charge carrier movement of the catalysts. Variations in band gap, as well as different redox reactions taking place due to doping are studied. $LaMn_{0.7}Ru_{0.3}O_3$ having lowest bandgap among all the synthesized catalysts and consisting of 80% cubic and 20% rhombohedral phase, shows the highest efficiency of oxygen production (at a rate of 4.73 mmol/h/g) with an AQY of 7.43 % and dye (MO) degradation.

3.5 REFERENCES

1. Lee, Y.; Suntivich, J.; May, K. J.; Perry, E. E.; Shao-Horn, Y. *J. Phys. Chem. Lett.* **2012**, *3*, 399.
2. Christoforidis, K. C.; Fornasiero, P. *ChemCatChem* **2017**, *9*, 1523.
3. Yi, Z.; Ye, J.; Kikugawa, N.; Kako, T.; Ouyang, S.; Stuart-Williams, H.; Yang, H.; Cao, J.; Luo, W.; Li, Z. *Nat. Mater.* **2010**, *9*, 559.
4. Li, H.; Shang, J.; Zhu, H.; Yang, Z.; Ai, Z.; Zhang, L. *ACS Catal.* **2016**, *6*, 8276.
5. Kudo, A.; Ueda, K.; Kato, H.; Mikami, I. *Catal. Letters* **1998**, *53*, 229.
6. Suntivich, J.; May, K. J.; Gasteiger, H. A; Goodenough, J. B.; Shao-Horn, Y. *Science.* **2011**, *334*, 2010.
7. Wang, S. L.; Mak, Y. L.; Wang, S.; Chai, J.; Pan, F.; Foo, M. L.; Chen, W.; Wu, K.; Xu, G. Q. *Langmuir* **2016**, *32*, 13046.
8. Meadowcroft, D. B *Nature* **1970**, *226*, 847.
9. Nishihata, Y. *Nature* **2002**, *418*, 164.
10. Sayama, K.; Mukasa, K.; Abe, R.; Abe, Y.; Arakawa, H. *Chem. Commun*. **2001**, 2416.
11. Gao, F.; Chen, X.; Yin, K.; Dong, S.; Ren, Z.; Yuan, F.; Yu, T.; Zou, Z.; Liu, J. M. *Adv. Mater.***2007**, *19*, 2889.

12. Parida, K. M.; Reddy, K. H.; Martha, S.; Das, D. P.; Biswal, N. *Int. J. Hydrogen Energy* **2010**, *35*, 12161.
13. Alifanti, M.; Auer, R.; Kirchnerova, J.; Thyrion, F.; Grange, P.; Delmon, B. *Appl. Catal., B* **2003**, *41*, 71.
14. Peña, M. A.; Fierro, J. L. G. *Chem. Rev.* **2001**, *101*, 1981.
15. Dai, H.; He, H.; Li, P.; Gao, L.; Au, C. T. *Catal. Today* **2004**, *90*, 231.
16. Kida, T.; Guan, G.; Minami, Y.; Ma, T.; Yoshida, *J. Mater. Chem.* **2003**, *13*, 1186.
17. Najjar, H.; Batis, H. *Appl. Catal., A* **2010**, *383*, 192.
18. Irusta, S.; Pina, M. P.; Menendez, M.; Santamaria, J. *J. Catal.* **1998**, *179*, 400.
19. Blasin-Aubé, V.; Belkouch, J.; Monceaux, L. *Appl. Catal., B* **2003**, *43*, 175.
20. Zhang, R.; Luo, N.; Yang, W.; Liu, N.; Chen, B. *J. Mol. Catal., A* **2013**, *371*, 86.
21. Ishihara, T. *Perovskite Oxide for Solid Oxide Fuel Cells. Springer, Berlin*, **2009**.
22. Hu, J.; Wang, L.; Shi, L.; Huang, H. *Electrochim. Acta* **2015**, *161*, 115.
23. Ghiasi, M.; Delgado-Jaime, M. U.; Malekzadeh, A.; Wang, R.-P.; Miedema, P. S.; Beye, M.; de Groot, F. M. F. *J. Phys. Chem. C* **2016**, *120*, 8167.
24. Chen, X.; Cai, Q.; Wang, W.; Chen, Z.; Wu, Z.; Wu, Z.; Feng, C.; Li, Q. *J. Phys. Chem. C* **2007**, *111*, 4512.
25. Keav, S.; Matam, S. K.; Ferri, D.; Weidenkaff, A. *Catalysts* **2014**, *4*, 226.
26. Mueller, D. N.; Machala, M. L.; Bluhm, H.; Chueh, W. C. *Nat. Commun.* **2015**, *6*, 6097.
27. Vojvodic, A.; Nørskov, J. K. *Science* **2011**, *334*, 1355.
28. Ohno, T.; Tanigawa, F.; Fujihara, K.; Izumi, S.; Matsumura, M. *J. Photochem. Photobiol., A* **1999**, *127*, 107.
29. Houskova, V.; Stengl, V.; Bakardjieva, S.; Murafa, N.; Tyrpekl, V. *App. Catal., B* **2009**, *89*, 613.
30. Malavasi, L.; Mozzati, M. C.; Tealdi, C.; Azzoni, C. B.; Flor, G. *J. Phys. Chem. B* **2005**, *109*, 20707.
31. Patra, A. S.; Kumar, N. V.; Barpuzary, D.; De, M.; Qureshi, M. *Mater. Lett.* **2014**, *131*, 125.
32. Kuznetsov, M. V; Parkin, I. P.; Caruana, D. J.; Morozov, Y. G. *J. Mater. Chem.* **2004**, *14*, 1377.
33. Maurin, I.; Barboux, P.; Lassailly, Y.; Boilot, J. P.; Villain, F.; Dordor, P. *J. Solid State Chem.* **2001**, *160*, 123.
34. Pi, L.; Hébert, S.; Martin, C.; Maignan, A.; Raveau, B. *Phys. Rev. B* **2003**, *67*, 024430.
35. Sahu, R. K.; Hu, Z.; Rao, M. L.; Manoharan, S. S.; Schmidt, T.; Richter, B.; Knupfer, M.; Golden, M.; Fink, J.; Schneider, C. M. *Phys. Rev. B* **2002**, *66*, 144415.
36. Wang, L. M.; Lai, J. -H.; Wu, J. -I.; Kuo, Y. -K.; Chang, C. L. *J. Appl. Phys.* **2007**, *102*, 023915.
37. Zhou, W.; Sunarso, J. *J. Phys. Chem. Lett.* **2013**, *4*, 2982.

38. Liu, Y.; Dai, H.; Deng, J.; Zhang, L.; Zhao, Z.; Li, X.; Wang, Y.; Xie, S.; Yang, H.; Guo, G. *Inorg. Chem.* **2013**, *52*, 8665.
39. Reitz, C.; Leufke, P. M.; Schneider, R.; Hahn, H.; Brezesinski, T. *Chem. Mater.* **2014**, *26*, 5745.
40. Wang, Y.; Xie, S.; Deng, J.; Deng, S.; Wang, H.; Yan, H.; Dai, H. *ACS Appl. Mater. Interfaces* **2014**, *6*, 17394.
41. Berti, G.; Sanna, S.; Castellano, C.; Van Duijn, J.; Ruiz-Bustos, R.; Bordonali, L.; Bussetti, G.; Calloni, A.; Demartin, F.; Duò, L.; Brambilla, A. *J. Phys. Chem. C* **2016**, *120*, 11763.
42. Kebin, L.; Xijun, L.; Kaigui, Z.; Jingsheng, Z.; Yuheng, Z. *J. Appl. Phys.* **1997**, *81*, 6943.
43. Julien, C. M.; Massot, M.; Poinsignon, C. *Spectrochim. Acta, Part A* **2004**, *60*, 689.
44. Zhou, X.; Xue, J.; Zhou, D.; Wang, Z.; Bai, Y.; Wu, X.; Liu, X.; Meng, J. *ACS Appl. Mater. Interfaces* **2010**, *2*, 2689.
45. Gao, F.; Lewis, R.; Wang, X. L.; Dou, S. X. *J. Alloys Compd.* **2002**, *347*, 314.
46. Tauc, J.; Grigorovici, R.; Vancu, A. *Phys. Status Solidi* **1966**, *15*, 627.
47. Arima, T.; Tokura, Y. *J. Phys. Soc. Jpn.* **1995,** *64*, 2488.
48. Santoni, A.; Speranza, G.; Mancini, M. R.; Padella, F.; Petrucci, L.; Casadio, S. *J. Phys. Condens. Matter* **1999**, *11*, 3387.
49. Hong, W. T.; Risch, M.; Stoerzinger, K. A.; Grimaud, A.; Suntivich, J.; Shao-Horn, Y. *Energy Environ. Sci.* **2015**, *8*, 1404.
50. Burstein, E. *Phys. Rev.* **1954**, *93*, 632.
51. Moss, T. S. *Proc. Phys. Soc. Sect. B* **1954**, *67*, 775.
52. Xu, Y.; Schoonen, M. A. A. *Am. Mineral.* **2000**, *85*, 543.
53. Nethercot, A. H. *Phys. Rev. Lett.* **1974**, *33*, 1088.
54. Ismail, A. A.; Bahnemann, D. W. *Green Chem.* **2011**, *13*, 428.
55. Khan, Z.; Chetia, T. R.; Qureshi, M. *Nanoscale* **2012**, *4*, 3543.
56. Rauf, M. A.; Ashraf, S. S. *Chem. Eng. J.* **2009**, *151*, 10.
57. Ghiasi, M.; Malekzadeh, A. *Sep. Purif. Technol.* **2014**, *134*, 12.
58. Huang, M.; Xu, C.; Wu, Z.; Huang, Y.; Lin, J.; Wu, J. *Dyes Pigm.* **2008**, *77*, 327.

Chapter 4

Doped Lanthanum Manganite /Graphene Oxide Composite for Efficient and Robust Photocatalytic Water Oxidation

This chapter presents the synthesis of stable and robust $La_{1-x}Sr_xMnO_3$ (x = 0.0 – 0.5) and $La_{1-x}Sr_xMnO_3$ (x = 0.0 – 0.5) – Graphene oxide (GO) composite and its use as a photocatalyst for water oxidation. Sr doping in $LaMnO_3$ creates holes or Mn (IV) in $La_{1-x}Sr_xMnO_3$ (x = 0.0 – 0.5) lattice. Owing to doping of larger Sr ions in La site in $La_{1-x}Sr_xMnO_3$ (x = 0.0 – 0.5) changes its crystal structure from rhombohedral to cubic phase in higher Sr doping concentration and thereby make the Mn – O – Mn angle ~180° in doped compounds. Formation of holes or Mn (IV) and ~180° of Mn – O – Mn bond angle facilitates the charge transport in these compounds. The blending of GO with $La_{1-x}Sr_xMnO_3$ (x = 0.0 – 0.5) shows further enhancement in photocatalytic O_2 evolution from water due to the good charge carrier transport property of GO.

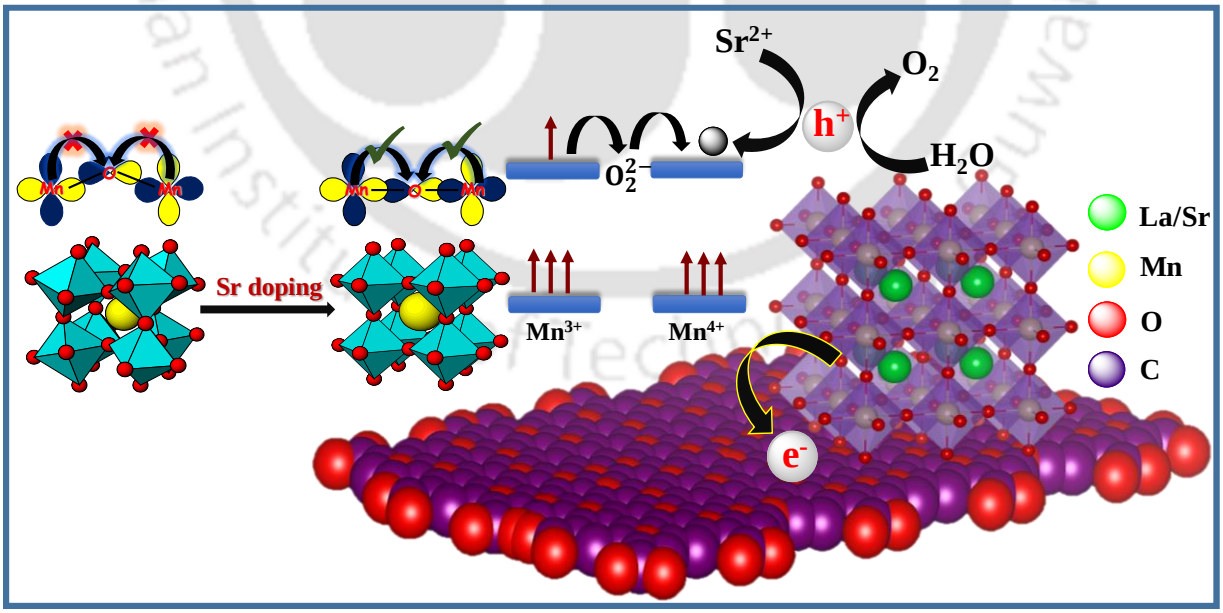

Patra *et al.*, *Mater. Lett.* **2014**, *131*, 125.

4.1 INTRODUCTION

Lanthanum manganites, as discussed in chapter 3, are one of the possible solutions where in maintaining proper stoichiometry within the compound is much easier owing to its thermal and chemical stability along with the superior conductivity at room temperature and the ease of synthesis.[1] The charge transport mechanism based on their density of states distribution in valence band and conduction band of doped manganites has been well understood along with its magnetic behavior.[2] Strontium doped Lanthanum manganite, $La_{1-x}Sr_xMnO_3$, a mixed valence perovskite oxide has gained enormous importance in a number of present technologies owing to its fascinating magnetic and transport properties along with intriguing thermal, chemical and mechanical properties. $La_{1-x}Sr_xMnO_3$ materials show room temperature metal-insulator transition with increasing Sr doping.[3] These materials have been used in solid-oxide fuel cells, magnetic sensors, catalysis, information storage, supercapacitors and so on.[4 – 10]

The rapid recombination of photogenerated charge carriers in photocatalysts hinder its catalytic efficiency. Hence, combining with suitable element doping into photocatalyst lattice, designing a photocatalyst composite with superior charge transporting material can suppress this charge carrier recombination. Graphene and its derivative, such as graphene oxide (GO) are superior charge transporting materials.[11] Graphene oxide (GO) is a layered carbon based hydrophilic material with various oxygen containing functional groups (hydroxyl, epoxy) on its basal plane as well as at the edge (carboxylic acid or carbonyl groups) of its lattice.[12 – 17] Completely oxidized graphene oxide is an insulator whereas incompletely oxidized graphene oxide is a semiconductor in nature and preceding reports says that the band gap of graphene oxide is actually controlled by the aromatic (sp^2) and aliphatic (sp^3) domains in its structure.[18 – 20] Owing to the high surface area, charge carrier separation and transport ability, GO and graphene related materials are extensively used in photocatalytic systems.[21 – 25]

In this chapter, to explore the role of A-site doping in $LaMnO_3$ (LMO) by Sr (II) in phase formation, and its consequences in photocatalytic properties, we have synthesized $La_{1-x}Sr_xMnO_3$ (x = 0.0 – 0.5) [where x is the partial substitution degree of strontium] by conventional solid-state synthesis in ambient atmosphere. To check the improved photocatalytic activity of $La_{1-x}Sr_xMnO_3$ (x = 0.0 – 0.5) we have made 1wt% GO composite of $La_{1-x}Sr_xMnO_3$ (x = 0.0 – 0.5) and found that compared to $La_{1-x}Sr_xMnO_3$ (x = 0.0 – 0.5) photocatalysts, GO composite of $La_{1-x}Sr_xMnO_3$ (x = 0.0 – 0.5) catalysts show a substantial enhancement in the photocatalytic water oxidation.

4.2 EXPERIMENTAL SECTION

4.2.1 Synthesis of $La_{1-x}Sr_xMnO_3$ (x = 0.0 – 0.5)

Strontium doped lanthanum manganites were prepared by the conventional solid-state route by using high-purity La_2O_3, $Mn(CH_3COO)_2$ and $SrCO_3$. A stoichiometric amount of the reagents were weighed accurately and ground well in an agate mortar and pestle for an hour with the help of acetone and subsequently these homogenously mixed powder of different compositions were kept in different alumina crucibles and kept inside a box furnace and calcined at 1050 °C for 12 h in air at a rate of 5 °C/min. Then the compounds were cooled down to room temperature naturally and ground again. After this process, the compounds were calcined again for 72 h at 1050 °C with several intermediate grinding.

4.2.2 Synthesis of Graphene Oxide (GO)

Graphene oxide was prepared by Hummers method through oxidation of graphite.[1] Initially, at 0 – 5 °C temperature graphite powder (0.5 g) and $NaNO_3$ (0.5g) were mixed in 30 mL of H_2SO_4 (95%). After 30 min of vigorous stirring, 1.5 g of $KMnO_4$ was added very slowly into this reaction mixture. During the addition of $KMnO_4$, the temperature of the reaction mixture was kept lower than 15 °C. After that, the reaction mixture was vigorously stirred at 35 °C for 7 h and added 50 mL of water into the reaction mixture and the color of the mixture turned faded to brown. Then the temperature was raised to 98 °C and at this temperature, the reaction mixture was stirred for another 6 h. Hence, 50 mL of water was added to this solution and lastly to remove unreacted $KMnO_4$, if any, 1 ml of H_2O_2 (30 wt %) was added to the reaction solution. To purify the reaction mixture, it was washed by centrifuging, rinsing and sonicating with 10% HCl and deionized (DI) water for several times. After centrifugation, the product was dried under vacuum at room temperature. In this process, the as-synthesized GO powders form GO nano sheets upon ultrasonic treatment. A schematic diagram of GO synthesis from graphite is shown in Scheme **4.1**.

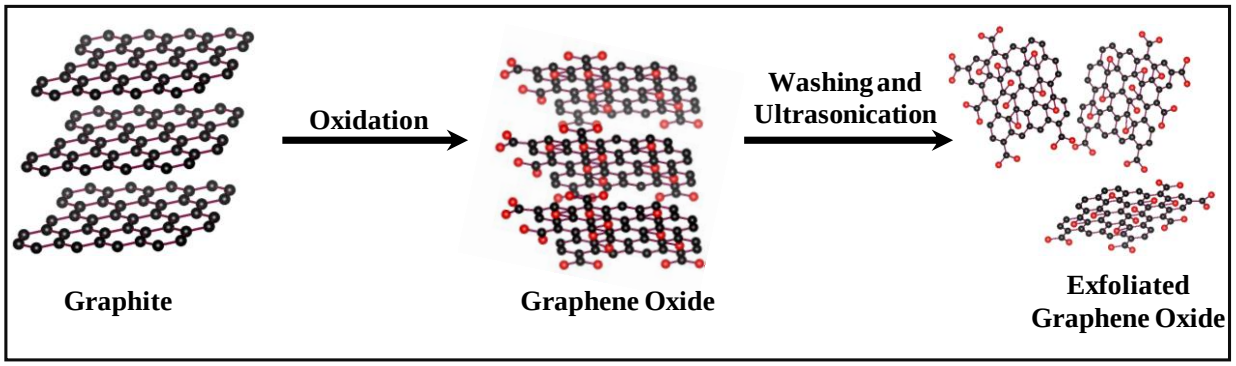

Scheme 4.1 Schematic representation of GO synthesis from graphite.[27]

4.2.3 Synthesis of $La_{1-x}Sr_xMnO_3$ (x = 0.0 – 0.5)/GO Composite Photocatalyst

$La_{1-x}Sr_xMnO_3$ (x = 0.0 – 0.5)/GO was prepared by mechanical grinding. Briefly, 0.2 g of as prepared $La_{1-x}Sr_xMnO_3$ (x = 0.0 – 0.5) compound was carefully ground with 1 wt% of as-synthesized GO by using agate mortar pestle and the motivation behind the grinding of $La_{1-x}Sr_xMnO_3$ (x = 0.0 – 0.5) and GO is to make uniform contact between them. The obtained powder of $La_{1-x}Sr_xMnO_3$ (x = 0.0 – 0.5)/GO was used for to examine the effect of graphene oxide on photocatalytic water oxidation.

4.3 RESULTS AND DISCUSSION

4.3.1 Powder X-ray Diffraction (PXRD) Patterns

The phase purity and highly crystalline perovskite structure of the as-synthesized $La_{1-x}Sr_xMnO_3$ (x = 0.0 – 0.5) were confirmed from the powder X-ray diffraction (PXRD) patterns of the samples. PXRD patterns for $La_{1-x}Sr_xMnO_3$ (x = 0.0 – 0.5) compounds after calcination at 1050 °C are shown in Figure **4.1**. The PXRD patterns of all as–synthesized compounds are indexed and the diffraction patterns are free from any impurity peaks. From the diffractogram, it is verified that the parent compound $LaMnO_3$ belongs to the rhombohedral phase with $R\bar{3}c$ space group (no. 167). From preceding reports, it is known that depending upon the reaction condition and calcination temperature, LMO can crystallize in different crystal phases such as orthorhombic, rhombohedral, cubic, monoclinic or triclinic symmetry owing to the different stoichiometry of oxygen atoms inside the lattice.[28, 29]

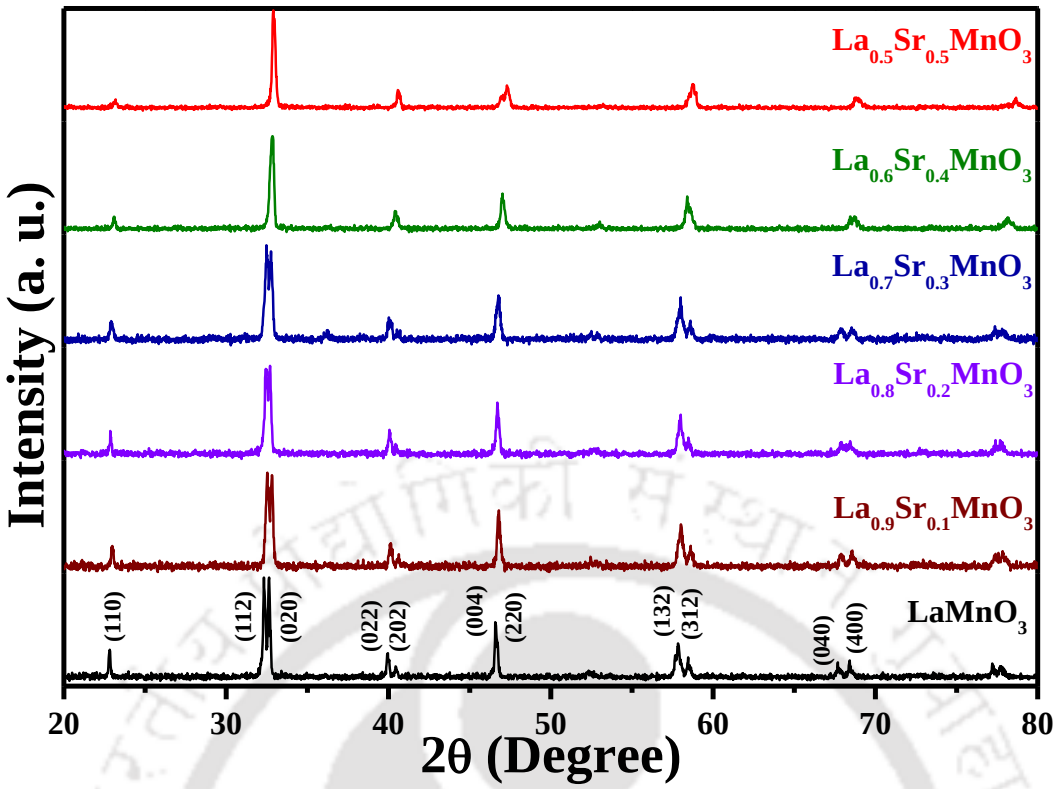

Figure 4.1 Powder X-ray diffraction pattern of all the synthesized $La_{1-x}Sr_xMnO_3$ (x = 0.0 – 0.5) catalysts.

In the rhombohedral phase of LMO, due to oxygen over stoichiometry, a fraction of Mn (III) is oxidized to Mn (IV) and hence, Mn exists in two different oxidation states – Mn (III) ($t_{2g}^3e_g^1$) and Mn (IV) ($t_{2g}^3e_g^0$).[30] The ionic radii of Sr (II) and La (III) are 132 pm and 117 pm, respectively, whereas, ionic radii of six coordinated Mn (III) and Mn (IV) are 65 pm and 52 pm, respectively. However, from Figure **4.1** we can notice that with progressive Sr doping, PXRD diffraction patterns shift towards higher diffraction angles. This could be explained by the formation of Mn (IV) ions from Mn (III) ions with Sr doping in LMO, as reported earlier.[31, 32] Doublet of the highest intensity peak at around 32.5° gradually merged to one peak with progressive Sr doping in LMO. And when x ≥ 0.4, this peak appears to be a stong peak without any splitting. This change in peak symmetry with Sr doping clearly indicates the presence of a modified crystallographic symmetry in Sr-doped LMO which may lead to the formation of cubic phase, space group $Pm\bar{3}m$ (no. 221). Daengsakul *et al.* have also reported similar kind of phenomena in $La_{1-x}Sr_xMnO_3$ synthesized by a sol-gel route.[32] The change in crystal phase may be due to the formation of more Mn (IV) ions which reduces the Mn – O bond strength compared to Mn (III) – O bond.[33]

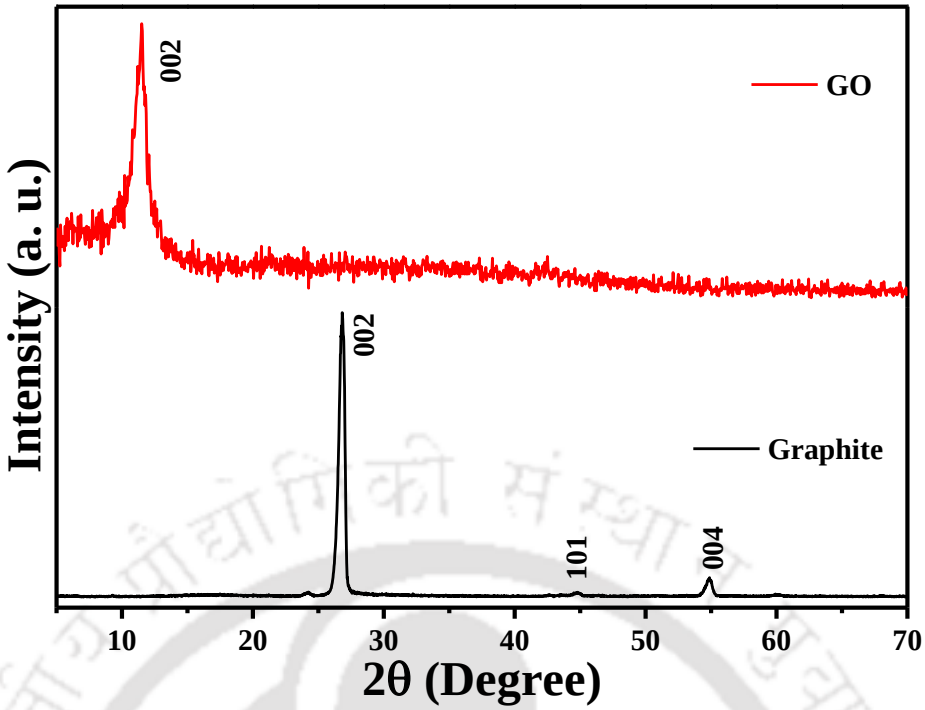

Figure 4.2 Powder X-ray diffraction pattern of used commercial graphite powder and as–synthesized GO.

Figure **4.2** shows the PXRD pattern of graphite and as-synthesized graphene oxide (GO). Commercial graphite powder showed a very strong diffraction peak at 2θ = 26.8˚ with an interlayer distance, d = 0.33 nm. Upon oxidation, a new broad diffraction peak is observed at 2θ = 11.5˚ with an interlayer distance, d = 0.76 nm and the strong diffraction peak of graphite completely disappeared, which confirms the formation of GO from graphite.

4.3.2 X-ray Photoelectron Spectroscopy (XPS) Spectra

Surface properties and the oxidation states of the component elements of $LaMnO_3$ and $La_{0.7}Sr_{0.3}MnO_3$ were investigated by XPS. Figure **4.3** represents (A) XPS survey spectra (B) deconvoluted Mn $2p_{3/2}$ peak, inset to (B) shows the Mn 2p core level spectra, and (C) deconvoluted O 1s core level spectra of $LaMnO_3$. Figure **4.4** represents (A) XPS survey spectra (B) deconvoluted Mn $2p_{3/2}$ peak, inset to (B) shows the Mn 2p core level spectra, (C) deconvoluted Sr 3d spectra, and (D) deconvoluted O 1s core level spectra of $La_{0.7}Sr_{0.3}MnO_3$. Deconvolution of O 1s spectra of $LaMnO_3$ (Figure **4.3(C)**) shows that this peak comprises of three peaks positioned at 529 eV, 530.4 eV and 532.1 eV and deconvolution of O 1s spectra of $La_{0.7}Sr_{0.3}MnO_3$ (Figure **4.4(D)**) also shows three peaks positioned at 529.1 eV, 530.8 eV,

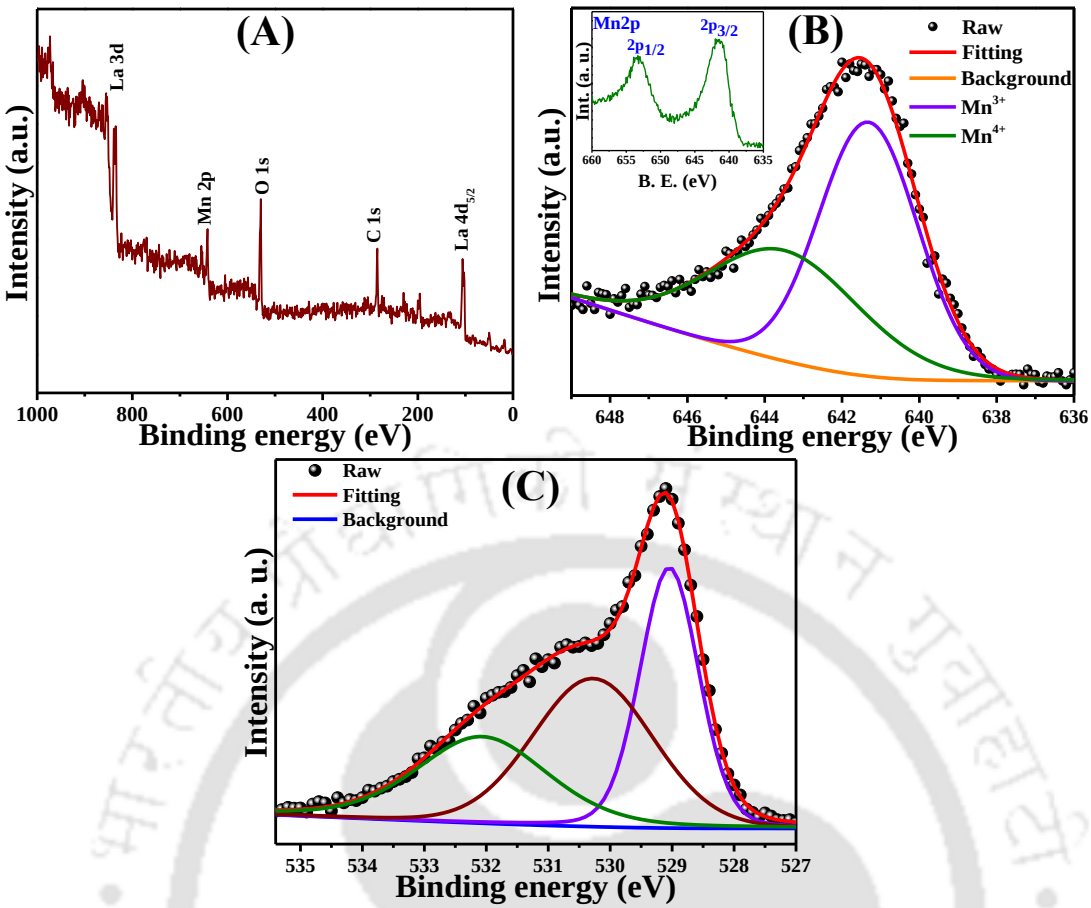

Figure 4.3 (A) XPS survey spectra, (B) deconvoluted Mn $2p_{3/2}$ peak, inset to (B) is the Mn 2p core level spectra, and (C) deconvoluted O 1s core level spectra of $LaMnO_3$.

and 532.4 eV corresponding to the surface lattice oxygen ($O_{latt.}$), adsorbed oxygen ($O_{ads.}$viz, O^-, O^{2-} or O_2^{2-}) and adsorbed molecular water, respectively.[34] Then we compare the Mn 2p XPS spectrum of $LaMnO_3$ and $La_{0.7}Sr_{0.3}MnO_3$ in order to obtain the oxidation states of Mn (Figure **4.3(B)** & Figure **4.4(B)**, respectively). The asymmetric nature of the Mn 2p peak indicates that Mn exits in the mixed valence state. To evaluate the oxidation state of Mn, we have deconvoluted the Mn $2p_{3/2}$ peak. It is noted from the deconvoluted data that the Mn $2p_{3/2}$ peak consists of two peaks at the position of 642.3 eV and 643.9 eV in case of $LaMnO_3$ and 641.5 eV and 644 eV for $La_{0.7}Sr_{0.3}MnO_3$, suggesting Mn exits in mixed valence states of Mn (III) and Mn (IV).[35] In Figure **4.4(C)**, data shows that Sr 3d XPS peak could be deconvoluted into two peaks with B.E. = 132.2 eV and 134 eV attributed to Sr $3d_{5/2}$ and Sr $3d_{3/2}$, respectively.[36]

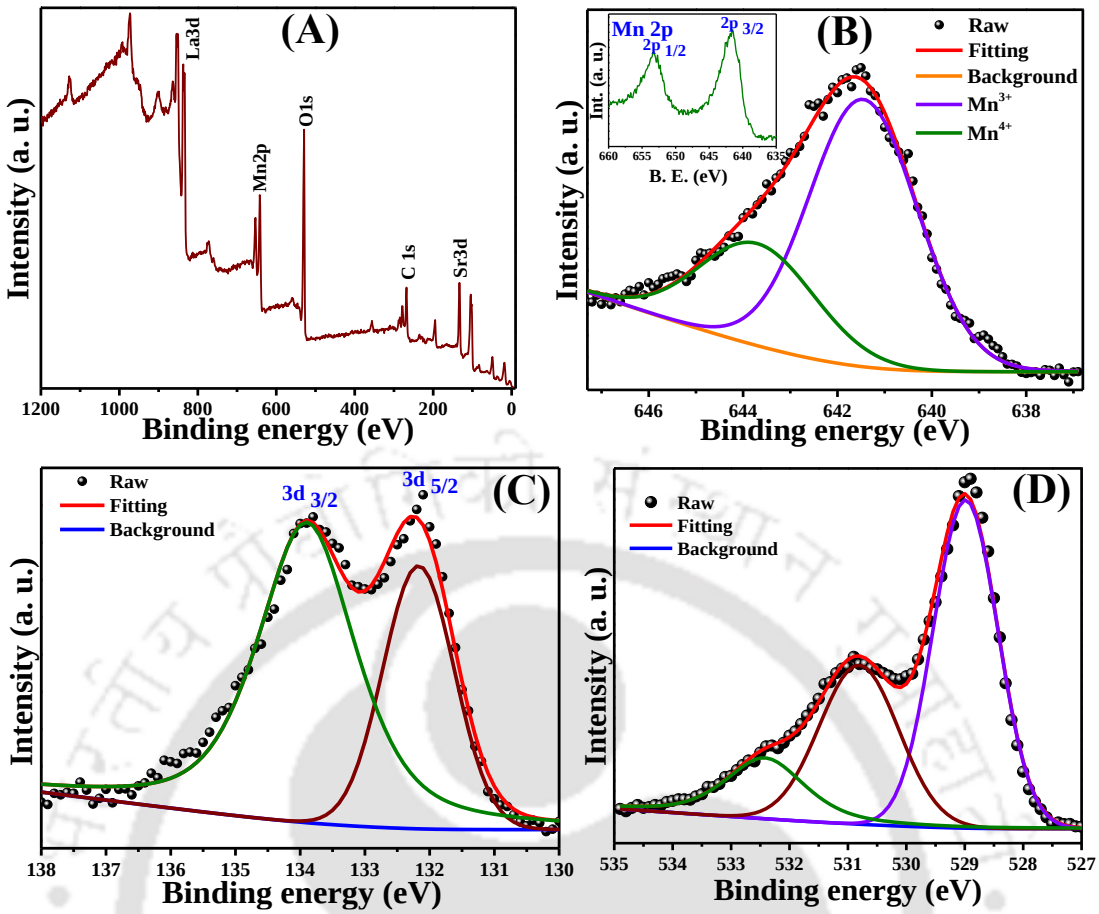

Figure 4.4 (A) XPS survey spectra, (B) deconvoluted Mn $2p_{3/2}$ peak, inset to (B) is the Mn 2p XPS core level spectra, (C) deconvoluted Sr 3d core level spectra, and (D) deconvoluted O 1s core level spectra of $La_{0.7}Sr_{0.3}MnO_3$.

4.3.3 Ultraviolet–visible Diffuse Reflectance Spectra

The UV-visible diffused reflectance spectra of $La_{1-x}Sr_xMnO_3$ (x = 0.0 – 0.5) was shown in Figure **4.5**. From these spectra, it is clear that these photocatalysts don't have absorption onset in the wavelength range of 200 – 800 nm investigated in this work and absorb whole UV-visible light as well as a portion of near infra-red light. Therefore, these compounds have very small band gap like metallic materials, less than 1.5 eV (800 nm) and could act as very good photocatalyst under UV as well as visible light. Inset to Figure **4.5** shows the UV-Vis diffused reflectance spectra of $La_{1-x}Sr_xMnO_3$ (x = 0.0 – 0.5) – GO composites and we did not observe any change in the absorption profile from the as-synthesized $La_{1-x}Sr_xMnO_3$ (x = 0.0 – 0.5) compounds. From this spectra, it can be stated that GO does not alter the absorption profile of the as-synthesized $La_{1-x}Sr_xMnO_3$ (x = 0.0 – 0.5) photocatalysts.

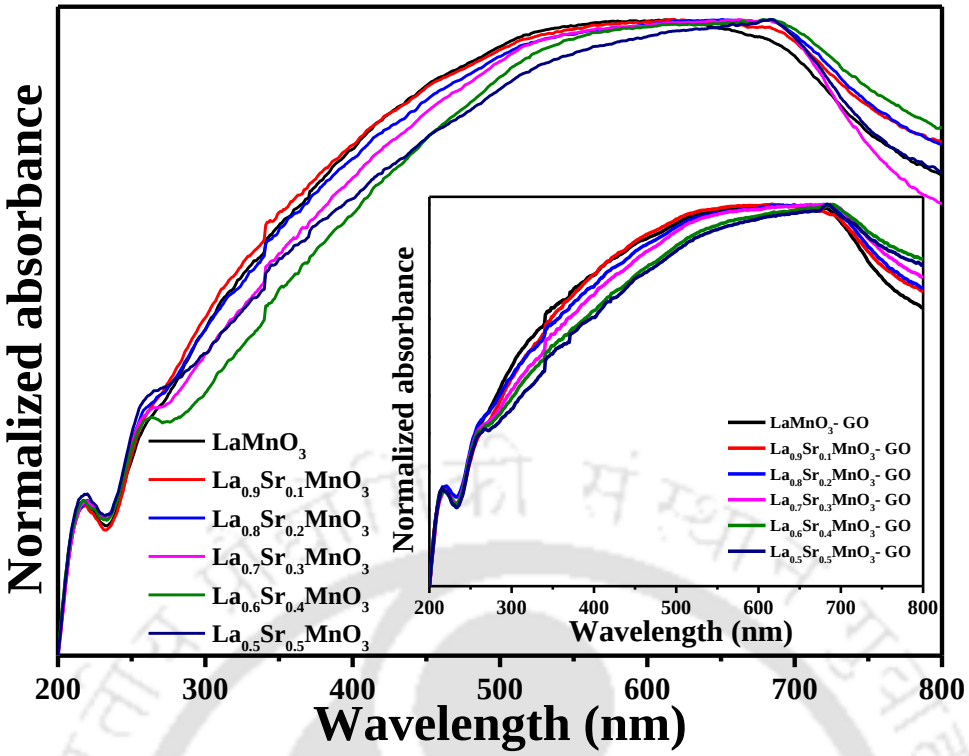

Figure 4.5 UV–visible diffuse reflectance spectra of $La_{1-x}Sr_xMnO_3$ (x = 0.0 – 0.5).

4.3.4 Field Emission Transmission Electron Microscopic (FETEM) Image and Elemental Analysis

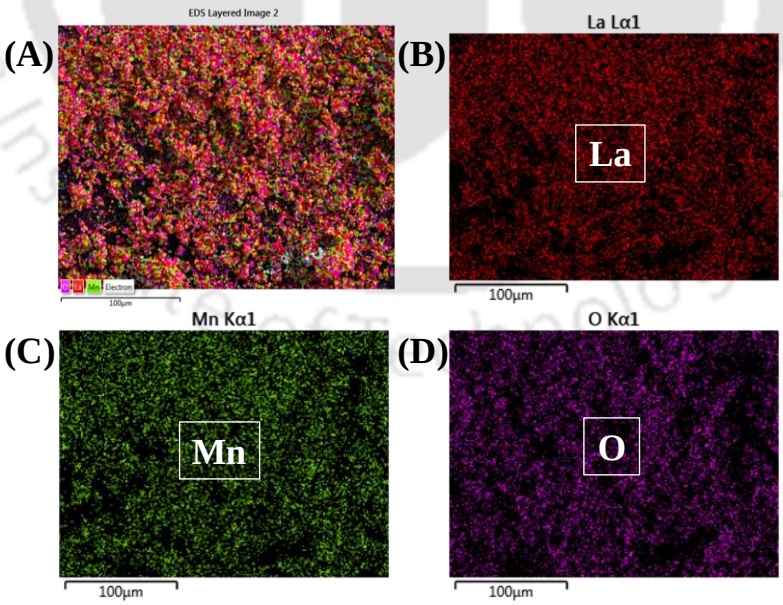

Figure 4.6 (A) EDX mapping of $LaMnO_3$, (B) elemental distribution of La, (C) Mn, and (D) O in (A).

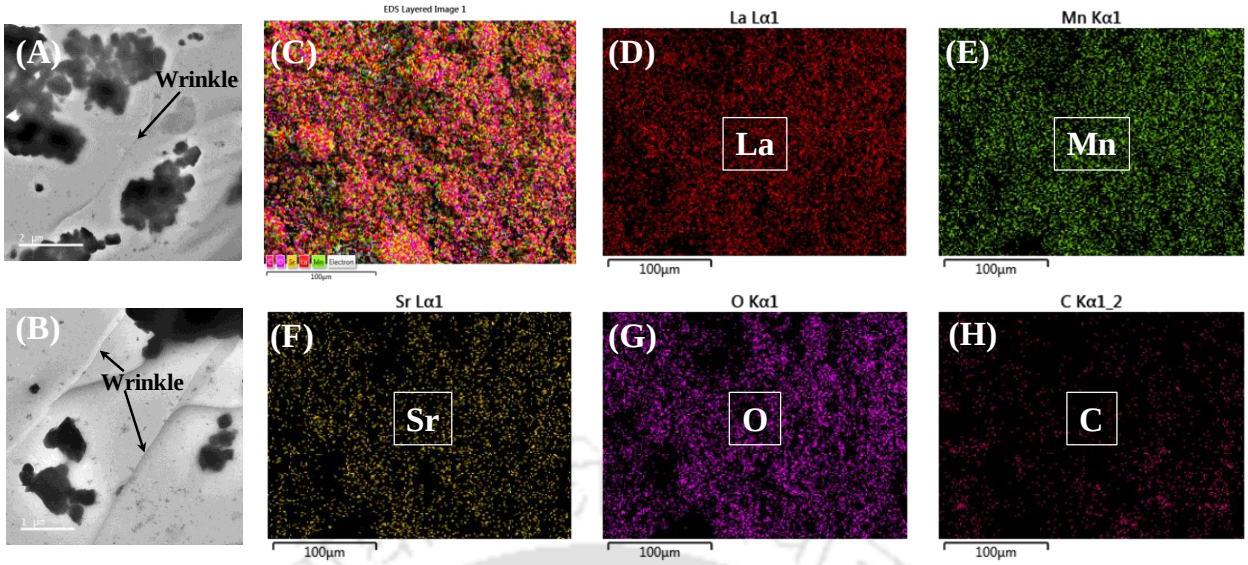

Figure 4.7 (A & B) Field Emission Transmission Electron Microscopic (FETEM) image of $La_{0.7}Sr_{0.3}MnO_3$ – GO composite, (C) EDX mapping of $La_{0.7}Sr_{0.3}MnO_3$ – GO composite (D) elemental distribution of La, (E) Mn, (F) Sr, (G) O and (H) O in (C).

To check the homogeneous elemental distribution in compounds, energy-dispersive X-ray (EDX) spectroscopic mapping was carried out. Figure **4.6(A)** shows the elemental distribution of the parent compound $LaMnO_3$ and Figure **4.6(B – D)** show the distribution of La, Mn, and O, respectively in the Figure **4.6(A)** scan area. It is observed that all the elements are evenly distributed throughout the sample. Figure **4.7(C)** shows the elemental distribution of the best performing compound $La_{0.7}Sr_{0.3}MnO_3$ – GO and Figure **4.7(D – H)** show the distribution of La, Mn, O, Sr and C respectively in the Figure **4.7B** scan area. It is observed that all the elements are evenly distributed throughout the sample. Figure **4.7(A – B)** represent the field emission transmission electron microscopic (FETEM) image of $La_{0.7}Sr_{0.3}MnO_3$ – GO composite and from these images the characteristic wrinkle of GO is clearly seen which proves the presence of GO sheet in $La_{0.7}Sr_{0.3}MnO_3$ – GO.

4.3.5 Room Temperature Resistivity Measurement

Since the catalyst acts as a sink or source of electrons in catalyzed redox reactions, for the optimum performance, suitable conductivity within the catalyst is important. Four probe resistivity measurements for the as-synthesized $La_{1-x}Sr_xMnO_3$ ($x = 0.0 – 0.5$) compounds with variable doping concentration of Sr are recorded at room temperature. From the resistivity plot shown in Figure **4.8**, it should be noted that the resistivity of $LaMnO_3$ increases initially from 0.166 Ω cm to 80 Ω cm in $La_{0.9}Sr_{0.1}MnO_3$, then decreases with an increase in Sr doping

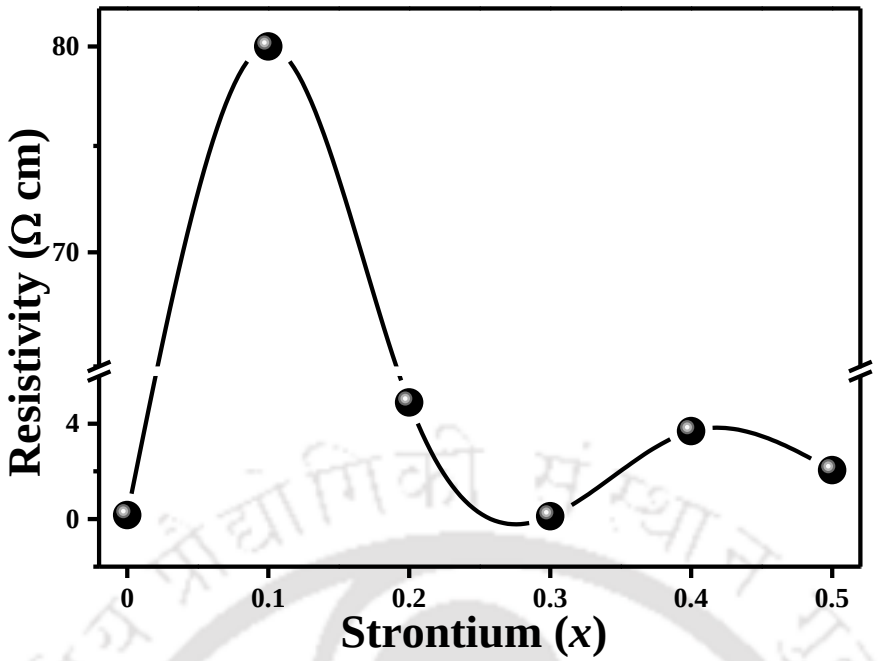

Figure 4.8 Room temperature resistivity values of $La_{1-x}Sr_xMnO_3$ photocatalyst (x = 0.0 – 0.5).

concentration from x = 0.1 to 0.3, but the trend does not hold with further increase in dopant level from x = 0.3 to 0.5. The lowest resistivity is obtained for x = 0.3. The low resistivity in $LaMnO_3$ may be due to presence of oxygen over stoichiometry. Decrease in resistivity from 80 Ω cm to 0.118 Ω cm can be correlated to the progressive increase in oxidation state of Mn from (III) to (IV) in $La_{1-x}Sr_xMnO_3$ compounds due to Sr doping.[37] The decrease in resistivity of $La_{1-x}Sr_xMnO_3$ (x = 0.0 – 0.5) occurs due to the more conductive nature of Mn (IV) as compared to Mn (III) and due to the existence of double exchange mechanism between two Mn (III) and Mn (IV) via O_2^{2-} ions. [38] A similar kind of resistivity trend has been reported by Nagabhushana et al.[39]

4.3.6 Photocatalytic Water Oxidation

For efficient hydrogen and oxygen generation from water, the bottom level of the conduction band of the photocatalysts has to be more negative than the redox potential of H^+/H_2 (0 V vs. NHE, pH = 0) while the top level of the valence band has to be more positive than the redox potential of O_2/H_2O (1.23 V vs. NHE, pH = 0).[40] So, the theoretical minimum band gap for water splitting is 1.23 eV. It is well known that the valence band of lanthanum manganites mainly consists of O 2p orbital contribution whereas the conduction band mainly consists of Mn 3d orbital contribution.[41] It is interesting to note that the valence band is lying well below the oxidation potential of H_2O/O_2 which facilitates oxygen production preferentially.

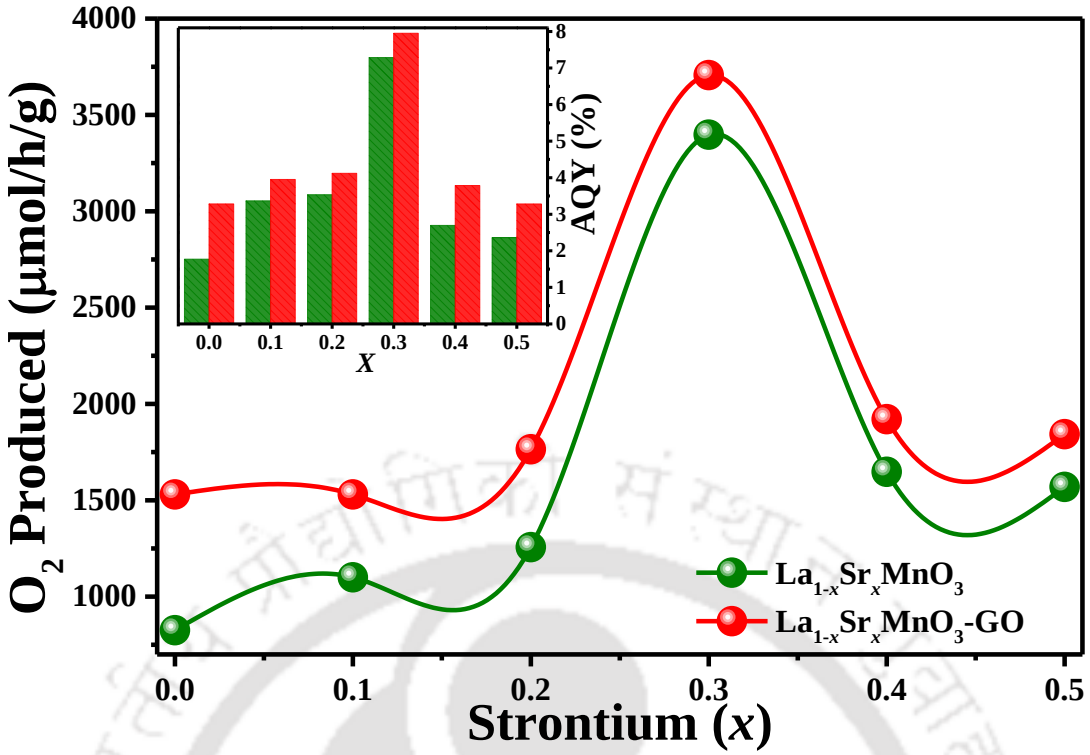

Figure 4.9 Photocatalytic O_2 production from water oxidation by $La_{1-x}Sr_xMnO_3$ (x = 0.0 – 0.5) and $La_{1-x}Sr_xMnO_3$ (x = 0.0 – 0.5) – GO photocatalysts and inset shows the calculated AQY values.

Migration of holes to the surface reaction site of the photocatalyst depends on the transport phenomenon of the system. The transport properties of the doped perovskites are strongly dependent on the Mn–O–Mn alignment, wherein the bond angle should ideally be 180° for enhanced conductivity. Progressive doping of strontium into the lanthanum manganite causes the bond angle to change from 150° (x = 0.0) to 180° (x = 0.3) due to the internal chemical pressure; which allows maximum electron conductance in the system. With further doping of strontium; i.e. x > 0.3, the bond angle moves towards 150° causing the hindrance to the migration of electron/ holes in the system. The four probe resistivity values of the lanthanum manganites showing a minimum resistivity of 0.118 Ω cm for x = 0.3 strontium doping. Doping of strontium in the lanthanum site facilitates the formation of an equivalent amount of holes (Mn (IV)) inducing the conduction pathway, which helps the formed charges to migrate to the surface of the reaction site to oxidize water. The cumulative effect of maximum conductance and hole formation leads to the enhanced photocatalytic oxygen generation in $La_{0.7}Sr_{0.3}MnO_3$. From the photoelectron spectroscopic measurements, the energy level of O 2p lies 6 eV below the Fermi level, which is equivalent to 1.56 eV vs NHE, whereas the Mn 3d level lies around 4.5 eV below the Fermi level.[41] With increase in the concentration of

strontium, the bond angle between Mn–O–Mn reaches to optimum 180° to facilitate the conduction of holes to the surface through the oxygen orbital of the valence band.

Figure **4.9** shows the photocatalytic oxygen production and calculated AQY values of $La_{1-x}Sr_xMnO_3$ (x = 0.0 – 0.5) and $La_{1-x}Sr_xMnO_3$ (x = 0.0 – 0.5) – GO photocatalysts. We have found that $La_{0.7}Sr_{0.3}MnO_3$ is the best performing photocatalyst and produce oxygen at a rate of 3.398 mmol/h/g (AQY ~ 7.2%) in comparison to $LaMnO_3$ (0.826 mmol/h/g, AQY ~ 1.8%), $La_{0.9}Sr_{0.1}MnO_3$ (1.100 mmol/h/g, AQY ~ 2.4%), $La_{0.8}Sr_{0.2}MnO_3$ (1.257 mmol/h/g, AQY ~ 2.7%), $La_{0.6}Sr_{0.4}MnO_3$ (1.648 mmol/h/g, AQY ~ 3.5%) and $La_{0.5}Sr_{0.5}MnO_3$ (1.570 mmol/h/g, AQY ~ 3.4%) . Additionally, introduction of GO into the system enhances the charge separation due to the ability of GO to readily accept the electrons thereby separating the electrons and holes efficiently and hence increases photocatalytic oxygen production. $La_{0.7}Sr_{0.3}MnO_3$ – GO shows highest photocatalytic activity in oxygen production at a rate of 3.707 mmol/h/g (AQY ~ 8%) in comparison to $LaMnO_3$ – GO (1.530 mmol/h/g, AQY ~ 3.3%), $La_{0.9}Sr_{0.1}MnO_3$ – GO (1.530 mmol/h/g, AQY ~ 3.3%), $La_{0.8}Sr_{0.2}MnO_3$ – GO (1.765 mmol/h/g, AQY ~ 3.8%), $La_{0.6}Sr_{0.4}MnO_3$ – GO (1.921 mmol/h/g, AQY ~ 4.1%) and $La_{0.5}Sr_{0.5}MnO_3$ – GO (1.843 mmol/h/g, AQY ~ 4%).

4.4 CONCLUSIONS

In summary, this work reports the synthesis of stable and robust $La_{1-x}Sr_xMnO_3$ (x = 0.0 – 0.5) and $La_{1-x}Sr_xMnO_3$ (x = 0.0 – 0.5) – GO composite and its use as a photocatalyst for water oxidation. Sr doping in LMO creates holes or Mn (IV) in $La_{1-x}Sr_xMnO_3$ (x = 0.0 – 0.5) lattice. Owing to doping of larger Sr ions in La site, the crystal phase of $La_{1-x}Sr_xMnO_3$ (x = 0.0 – 0.5) changes from rhombohedral to cubic in higher Sr doping concentration and thereby makes the Mn–O–Mn angle ~180° in doped compounds. Formation of holes or Mn (IV) and ~180° of Mn–O–Mn bond angle facilitates the charge transport in these compounds. As $La_{0.7}Sr_{0.3}MnO_3$ photocatalyst has lowest resistivity among all $La_{1-x}Sr_xMnO_3$ (x = 0.0 – 0.5) photocatalysts, it gives highest amount of O_2 evolution from water oxidation (3.398 mmol/h/g, AQY ~ 7.2%). A blending of GO with $La_{1-x}Sr_xMnO_3$ (x = 0.0 – 0.5) shows further enhancement in photocatalytic O_2 evolution from water due to the good charge carrier transport property of GO and $La_{0.7}Sr_{0.3}MnO_3$ – GO shows highest photocatalytic activity in oxygen production at a rate of 3.707 mmol/h/g with ~ 8% of AQY.

4.5 REFERENCES

1. Co, A. C.; Birss, V. I. *J. Phys. Chem. B* **2006**, *110*, 11299.
2. Nicastro, M.; Patterson, C. H. *Phys. Rev. B* **2002**, *65,* 205111.
3. Gor'kov, L. V.; Kresin, V. Z. *Phys. Rep.* **2004**, *400*, 149.
4. Rao, C. N. R. *J. Phys. Chem. B* **2000**, *104*, 5877.
5. Jin, S.; Tiefel, T. H.; Cormack, M. M.; Fastnacht, R. A.; Ramesh, R.; Chen, L. H. *Science* **1994**, *264*, 413.
6. Tian, Y.; Chen, D. R.; Jiao, X. L. *Chem. Mater.* **2006**, *18*, 6088.
7. Haile, S. M.; *Acta Mater.* **2003**, *51*, 5981.
8. Maity, S.; Ray, S. K.; Bhattacharya, D. *J. Phys. Chem. Solids* **2013**, *74*, 315.
9. Mori, M.; N. Sammes, M.; Suda, E.; Takeda, Y.; *Solid State Ionics* **2003**, *164*, 1.
10. Wang, X. W.; Zhu, Q. Q.; Wang, X. E.; Zhang, H. C.; Zhang, J. J.; Wang, L. F. *J. Alloys Compd.* **2016**, *675*, 195.
11. Stankovich, S.; Dikin, D. A.; Dommett, G. H. B.; Kohlhaas, K. M.; Zimney, E. J.; Stach, E. A.; Piner, R. D.; Nguyen, S. B. T.; Ruoff, R. S. *Nature* **2006**, *442*, 282.
12. Mathkar, A.; Tozier, D.; Cox, P.; Ong, P.; Galande, C.; Balakrishnan, K.; Reddy, A. L. M.; Ajayan, P. M. *J. Phys. Chem. Lett.* **2012**, *3*, 986.
13. Zhu, Y. W.; Murali, S.; Cai, W. W.; Li, X. S.; Suk, J. W.; Potts, J. R.; Ruoff, R. S. *Adv. Mater.* **2010**, *22*, 3906.
14. Kamat, P. V. *J. Phys. Chem. Lett.* **2011**, *2*, 242.
15. Dreyer, D. R.; Park, S.; Bielawski, C. W.; Ruoff, R. S. *Chem. Soc.Rev.* **2010**, *39*, 228.
16. Geim, A. K. *Science* **2009**, *324*, 1530.
17. Yeh, T. F.; Syu, J. M.; Cheng, C.; Chang, T. H.; Teng, H. *Adv. Funct. Mater.* **2010**, *20*, 2255.
18. Zhuo, S. J.; Shao, M. W.; Lee, S. T. *ACS Nano* **2012**, *6*, 1059.
19. Eda, G.; Mattevi, C.; Yamaguchi, H.; Kim, H.; Chhowalla, M. *J. Phys. Chem. C* **2009**, *113*, 15768.
20. Eda, G.; Chhowalla, M. *Adv. Mater.* **2010**, *22*, 2392.
21. Hou, J.; Wang, Z.; Kan, W.; Jiao, S.; Zhu, H.; Kumar, R. V. *J. Mater. Chem.* **2012**, *22*, 7291.
22. Yeh, T. F.; Cihlář, J.; Chang, C. Y.; Cheng, C.; Teng, H. *Mater. Today* **2013**, *16*, 78.
23. Gao, P.; Liu, J.; Lee, S.; Zhang, T.; Sun, D. D. *J. Mater. Chem.* **2012**, *22*, 2292.
24. Ng, Y. H.; Iwase, A.; Kudo, A.; Amal, R. *J. Phys. Chem. Lett.* **2010**, *1*, 2607.
25. Chen, C.; Cai, W.; Long, M.; Zhou, B.; Wu, Y.; Wu, D.; Feng, Y. *ACS Nano* **2010**, *4*, 6425.
26. Hummers, W. S.; Offeman, R. E. *J. Am. Chem. Soc.* **1958**, *80*, 1339.
27. Fu, Min.; Jiao, Q.; Zhao, Y.; Li, H. *J. Mater. Chem. A* **2014**, *2*, 735.
28. Kuznetsov, M. V; Parkin, I. P.; Caruana, D. J.; Morozov, Y. G. *J. Mater. Chem.* **2004**, *14*, 1377.

29. Alonso, J. A.; Martínez-lope, M. J.; Casais, M. T.; Macmanus-driscoll, J. L.; de Silva, P. S. I. P. N.; Cohen, L. F.; Fernández-díaz, M. T. *J. Mater. Chem.* **1997**, *7*, 2139.
30. Maurin, I.; Barboux, P.; Lassailly, Y.; Boilot, J. P.; Villain, F.; Dordor, P. *J. Solid State Chem.* **2001**, *160*, 123.
31. Tian, Y.; Chen, D.; Jiao, X. *Chem. Mater.* **2006**, *18*, 6088.
32. Daengsakul, S.; Thomas, C.; Thomas, I.; Mongkolkachit, C.; Siri, S.; Amornkitbamrung, V.; Maensiri, S. *Nanoscale Res. Lett.* **2009**, *4*, 839.
33. Rørmark, L.; Wiik, K.; Stølen, S.; Grande, T. *J. Mater. Chem.* **2002**, *12*, 1058.
34. Wang, L. M.; Lai, J. -H.; Wu, J. -I.; Kuo, Y. -K.; Chang, C. L. *J. Appl. Phys.* **2007**, *102*, 023915.
35. Zhou, W.; Sunarso, J. *J. Phys. Chem. Lett.* **2013**, *4*, 2982.
36. Giri, A.; Goswami, N.; Bootharaju, M. S.; Xavier, P. L.; John, R.; Thanh, N. T. K.; Pradeep, T.; Ghosh, B.; Raychaudhuri, A. K.; Pal, S. K. *J. Phys. Chem. C* **2012**, *116*, 25623.
37. Banach, G.; Temmerman, W. M. *Phys. Rev. B* **2004**, *69*, 054427.
38. Chang-Sun, P.; Ho-Jung, S. *J. Korean Phys. Soc.* **2010**, *57*, 994.
39. Nagabhushana, B. M.; Chakradhar, R. P. S.; Ramesh, K. P.; Shivakumara, C.; Chandrappa, G. T. *Mater. Res. Bull.* **2006**, *41*, 1735-1741.
40. Iwase, A.; Kato, H.; Kudo, A. *ChemSusChem* **2009**, *2*, 873.
41. Santoni, A.; Speranza, G.; Mancini, M. R.; Padella, F.; Petrucci, L.; Casadio, S. *J. Phys. Condense Mater.* **1999**, *11*, 3387.

Chapter 5

Synergistic Effect of Cerium Doping and Oxygen Vacancies in Photocatalytic Hydrogen Production Efficiency of $BaZrO_{3-\delta}$ Hollow Nanospheres

This Chapter illustrates the synergistic effect of oxygen vacancies and cerium doping in photocatalytic water reduction of a template free hydrothermally synthesized of B site Ce doped barium zirconate hollow nanospheres, $BaZr_{1-x}Ce_xO_{3-\delta}$ (x = 0.00 – 0.04). Lattice disorder, oxygen vacancies and substituting Zr ions by Ce ions alter the electronic structure of $BaZrO_{3-\delta}$ compounds, resulting in their increase in photocatalytic efficiencies. Photocatalytic efficiencies of $BaZr_{1-x}Ce_xO_{3-\delta}$ (x = 0.00 – 0.04) compounds further increased by reducing lattice disorder and oxygen vacancies – which act as charge carrier trap states, by calcining at ambient atmosphere.

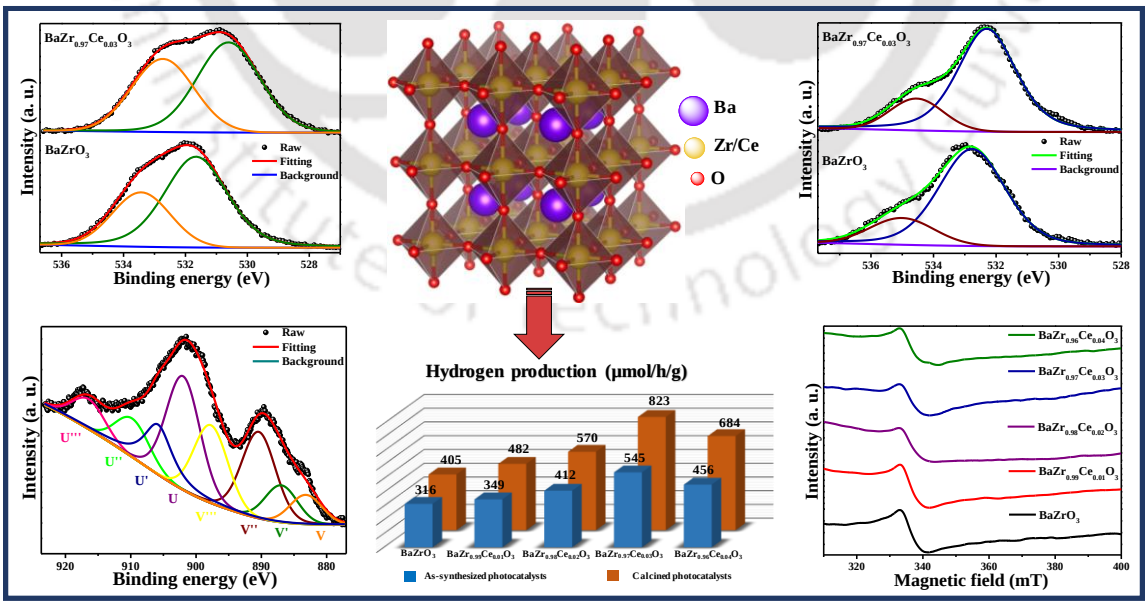

Manuscript under communication

5.1 INTRODUCTION

Among several studied perovskite oxide photocatalysts, barium zirconate, $BaZrO_3$ (BZO), a typical wide band gap cubic perovskite oxide, is a promising material with a wide range of technological applications in modern industries.[1 – 3] BZO has been studied extensively due to its high conductivity and ability to host wide range of dopants into it. In recent times, Yuan *et al.* have reported BZO as an efficient photocatalyst for photocatalytic hydrogen production from water without the assistance of any cocatalysts.[4] In order to enhance the visible-light absorption of such wide band gap materials, several attempts have been made to modify their band positions by incorporating metal or anion dopants and creating oxygen vacancies into the lattice.[5] Surface oxygen vacancies act as trap states for photo-induced charge carriers, reducing the probability of electron-hole recombination, whereas, bulk oxygen vacancies act as photogenerated charge recombination centers and thus play a crucial role in photocatalysis.[6, 7] Moreover, trap states induce mid-gap energy levels in the material and thereby allow fine tuning of the electronic structure.[8]

Efficient utilization of incident sunlight by the semiconductor could be one effective way to enhance the catalytic activity of a photocatalyst material. Literature reports have shown that structures with suitable inner voids can contribute to the incident light absorption by multiple reflections and scattering inside the voids.[9] For example, in case of TiO_2, a hollow–sphere morphology is known to exhibit a superior photocatalytic effect compared to its dense counterpart.[10] Thus, morphological modification to generate hollow nanospheres can contribute to enhanced light absorption.

To enhance the photocatalytic activity of BZO material a number of attempts have been made in past few years, such as, Zou *et al.* have reported that Sn(IV) doped BZO shows enhanced photocatalytic hydrogen production because of the reduction in band gap energy through altering the density of states in the vicinity of the conduction band, which changes the charge-carrier excitation process in BZO.[11] Similarly, Díaz-Torres *et al.* have reported enhanced photocatalytic activity from Bi-doped BZO due to the shift in absorption onset toward the visible light.[12] Furthermore, lanthanide elements can be used as electron acceptor dopants in wide band gap semiconductors, which results in a shift in the absorption onset toward the visible spectral region.[13] Among the lanthanide elements, cerium is one of the most favorable choices due to its low cost and formation of a stable Ce(III)/Ce(IV) redox couple in oxidizing and reducing conditions. It is reported that the Ce(III)/Ce(IV) couple whose different electronic configurations of $4f^1 5d^0/4f^0 5d^0$ can introduce diverse optical properties and

improve electron-hole pair separation in doped photocatalysts.[14] Additionally, this combination of ions result in increased oxygen vacancies in compounds which could be beneficial for the photocatalytic efficiency of a material.[15] These advantages motivated us to synthesize hollow nanospheres of $BaZr_{1-x}Ce_xO_3$, where x = 0.00 – 0.04 and "x" denotes the partial degree of Ce substitution, to gain an understanding on the effect of Ce on the crystal structure and optical and photocatalytic properties of BZO.

5.2 EXPERIMENTAL SECTION

5.2.1 Preparation of $BaZr_{1-x}Ce_xO_3$ (x = 0.00 – 0.04)

Cerium doped barium zirconate compounds were prepared following a modified hydrothermal method.[16] The reactions were carried out in a stainless-steel autoclave with Teflon liner at 200 °C and autogenous pressure. Briefly, a stoichiometric amount of $BaCl_2 \cdot 2H_2O$, $ZrOCl_2 \cdot 8H_2O$ and $(NH_4)_2Ce(NO_3)_6$ were weighed according to the stoichiometry of $BaZr_{1-x}Ce_xO_3$ (x = 0.00 – 0.04) and transferred to a Teflon made autoclave reactor. A 20 M aqueous KOH solution was prepared in a round bottomed flask by dissolving a calculated amount of KOH pellets into milli-Q water. To avoid any inhomogeneous mixing of the reagents, the as-prepared KOH solution was added to the previously taken metal salts and filled the reactor up to 70% of its volume and vigorously stirred for 1 h. Thereafter, these Teflon beakers were sealed inside a stainless steel jacket and kept in a pre-heated electric oven for 24 h at 200 °C. After completion of the reaction, autoclaves were allowed to cool to room temperature. The white precipitate was centrifuged and washed with water, dilute acetic acid and ethanol several times to remove the impurities. Finally, the obtained purified products were dried at 100 °C overnight.

5.3 RESULTS AND DISCUSSION

5.3.1 Powder X-ray Diffraction (PXRD) Patterns

Phase purity and crystal structure of the as-synthesized materials were determined by PXRD. Well-indexed PXRD patterns in the 2θ range of 20° – 80° for $BaZr_{1-x}Ce_xO_3$ (x = 0.00 – 0.04) photocatalysts are shown in Figure **5.1(A)**. From the diffractogram patterns it is verified that all the compounds belong to the cubic phase with $Pm\bar{3}m$ space group (no. 221) [JCPDS file No.06-0399]. The PXRD patterns of the parent compound BZO and Ce doped BZO are free from any discernable impurity peaks or peaks for CeO_2 (2θ = 28.5°, 47.7°, 56.6°), which were not observed in the Ce-doped BZO compositions and supports the successful doping of Ce in

BZO. Figure **5.1(B)** shows a gradual shifting of (110) diffraction peaks toward lower values in the 2θ range of 29.6° – 30.6°. This can be explained based on the ionic radii of Ce(III) / Ce(IV) (101 pm/87 pm), which are larger than that of Zr(IV) (72 pm) in an octahedral environment. Hence, doping of Ce at Zr sites expands the unit cell volume and shifts the 2θ value in the PXRD patterns toward lower values.

In order to understand the effect of Ce doping on the crystal structure, lattice parameters, and unit cell volume, we performed Rietveld refinement of the PXRD diffraction patterns of $BaZr_{1-x}Ce_xO_3$ (x = 0.00 – 0.04) compounds. In the cubic BZO and Ce-doped BZO perovskite structures, the Ba atoms are in the Wyckoff position 1b (0.5, 0.5, 0.5), Zr/Ce in 1a (0, 0, 0) and O in 3d (0.5, 0, 0). Figure **5.2(A – E)** shows the Rietveld refined PXRD pattern of $BaZr_{1-x}Ce_xO_3$ (x = 0.00 – 0.04) catalysts. These data indicate that the compounds crystallize in cubic phase and with an increase in Ce doping in BZO, the cell parameters and unit cell volume increase linearly. Figure **5.2(F)** displays the variation of lattice parameters and cell volume with Ce doping concentration in BZO. As we have mentioned earlier that due to the size difference between cerium and zirconium, the unit cell volume of doped compounds increases compared to the parent BZO.

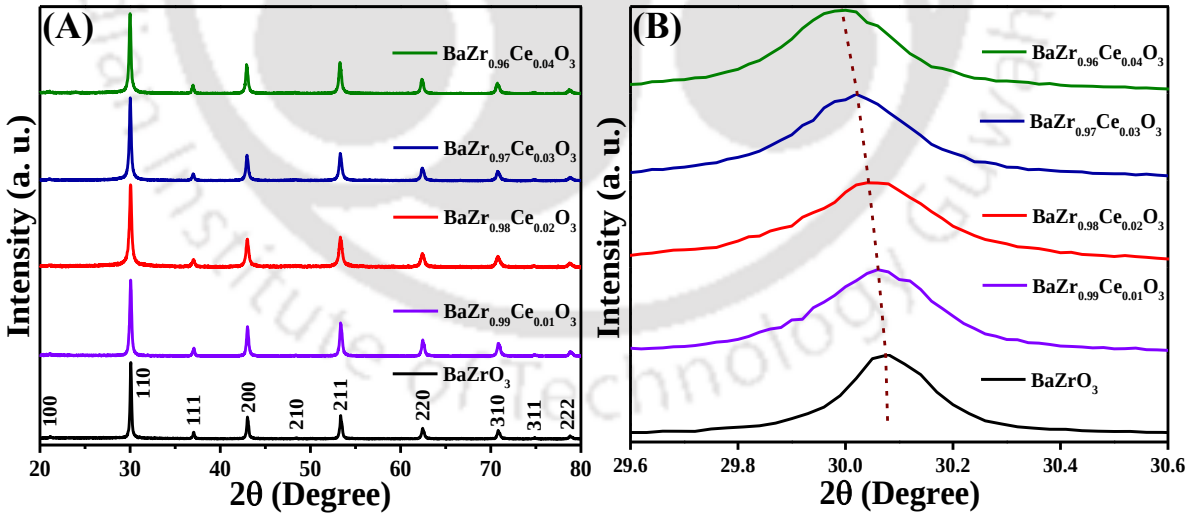

Figure 5.1 Powder X-ray diffraction patterns of $BaZr_{1-x}Ce_xO_3$ (x = 0.00 – 0.04). (A) Full scale, (B) enlarged within 2θ = 29.6° – 30.6°.

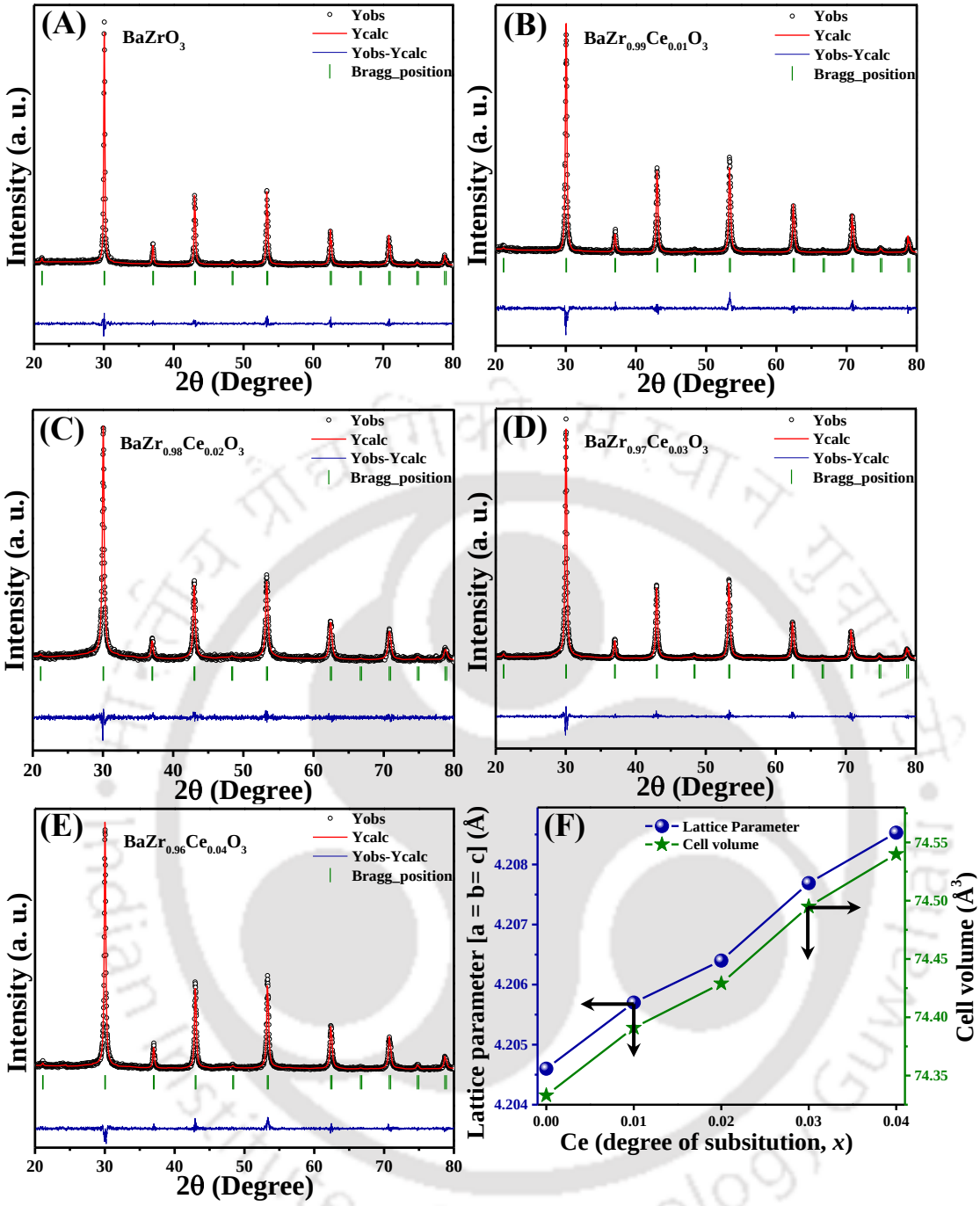

Figure 5.2 Rietveld refined PXRD profile of the as-synthesized (A – E) $BaZrO_3$, $BaZr_{0.99}Ce_{0.01}O_3$, $BaZr_{0.98}Ce_{0.02}O_3$, $BaZr_{0.97}Ce_{0.03}O_3$ and $BaZr_{0.96}Ce_{0.04}O_3$. Blue line in the bottom shows the difference between observed and calculated values and vertical sticks in olive color denote calculated Bragg positions for cubic phases in the Rietveld refined plot. (F) Variation of lattice parameters and cell volume with Ce doping concentration in BZO.

Table 5.1 Structural parameters obtained by Rietveld refinement of the powder X-ray diffraction data of $BaZr_{1-x}Ce_xO_3$ (x = 0.00 – 0.04) catalysts.

$BaZr_{1-x}Ce_xO_3$	***x* = 0.00**	***x* = 0.01**	***x* = 0.02**	***x* = 0.03**	***x* = 0.04**
Crystal system	cubic	cubic	cubic	cubic	cubic
Space group	$Pm\bar{3}m$	$Pm\bar{3}m$	$Pm\bar{3}m$	$Pm\bar{3}m$	$Pm\bar{3}m$
a, Å	4.2046	4.2057	4.2064	4.20769	4.20853
b, Å	4.2046	4.2057	4.2064	4.20769	4.20853
c, Å	4.2046	4.2057	4.2064	4.20769	4.20853
Cell volume, ($Å^3$)	74.333	74.391	74.429	74.495	74.540
Atomic positions					
Ba					
x	0.5000	0.5000	0.5000	0.5000	0.5000
y	0.5000	0.5000	0.5000	0.5000	0.5000
z	0.5000	0.5000	0.5000	0.5000	0.5000
Zr/Ce					
x	0.0000	0.0000	0.0000	0.0000	0.0000
y	0.0000	0.0000	0.0000	0.0000	0.0000
z	0.0000	0.0000	0.0000	0.0000	0.0000
O					
x	0.5000	0.5000	0.5000	0.5000	0.5000
y	0.0000	0.0000	0.0000	0.0000	0.0000
z	0.0000	0.0000	0.0000	0.0000	0.0000
Rwp	21.6	17.1	20.3	16.0	20.2
Rp	22.1	16.5	23.5	14.3	18.8
R_{exp}	12.66	8.62	12.68	9.22	10.43
χ^2	2.91	3.92	2.56	3.0	3.74

Hence, from Figure **5.2(F)** it is proved that we have successfully prepared Ce doped BZO samples with different atom% of Ce. In Table **5.1**, the comprehensive values of the refined lattice parameters, unit cell volume, goodness of fit (χ^2), R_p, R_{wp}, R_{exp} and atomic positions of Ba, Zr/Ce and O of $BaZr_{1-x}Ce_xO_3$ (x = 0.00 – 0.04) are tabulated.

5.3.2 Material Morphology and Elemental Analysis

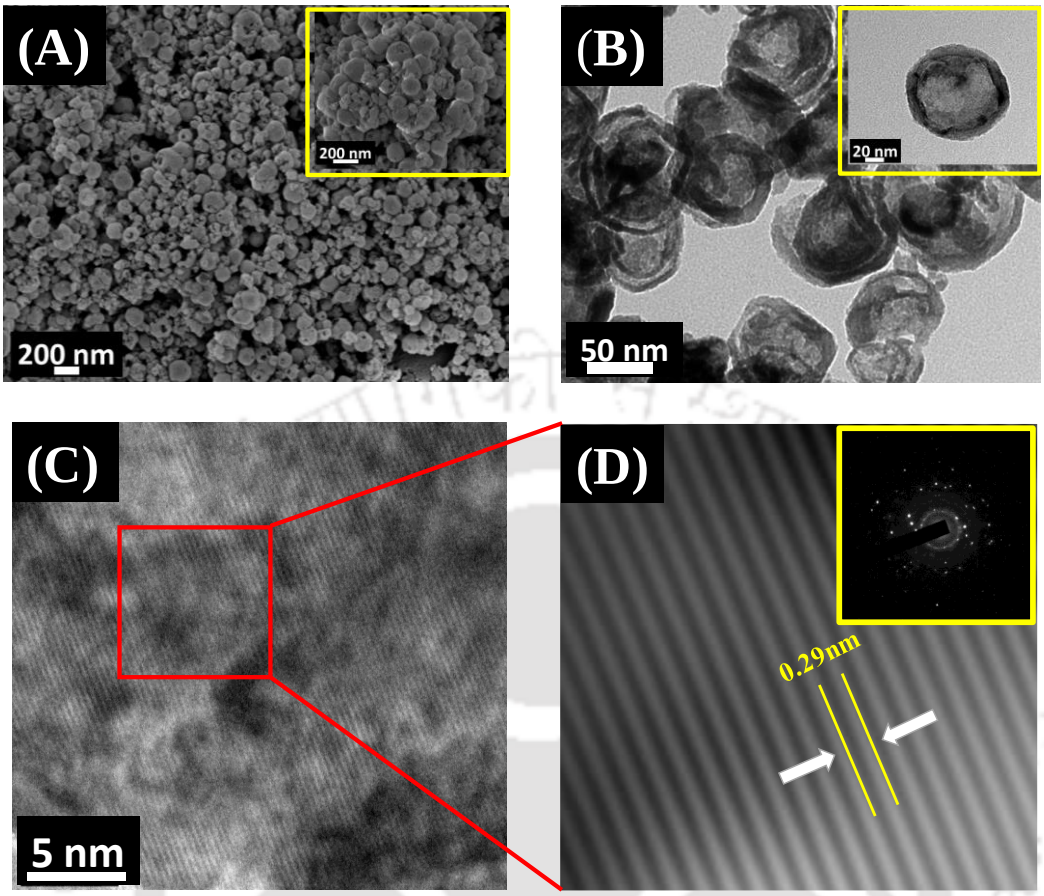

Figure 5.3 (A) FESEM image of $BaZr_{0.97}Ce_{0.03}O_3$, inset to trace (A) shows higher magnified FESEM image, (B) FETEM image of $BaZr_{0.97}Ce_{0.03}O_3$, inset to trace (B) shows FETEM image of a single hollow nanosphere, (C) high-resolution TEM (HRTEM) image of $BaZr_{0.97}Ce_{0.03}O_3$ and (D) inverse fast Fourier transformed (IFFT) of the HRTEM image of $BaZr_{0.97}Ce_{0.03}O_3$. Inset to trace (D) shows the selected area energy diffraction (SAED) patterns of $BaZr_{0.97}Ce_{0.03}O_3$ hollow nanospheres.

Figure **5.3(A)** shows field emission scanning electron microscopic (FESEM) image of $BaZr_{0.97}Ce_{0.03}O_3$ hollow nanosphere. The FESEM images reveal that as-synthesized $BaZr_{0.97}Ce_{0.03}O_3$ particles are more or less spherical and a higher magnified image [inset to Figure **5.3(A)**] shows the presence of a hollow structure. Figure **5.3(B)** shows field emission transmission electron microscopic (FETEM) image of $BaZr_{0.97}Ce_{0.03}O_3$ hollow nanosphere. Particle diameters are found to be ~150 – 200 nm. The hollow nature of the particles can be evidenced from the inset of Figure **5.3(B)**, which is the FETEM image of an individual particle and shows a sharp contrast between the dark edge and the bright region. The HRTEM image of $BaZr_{0.97}Ce_{0.03}O_3$ (Figure **5.3(C)**) shows the repeated uniform lattice fringes. Figure

5.3(D) shows the IFFT of the HRTEM image where the obtained spacing of the lattice fringes (d-spacing) is ~0.29 nm and can be assigned to the (110) lattice plane of the cubic phase of $BaZr_{0.97}Ce_{0.03}O_3$ consistent with the fact that cubic BZO usually exposes its [110] facet due to that being a lower energy surface.[17] The inset to Figure **5.3(D)** shows the SAED patterns of the $BaZr_{0.97}Ce_{0.03}O_3$ hollow nanospheres. The TEM as well as FESEM images prove the hollow nature of the product.

The formation of hollow nanospheres in hydrothermal synthesis could be explained in three different steps, viz. hydrolysis of precursors, nucleation, and growth process.[18] All steps are controlled by the course of the reaction and reaction conditions. Owing to the highly alkaline synthesis conditions (pH ≈ 14), barium, zirconium and cerium salts undergo hydrolysis to form corresponding hydroxides in the reaction medium. Here, KOH acts as a mineralizer and these metal hydroxides act as monomers of the desired product. During the course of the reaction, the solubility of the salts increases and they react to form a supersaturated sol-like suspension, which favors nucleation to generate very small product particulates by suppressing the grain-growth process. It is known that the pH of the solution, the temperature of the system, and time of the reaction catalyzes the rate of nucleation.[19] Since, the nanoparticles have high surface energy, they have the tendency to form agglomerates under the influence of van der Waals forces. This growth process of BZO follows hydrolysis or decomposition of metal hydroxide monomers. This process avoids the high surface energy and proceeds until an electrostatic barrier layer is established.[17] In the course of 24 h, hollow nanospheres are created by an Ostwald ripening process. Ostwald ripening has been widely used to synthesize many hollow inorganic nanostructures by wet chemical routes.[20, 21] Ostwald ripening is a well-known physical phenomenon in the field of crystal growth and it is related to the recrystallization process in solution phase. Like in the nucleation rate, the reaction temperature and the concentration of the alkaline solution plays a vital role in this final step. In the low reaction temperature and less alkaline conditions only partially hollow or dense nanoparticles are forms as reported by Z. Dong et al.[16, 22] Here the formation of a typical spherical structure of BZO can be attributed to adsorbed hydroxyl groups on the surface of the particles under the highly alkaline condition.[23] Scheme **5.1** illustrates step-wise formation mechanism for BZO hollow nanospheres. The decomposition or dehydration pathway can be explained by the following plausible reaction mechanism -

$$[Ba^{2+}(OH)_a^-]^m + [Zr^{4+}(OH)_b^-]^n = BaZrO_3 + 3H_2O$$

$$[Ba^{2+}(OH)_a^-]^m + [Zr^{4+}(OH)_b^-]_{1-x}^n + [Ce^{4+}(OH)_c^-]_x^o = BaZr_{1-x}Ce_xO_3 + 3H_2O$$

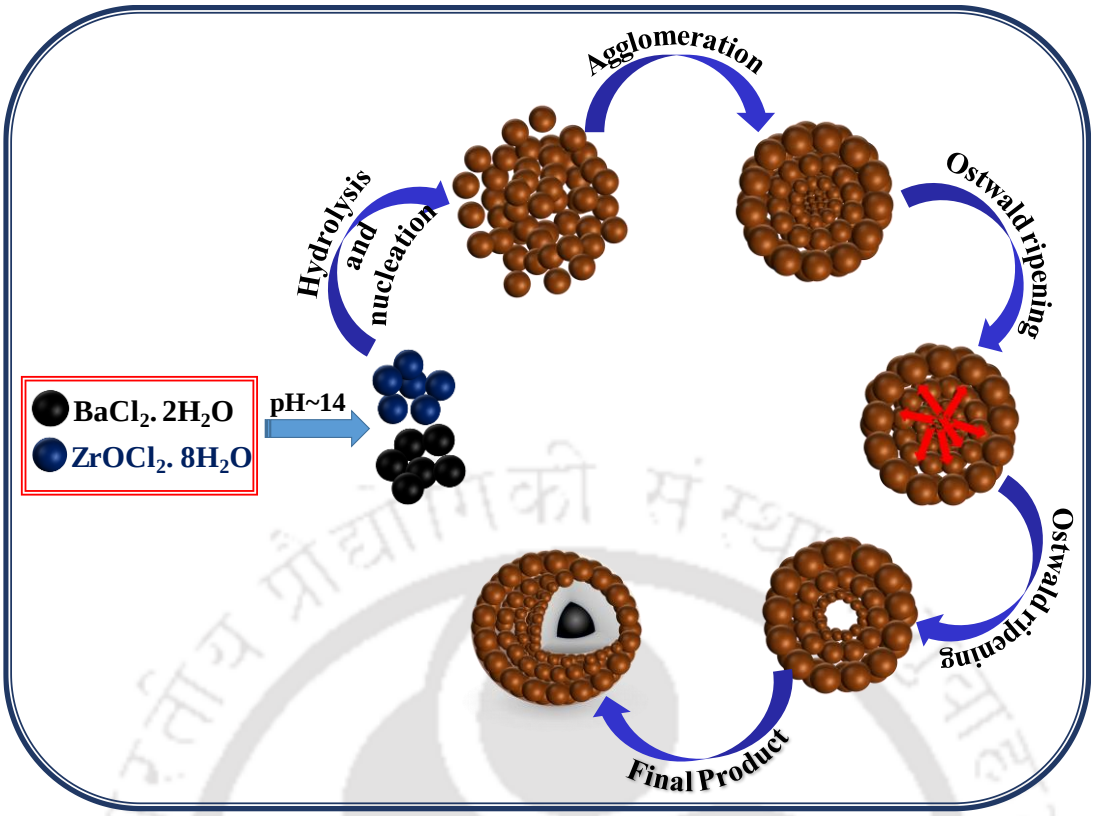

Scheme 5.1 Schematic representation of the formation of BZO hollow nanospheres in the hydrothermal process, showing stepwise formation of hollow nanospheres through hydrolysis of the constituent reagents in the presence of alkaline solution, formation of nanoparticles by nucleation, aggregation of the nanoparticles to form solid large spherical particles followed by hollow spheres through the Ostwald ripening process.

The above mentioned dehydration process is slow in a superheated and supersaturated solution and may withhold a fraction of OH^- and H_2O in BZO and form a defective crystal.[24] During the dehydration process some of the OH^- occupying the surface oxygen sites in BZO are released which leads to the formation of defective crystals with oxygen vacancies.

EDX mapping was performed to examine the elemental distribution in the synthesized compounds. Figure **5.4(A)** shows the elemental distribution of the parent compound, $BaZrO_3$ and Figure **5.4(B – D)** shows the distribution of Ba, Zr, and O, respectively in the scan area from panel A. It can be noticed that all the elements are uniformly distributed all over the sample. Figure **5.5(A)** shows the elemental distribution of the best performing catalyst, $BaZr_{0.97}Ce_{0.03}O_3$ and Figure **5.5(B – E)** shows the distribution of Ba, Zr, O and Ce, respectively in the scan area from panel A. It can be noticed that all the elements are also uniformly distributed all over the sample.

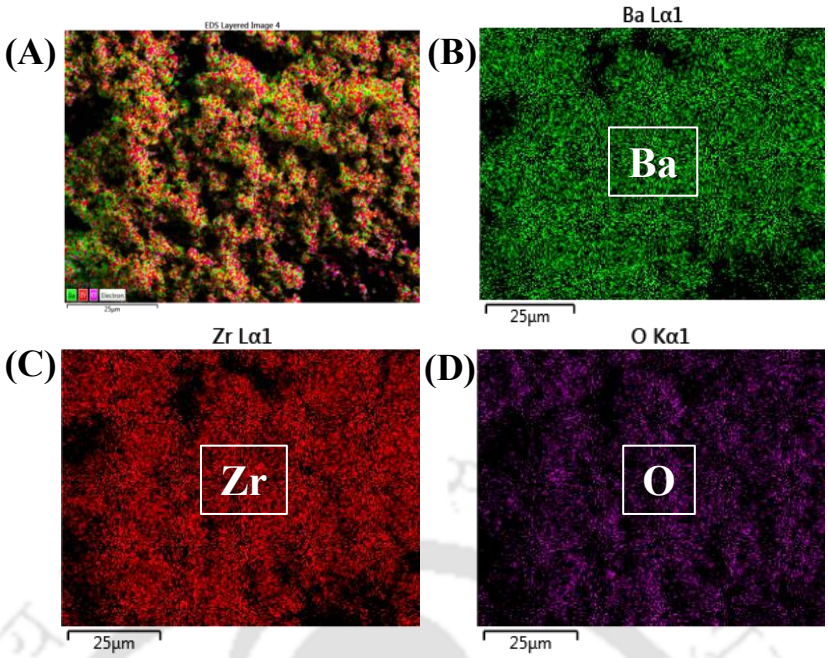

Figure 5.4 (A) EDX mapping of $BaZrO_3$, elemental distribution of (B) Ba, (C) Zr and (D) O in (A).

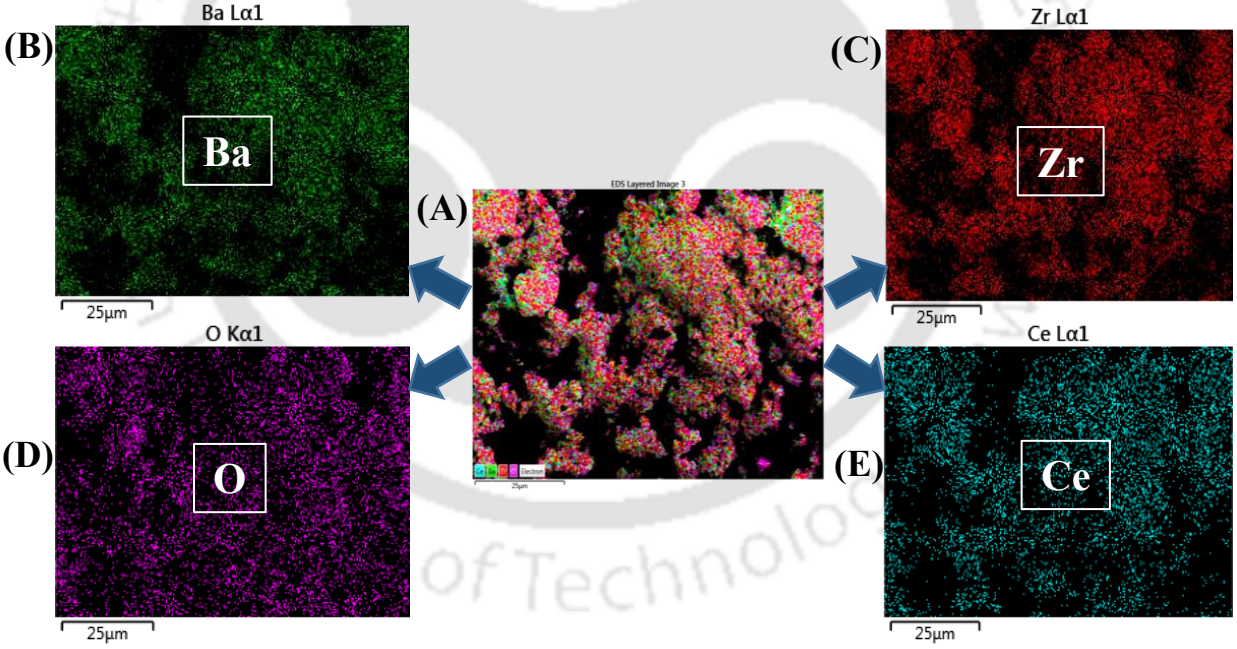

Figure 5.5 (A) EDX mapping of $BaZr_{0.97}Ce_{0.03}O_3$, elemental distribution of (B) Ba, (C) Zr, (D) O and (E) Ce in (A).

5.3.3 Ultraviolet-visible Diffuse Reflectance Spectra and Band Gap Calculation

The photocatalytic effectiveness of a material is predominantly dependent on its light absorbing capability and therefore its band gap structure. The UV–Vis DRS of the as-

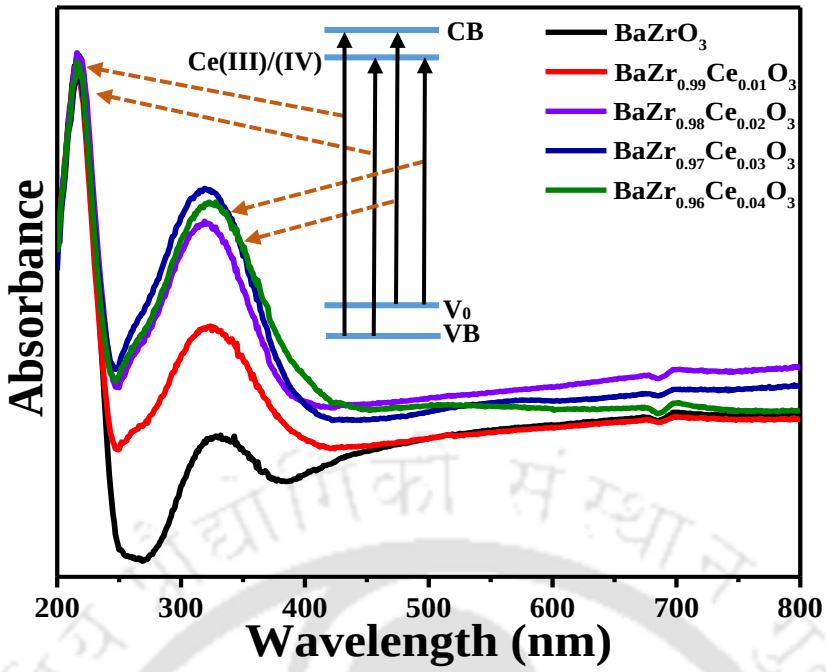

Figure 5.6 UV-visible diffuse reflectance spectra of as-synthesized $BaZr_{1-x}Ce_xO_3$ (x = 0.00 – 0.04) catalysts. The graphical image in the inset demonstrates the different phenomena responsible for the absorbance in different regions of the electromagnetic spectrum.

synthesized catalysts are shown in Figure **5.6** within the wavelength range of 200 – 800 nm. A major peak at around 230 nm is observed which can be assigned to a band-to-band transition and a band tail with an absorption extended beyond 400 nm is observed which is reasonably assigned to the presence of lattice defects, which are known to give rise to a band tail in the absorption spectrum.[25] As we have stated before, in BZO oxygen vacancies and different types of structural and electronic disorders are created due to poor oxygen atmosphere or by the removal of oxygen atoms by de-hydroxylation in BZO.[25 – 27] Different types of structural and electronic disorders are represented in Kröger-Vink notation as $[ZrO_6]^x$, $[ZrO_5.V_0^x]$, $[ZrO_5.V_0^{\bullet}]$, and $[ZrO_5.V_0^{\bullet\bullet}]$ where, $[ZrO_6]^x$ symbolizes the normal six-coordinate Zr octahedron, $[ZrO_5.V_0^x]$ denotes penta-coordinate Zr with two electrons, $[ZrO_5.V_0^{\bullet}]$ is with one unpaired electron and $[ZrO_5.V_0^{\bullet\bullet}]$ with no trapped electrons.[28] Here, $[ZrO_6]^x$ denotes normal octahedra and $[ZrO_6]'$ acts as a donor.[28]

In the Ce-doped materials, the intensity of band tail absorption peak is observed to be increased with doping percentage. With an increase in Ce doping concentration from x = 0.0 – 0.04, the absorption onset of the doped compounds are slightly red shifted. It is well known that the conduction band of BZO is predominantly formed by Zr 3d orbitals, whereas the valence band is made of O 2p orbitals.[11] The presence of oxygen vacancies and structural

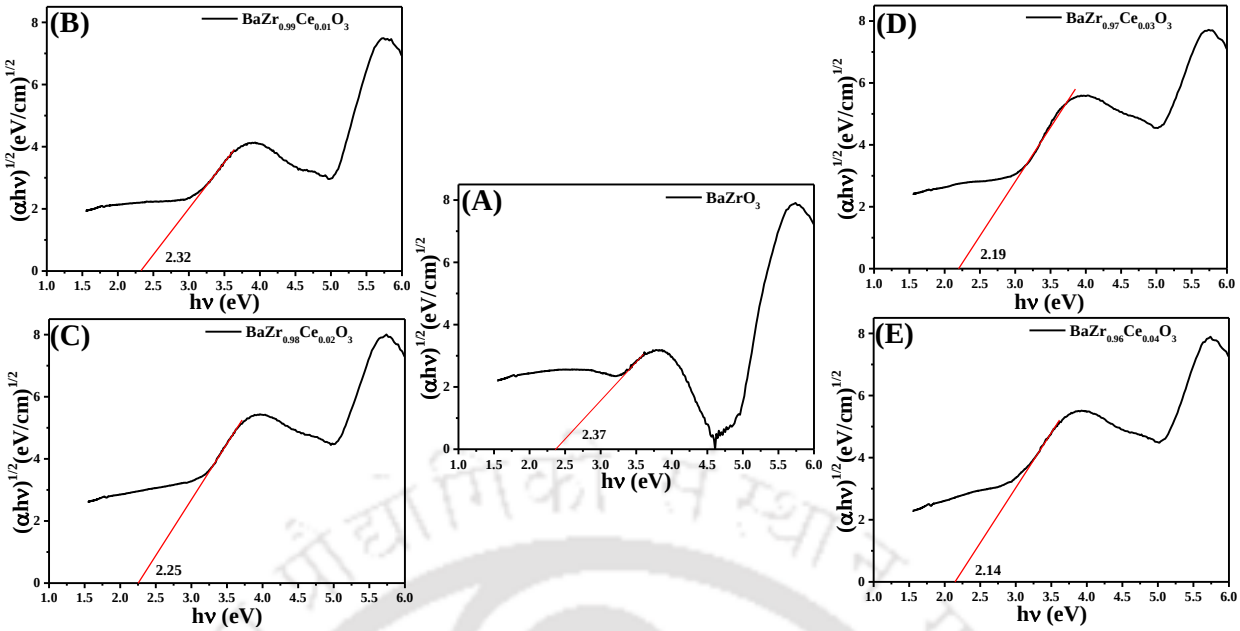

Figure 5.7 Tauc plot and calculated band gap of as-synthesized $BaZr_{1-x}Ce_xO_3$ (x = 0.00 – 0.04) catalysts.

disordered states can form additional mid-gap energy levels in the $BaZr_{1-x}Ce_xO_3$ (x = 0.00 – 0.04) lattice. From preceding reports we know that surface oxygen vacancies with a pair of free trapped electrons form an additional mid-gap adjacent to the valence band whereas oxygen vacancies with zero trapped electrons form an additional mid-gap state adjacent to the conduction band of the material and paramagnetic oxygen vacancies with one unpaired trapped electron form mid-gap states with in the band gap of the material.[29] Owing to the presence of Ce in Ce (III)/Ce (IV) mixed oxidation states, it creates an additional impurity level within the band gap of BZO which act as electron acceptor/trap centers leading to enhanced light absorption and charge separation.[30] We have calculated the band gap of all the compounds by the Tauc method and shown in Figure **5.7**.[31] From Figure **5.7**, we have observed that the band gap of parent BZO is 2.37 eV and with Ce doping the band gap of the materials decreased linearly.

5.3.4 X-ray Photoelectron Spectroscopy (XPS) Spectra

To gain a better understanding about the core-level electronic structure of the constituent elements as well as the surface properties of as-synthesized compounds, XPS analyses were performed. A typical survey spectrum of $BaZr_{0.97}Ce_{0.03}O_3$ is presented in Figure **5.8(C)**, which shows the presence of all elements, viz., Ba, Zr, O and Ce. Figure **5.8(A)** shows the high resolution XPS spectra of Ba 3d of BZO and $BaZr_{0.97}Ce_{0.03}O_3$, respectively. The Ba 3d

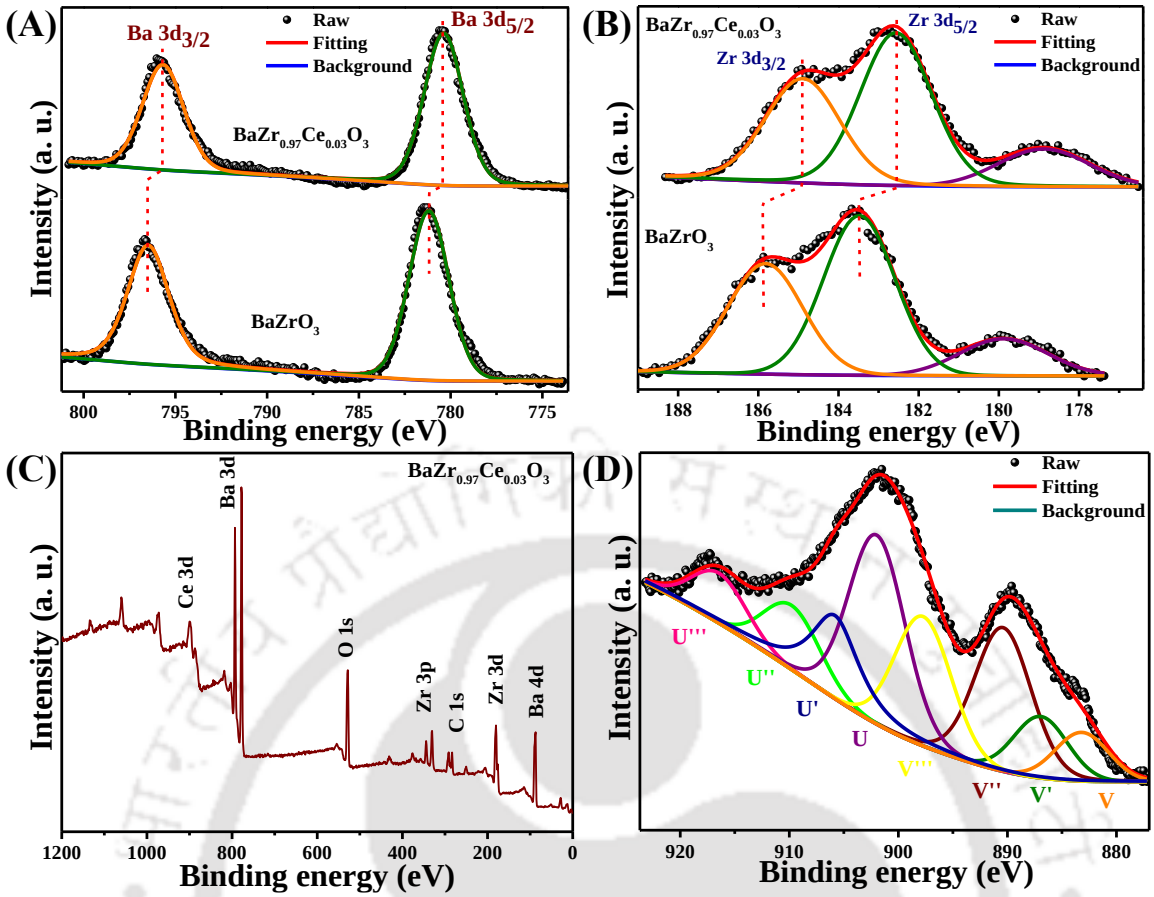

Figure 5.8 XPS spectra of (A) Ba 3d of $BaZrO_3$ and $BaZr_{0.97}Ce_{0.03}O_3$, (B) Zr 3d of $BaZrO_3$ and $BaZr_{0.97}Ce_{0.03}O_3$, (C) survey spectrum of $BaZr_{0.97}Ce_{0.03}O_3$ and (D) Ce 3d core levels of $BaZr_{0.97}Ce_{0.03}O_3$.

core level XPS spectra of BZO appears at a binding energy (B. E.) of 781.18 eV and 796.48 eV, which corresponds to the Ba $3d_{5/2}$ and Ba $3d_{3/2}$ respectively. Ba 3d core level XPS spectra of $BaZr_{0.97}Ce_{0.03}O_3$ appears at 780.38 eV and 795.68 eV, corresponding to Ba $3d_{5/2}$ and Ba $3d_{3/2}$ respectively. Although the peak positions little deviated from the previously reported values, the peak separation energy between the two peaks in the Ba 3d doublet ($\Delta E_{B.\,E.}$ = B. E. $3d_{3/2}$ – B. E. $3d_{5/2}$) is found to be ~15.3 eV, which supports our peak assignment.[32] Zr 3d XPS spectra of $BaZrO_3$ and $BaZr_{0.97}Ce_{0.03}O_3$ are shown in Figure **5.8(B)**. This peak can be deconvoluted into three peaks with binding energies of 179.88 eV, 183.48 eV and 185.82 eV for $BaZrO_3$ and 178.88 eV, 182.57 eV and 184.89 eV for $BaZr_{0.97}Ce_{0.03}O_3$ corresponding to Ba 4p, Zr $3d_{5/2}$ and Zr $3d_{3/2}$, respectively.[33] Although the peak positions little deviated from the previously reported values, the peak separation energy between the two peaks in the Zr 3d doublet ($\Delta E_{B.\,E.}$ = B. E. $3d_{3/2}$ – B. E. $3d_{5/2}$) is found to be ~2.3 eV, which supports our peak assignment.[32] The XPS spectra of Ce 3d of $BaZr_{0.97}Ce_{0.03}O_3$ is shown in Figure **5.8(D)**. Due

to a very low concentration of Ce in $BaZr_{0.97}Ce_{0.03}O_3$, the shape of the spectra is not as distinct as for pure CeO_2. The Ce 3d XPS spectral analysis is complicated due to spin-orbit coupling between Ce 4f and O 2p electrons, leading to the structured peaks.[34] Many reports have shown that Ce 3d spectra can consist of eight peaks with four pairs of spin-orbit coupling contributions, viz. u/v, u'/v', u''/v'' and u'''/v''', where u and v symbolize two sets of spin-orbital multiplets, viz. Ce $3d_{5/2}$ and Ce $3d_{3/2}$ respectively.[34, 35] From the preceding reports, the u'/v' bands arise in the Ce 3d spectrum for Ce(III) $3d_{5/2}$ and Ce(III) $3d_{3/2}$, respectively. The other three pairs of peaks are generated from spin-orbit coupling for Ce(IV) $3d_{5/2}$ and Ce(IV) $3d_{3/2}$. In this spectra, the fraction of Ce(III) present can be evaluated by dividing the total integrated peak intensity for Ce(III) by that due to both Ce(IV) and Ce(III).[36] Here, we found that the fraction of Ce(III) in $BaZr_{0.97}Ce_{0.03}O_3$ is 20%. From this analysis, it is clear that in Ce-doped BZO samples, Ce exists in a mixed valence state of Ce(III) and Ce(IV). Consequently, to neutralize the charge imbalance in doped compounds due to the formation of Ce(III), additional oxygen vacancies are created.[37, 38] Progressive increase in the intensity of the absorption band tail in the UV-Vis DRS is also an evidence that the cerium doping has a direct impact on the increase in oxygen vacancies.

To investigate the presence of oxygen vacancies we analyzed the high-resolution XPS spectra of O 1s as shown in Figure **5.9(A)**. Deconvolution of an asymmetric shaped O 1s peak of BZO shows two peaks positioned at 531.71 eV and 533.54 eV corresponding to lattice oxygen ($O_{latt.}$) and adsorbed oxygen ($O_{ads.}$) in the oxygen deficient region within the compound matrix

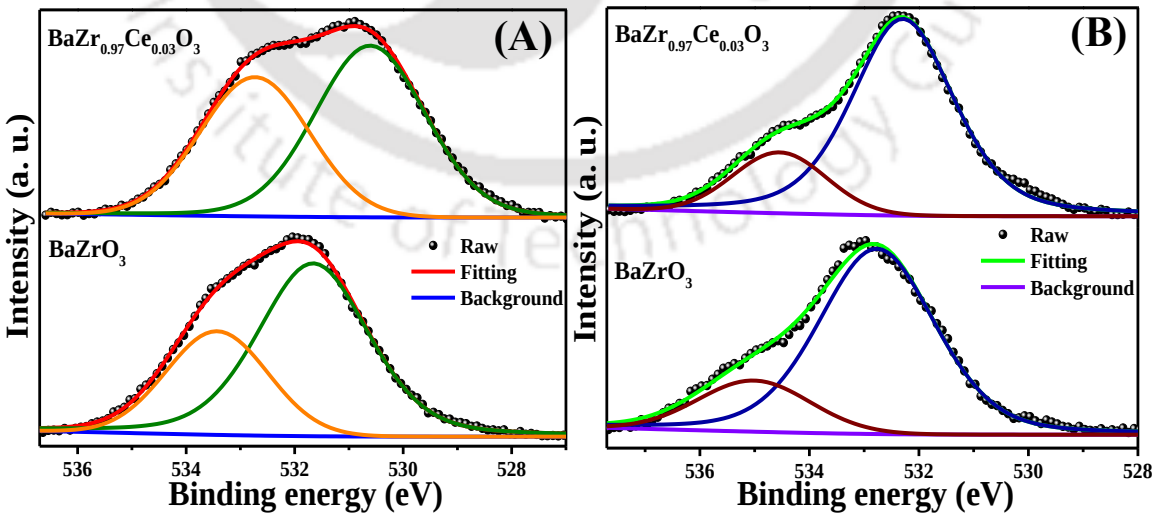

Figure 5.9 O 1s core level XPS spectra of $BaZrO_3$ and $BaZr_{0.97}Ce_{0.03}O_3$, (A) before and (B) after annealing in air at 700 °C for 2 h.

and surface H_2O, respectively.[39] The two fitted deconvoluted bands of O 1s peak for $BaZr_{0.97}Ce_{0.03}O_3$ appear at 530.61 eV and 532.73 eV. The area under the fitted band of non-lattice oxygen ($O_{ads.}$) in $BaZr_{0.97}Ce_{0.03}O_3$ is larger than that of $BaZrO_3$ suggesting that with Ce doping, the number of oxygen vacancy increases in the doped $BaZrO_3$, complimented by the UV-Vis DRS data of the as-synthesized compounds in Figure **5.6**. The Ba 3d, O 1s, and Zr 3d peaks are all shifted to lower energy in the Ce-doped compounds compared to the undoped BZO. The spectral shifts in XPS are attributed to the change in chemical environment around the Ba, Zr, O in the Ce doped compounds due the larger size of Ce(IV) and its decreased electronegativity as compared to Zr(IV).[11, 40]

We have calcined all the compounds at 700 °C in a box furnace under air for 2h to further support our claim of oxygen vacancies. It is known that oxygen vacancies of a compound could be moderately reduced by calcining at an elevated temperature under air or oxygen atmosphere.[41] The high-resolution O 1s core level XPS spectra of the calcined products are shown in Figure **5.9(B)**. It is clear that after calcination, the intensity of the peak corresponding to the oxygen vacancy reduces due to the partial filling up of oxygen vacancies by atmospheric oxygen.

5.3.5 Electron Spin Resonance (ESR) Spectra

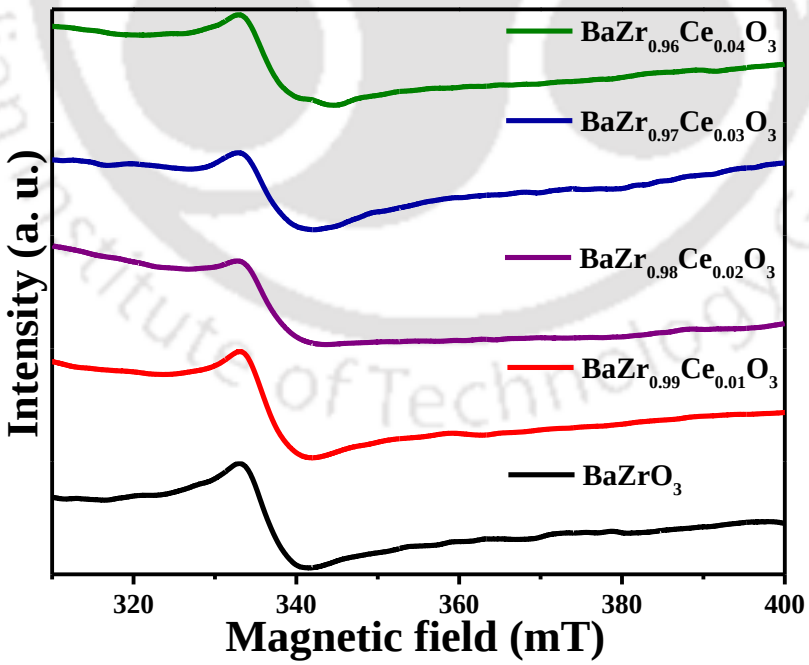

Figure 5.10 Room temperature ESR spectra of as-synthesized $BaZr_{1-x}Ce_xO_3$ (x = 0.00 – 0.04) catalysts.

One of the key parameters proposed to control photocatalytic activity in our materials is the concentration of oxygen vacancies. Hence, it is important to understand the nature of oxygen vacancies that are present in doped BZO. There is literature precedent that suggests that there are three different types of oxygen vacancies that can be present in a compound: neutral with two free electrons, singly ionized with one free electron, and doubly ionized with no free electrons.[42] Taking advantage of the spin state, the nature of the oxygen species in these compounds can be analyzed by the ESR technique. As the singly ionized oxygen vacancy has only one unpaired electron, it gives rise to a strong ESR signal. Therefore, we performed room-temperature ESR measurements of all as-synthesized compounds and the data is presented in Figure **5.10**. From Figure **5.10**, we observe that the BZO and Ce-doped BZO compositions show a peak at around g-tensor value of 2.005, which is due to the singly ionized paramagnetic oxygen vacancies ($V_O^{\bullet}$).[43] In doped compounds, Ce(IV) ions cannot give rise to a resonance peak under magnetic field as their outer electrons are paired but Ce(III) ions have unpaired electrons in their outer shell, which can give rise to a resonance peak under magnetic field. However, in this analysis, we could not find any characteristic peak of Ce(III) in doped samples, which might be due to the weak crystal field of Ce(III) owing to the shielding effect created by the outer electrons.

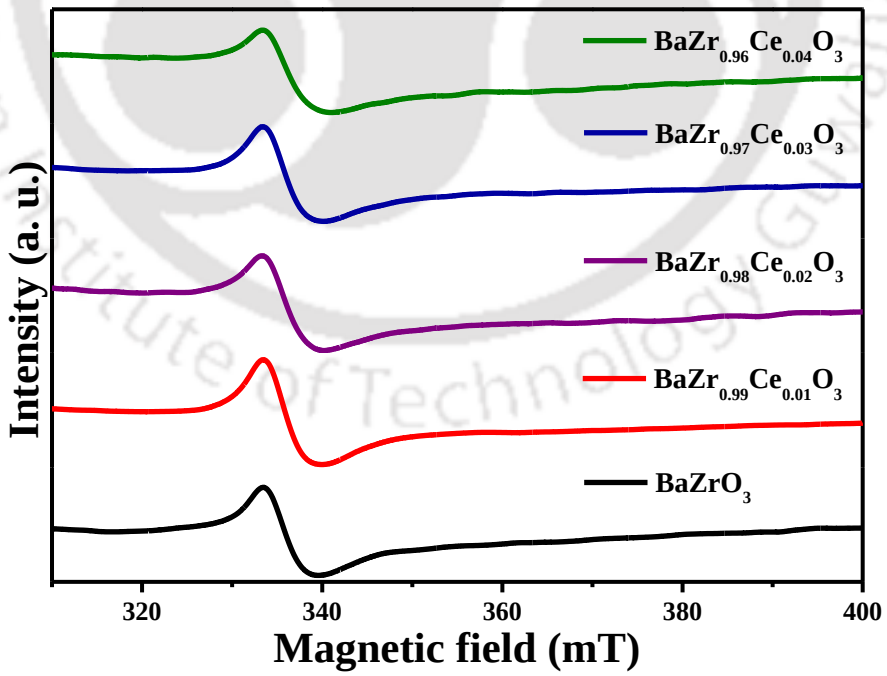

Figure 5.11 Room temperature ESR spectra of $BaZr_{1-x}Ce_xO_3$ (x = 0.00 – 0.04) catalysts calcined at 700°C for 2h under air.

To check the presence of oxygen vacancies in calcined photocatalysts, we performed ESR analysis on all compounds and observed a sharp peak at around g-tensor value of ~2.005, corresponding to the singly ionized paramagnetic oxygen vacancies (Figure **5.11**). These results from XPS and ESR indicate that all the photocatalysts retain oxygen vacancies in their structure even after calcination at 700 °C for 2 h under air. Hence, from these above findings we can say that all the compounds in this study are suffered from ordered-disordered type of lattice defects with considerable amount of oxygen vacancies. The presence of these defects could be represented by Kröger-Vink notation,[44]

$$[ZrO_6]^x + [ZrO_5.V_O^x] \longrightarrow [ZrO_6]' + [ZrO_5.V_O^{\bullet}]$$

$$[ZrO_6]^x + [ZrO_5.V_O^{\bullet}] \longrightarrow [ZrO_6]' + [ZrO_5.V_O^{\bullet\bullet}]$$

$$[ZrO_5.V_O^{\bullet}] + \frac{1}{2}\,O_2 \longrightarrow [ZrO_6]$$

5.3.6 XPS Valence Band Spectra

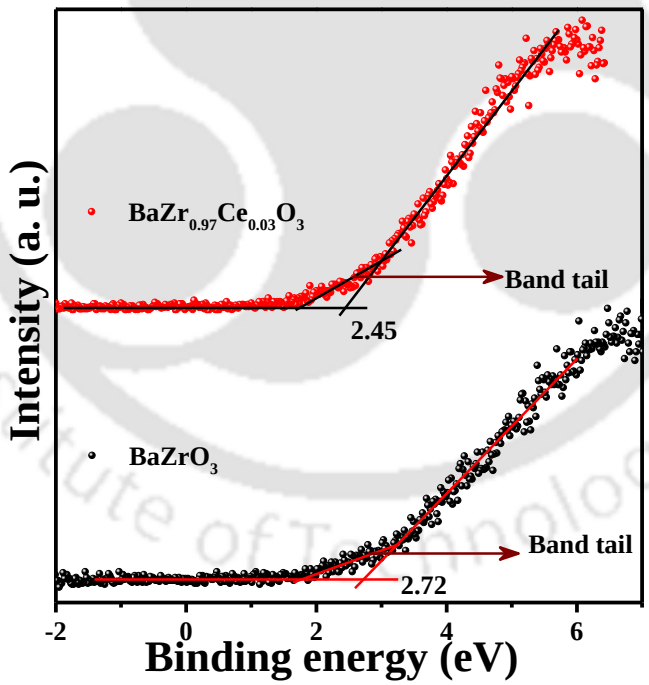

Figure 5.12 XPS valence band spectra of $BaZrO_3$ and $BaZr_{0.97}Ce_{0.03}O_3$.

Experimentally the position of valence band maxima of a material can be derived by fitting the XPS valence band spectra. The XPS valence band spectra of $BaZrO_3$ and $BaZr_{0.97}Ce_{0.03}O_3$ are shown in Figure **5.12**, where we see that with doping, the position of valence band is

shifted towards lower binding energy. This shift in valence band maxima in Ce-doped materials clearly indicates the formation of a defect/impurity band next to the valence band. The band tail in both the spectra reveals the presence of lattice disorder in the compounds.[45] The enhanced light absorption of $BaZr_{1-x}Ce_xO_3$ ($x = 0.00 - 0.04$) compounds can be explained by the electronic transition from the valence band tail to oxygen vacancies to the conduction band or to the impurity level due to cerium doping beneath the conduction band. We have calculated the valence band and conduction band positions of all the compounds (Table **5.2)** and found that the band positions are also changing with Ce doping as we have found in XPS valence band spectra.

5.3.7 Calculation of Band Position

The valence band position of an inorganic semiconductor can be interpreted according to the following formulas as proposed by Xu and Schoonen,[46]

$$E_{VB} = \left(\chi_M{}^a \chi_X{}^b\right)^{\frac{1}{a+b}} + \frac{1}{2}E_g - E^e \quad \ldots \text{(i)}$$

$$\chi = \frac{1}{2}\,(IP + EA) \quad \ldots\ldots \text{(ii)}$$

$$E_{CB} = E_{VB} - E_g \quad \ldots\ldots\ldots \text{(iii)}$$

Here, E_{VB} denotes the valence band maxima (VBM), E_{CB} denotes the conduction band minima (CBM), E_g is the band gap of the semiconductor calculated from Tauc plot, E^e stands for energy of free electrons on the hydrogen scale (– 4.5 eV), χ_M and χ_X are the absolute electronegativities of M and X atoms, respectively. χ is the electronegativity of the individual atoms of the multi-atomic semiconductor, calculated using equation (ii), IP is the ionization potential and EA is the electron affinity values of each atom.

The IP values for Ba, Zr, O and Ce atoms are 5.211 eV, 6.633 eV, 13.6 eV and 5.538 eV, respectively. While the EA values of Ba, Zr, O and Ce atoms are 0.144 eV, 0.427 eV, 1.46 eV and 0.57 eV, respectively. From equation (ii), the calculated absolute electronegativity values of Ba, Zr, O and Ce are 2.672 eV, 3.515 eV, 7.535 eV and 3.035 eV, respectively. Hence, the calculated absolute electronegativity values of $BaZrO_3$, $BaZr_{0.99}Ce_{0.01}O_3$, $BaZr_{0.98}Ce_{0.02}O_3$, $BaZr_{0.97}Ce_{0.03}O_3$ and $BaZr_{0.96}Ce_{0.04}O_3$ as the geometric mean of the electronegativity values for each of the constituent atoms are 5.258 eV, 5.256 eV, 5.254 eV, 5.253 eV and 5.251 eV, respectively. The valence band maxima and conduction band minima calculated by using equations (i) and (iii) are shown in Table **5.2**.

Table 5.2 Calculated values of valence band maxima, conduction band minima and band gap of $BaZr_{1-x}Ce_xO_3$ (x = 0.00 – 0.04).

Compound	Valence band maxima (eV)	Conduction band minima (eV)	Band gap (eV)
$BaZrO_3$	1.943	-0.427	2.37
$BaZr_{0.99}Ce_{0.01}O_3$	1.916	-0.404	2.32
$BaZr_{0.98}Ce_{0.02}O_3$	1.879	-0.371	2.25
$BaZr_{0.97}Ce_{0.03}O_3$	1.848	-0.342	2.19
$BaZr_{0.96}Ce_{0.04}O_3$	1.821	-0.319	2.14

5.3.8 Photocatalytic Hydrogen Production

Ultraviolet-visible radiation assisted H_2 evolution from water by $BaZr_{1-x}Ce_xO_3$ (x = 0.00 – 0.04) photocatalysts were analyzed in the presence of 0.25 M Na_2SO_3/0.35 M Na_2S mixture as the sacrificial reagent for photogenerated holes. The data are shown in Figure **5.13**, and clearly indicate that photocatalytic H_2 production efficiency in Ce doped BZO is higher than that of the BZO and $BaZr_{0.07}Ce_{0.03}O_3$ shows highest photocatalytic efficacy among all the catalysts. The valence band maxima of the photocatalysts is more positive than the H_2O/O_2 reduction potential and the conduction band minima is more negative than the H_2/H^+ redox potential.[1, 8] Upon photo-excitation of the semiconductor by light of suitable energy, photo-generated electrons and holes are produced. These photogenerated charge carriers may diffuse to the surface of the catalyst where they react with the reactants. It is well known that during photocatalytic H_2 evolution, the reduction of photogenerated holes by using a sacrificial reagent can enhance its efficiency as the sacrificial reagent can consume the photogenerated holes in the valence band of the semiconductor and leaves the photogenerated electrons in the conduction band, which in turn reduces the charge carrier recombination and thereby enhances the charge separation.[47, 48]

In this work, the amount of H_2 gas produced by as-synthesized BZO is 316 µmol per hour per gram. Compared to parent BZO, the Ce doped BZO photocatalysts exhibit superior catalytic activity, inferring the beneficial role of Ce-doping in BZO. The improved H_2 production efficacy can be attributed to the change in electronic structure and enhanced light absorption

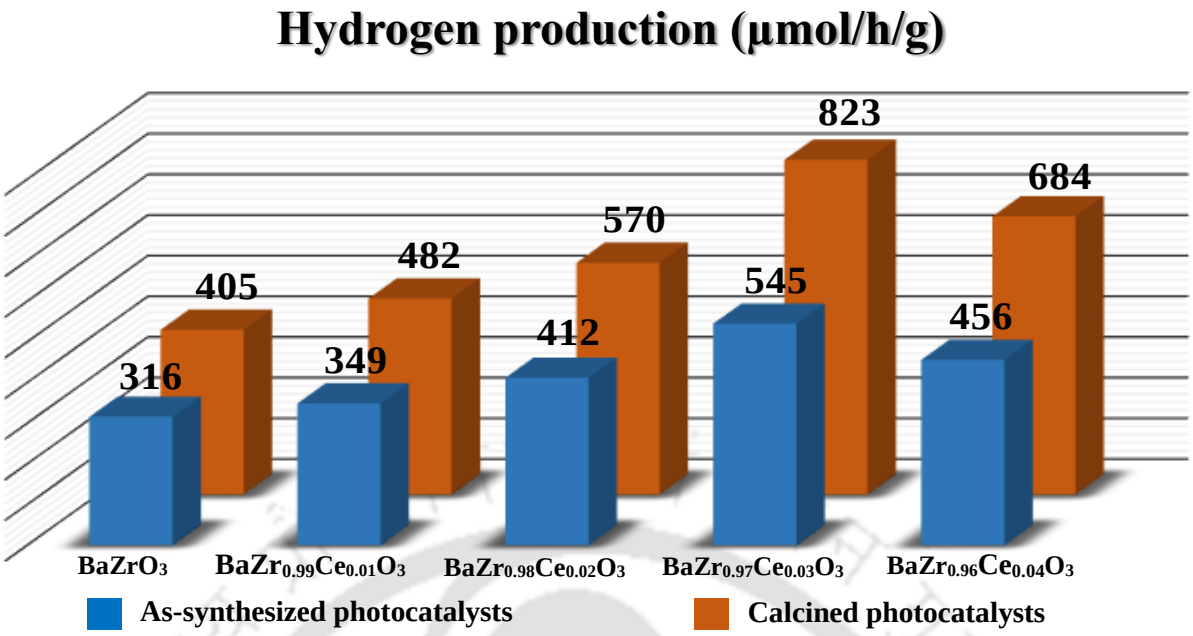

Figure 5.13 Rate of photocatalytic hydrogen gas evolution of $BaZr_{1-x}Ce_xO_3$ ($x = 0.00 – 0.04$) catalysts under UV-visible light irradiation with 0.25 M Na_2SO_3/0.35 M Na_2S mixture as sacrificial reagent.

of the catalysts in the visible light regime after Ce doping. From Figure **5.13** we note that in as-synthesized compounds, 3 atom% is the optimal Ce doping concentration for the highest amount of H_2 gas evolution (545 µmol/h/g), whereas, $BaZr_{0.99}Ce_{0.01}O_3$, $BaZr_{0.98}Ce_{0.02}O_3$ and $BaZr_{0.96}Ce_{0.04}O_3$ produces 349 µmol/h/g, 412 µmol/h/g and 456 µmol/h/g of H_2 gas respectively. The calculated AQY values of H_2 production of as-synthesized BZO, $BaZr_{0.99}Ce_{0.01}O_3$, $BaZr_{0.98}Ce_{0.02}O_3$, $BaZr_{0.97}Ce_{0.03}O_3$ and $BaZr_{0.96}Ce_{0.04}O_3$ are 2.3%, 2.6%, 3%, 4% and 3.3% respectively. It is observed that beyond 3 atom% Ce doping, the H_2 gas production efficacy decreases which can be explained by the formation of defect states which act as a charge carrier recombination site.[49] After calcination at 700 °C for 2 h under air the efficiency of all the catalysts increased to 405 µmol/h/g (BZO), 482 µmol/h/g ($BaZr_{0.99}Ce_{0.01}O_3$), 570 µmol/h/g ($BaZr_{0.98}Ce_{0.02}O_3$), 823 µmol/h/g ($BaZr_{0.97}Ce_{0.03}O_3$) and 684 µmol/h/g ($BaZr_{0.96}Ce_{0.04}O_3$). The calculated AQY values of H_2 production of calcined BZO, $BaZr_{0.99}Ce_{0.01}O_3$, $BaZr_{0.98}Ce_{0.02}O_3$, $BaZr_{0.97}Ce_{0.03}O_3$ and $BaZr_{0.96}Ce_{0.04}O_3$ are 3%, 3.5%, 4.2%, 6% and 5% respectively. From the O 1s XPS spectra and ESR analysis, we have found that even after calcination the catalysts possess certain amount of oxygen vacancies in their lattice. Therefore, the increase in photocatalytic efficiency in these catalysts after calcination could be due to the reduction of crystal defects and increase in crystallinity.

5.4 CONCLUSIONS

In summary, barium zirconate and cerium doped barium zirconate hollow spheres have been successfully synthesized using a low-temperature template-free hydrothermal method. All the compounds show cubic phase with a high range of crystallinity. The as-synthesized compounds produced hydrogen upon illumination without any co-catalysts but in the presence of sacrificial donor molecules. As found from UV-Vis DRS, XPS and ESR analysis, the presence of disordered lattice, oxygen vacancies and cerium doping play a critical role in enhancing the photocatalytic activity in the ultraviolet-visible region. $BaZr_{0.97}Ce_{0.03}O_3$ among all the as-synthesized compounds, $BaZr_{1-x}Ce_xO_3$ (x = 0.00 – 0.04), shows the highest efficiency in hydrogen gas production concomitant with oxidation of a sacrificial donor.

5.5 REFERENCES

1. Tao, S.; Irvine, J. T. S. *J. Solid State Chem.* **2007**, *180*, 3493.
2. MacManus-Driscoll, J. L.; Foltyn, S. R.; Jia, Q. X.; Wang, H.; Serquis, A.; Civale, L.; Maiorov, B.; Hawley, M. E.; Maley, M. P.; Peterson, D. E. *Nat. Mater.* **2004**, *3*, 439.
3. Bennett, J. W.; Grinberg, I.; Rappe, A. M. *Phys. Rev. B* **2006**, *73*, 180102.
4. Yuan, Y.; Zhang, X.; Liu, L.; Jiang, X.; Lv, J.; Li, Z.; Zou, Z. *Int. J. Hydrogen Energy* **2008**, *33*, 5941.
5. Yerga, R. M. N.; Galvan, M. C. Á.; del Valle, F.; Mano, J. A. V.; Fierro, J. L. G. *ChemSusChem*, **2009**, *2*, 471.
6. Wang, G.; Ling, Y.; Li, Y. *Nanoscale* **2012**, *4*, 6682.
7. Pesci, F. M.; Wang, G.; Klug, D. R.; Li, Y.; Cowan, A. J. *J. Phys. Chem. C* **2013**, *117*, 25837.
8. Lv, Y.; Zhu, Y.; Zhu, Y. *J. Phys. Chem. C* **2013**, *117*, 18520.
9. Huo, Y.; Chen, X.; Zhang, J.; Pan, G.; Jia, J.; Li, H. *Appl. Catal., B* **2014**, *148*, 550.
10. Li, H.; Bian, Z.; Zhu, J.; Zhang, D.; Li, G.; Huo, Y.; Li, H.; Lu, Y. *J. Am. Chem. Soc.* **2007**, *129*, 8406.
11. Yuan, Y.; Zhao, Z.; Zheng, J.; Yang, M.; Qiu, L.; Li, Z.; Zou, Z. *J. Mater. Chem.* **2010**, *20*, 6772.
12. Borja-Urby, R.; Díaz-Torres, L. A.; Salas, P.; Moctezuma, E.; Vega, M.; Ángeles-Chávez, C. *Mater. Sci. Eng. B.* **2011**, *176*, 1382.
13. Weber, A. S.; Grady, A. M.; Koodali, R. T. *Catal. Sci. Technol.* **2012**, *2*, 683.
14. Zhang, Y.; Yuwono, A. H.; Wang, J.; Li, J. *J. Phys. Chem. C* **2009**, *113*, 21406.
15. Nasir, M.; Xi, Z.; Xing, M.; Zhang, J.; Chen, F.; Tian, B.; Bagwasi, S. *J. Phys. Chem. C* **2013**, *117*, 9520.
16. Dong, Z.; Ye, T.; Zhao, Y.; Yu, J.; Wang, F.; Zhang, L.; Wang, X.; Guo, S. *J. Mater. Chem.* **2011**, *21*, 5978.

17. Bandura, A. V.; Evarestov, R. A.; Kuruch, D. D. *Surf. Sci.* **2010**, *604*, 1591.
18. Charoonsuk, T.; Vittayakorn, N. *Mater. Des.* **2017**, *118*, 44.
19. Ye, T.; Dong, Z.; Zhao, Y.; Yu, J.; Wang, F.; Guo, S.; Zou, Y. *Langmuir* **2011**, *27*, 8878.
20. Li, J.; Zeng, H. C. *J. Am. Chem. Soc.* **2007**, *129*, 15839.
21. Yin, X. M.; Li, C. C.; Zhang, M.; Hao, Q. Y.; Liu, S.; Chen, L. B.; Wang, T. H. *J. Phys. Chem. C* **2010**, *114*, 8084.
22. Zou, Y.; Luo, Y.; Wen, N.; Ye, T.; Xu, C.; Yu, J.; Wang, F.; Li, G.; Zhao, Y. *New J. Chem.* **2014**, *38*, 2548.
23. Moreira, M. L.; Longo, V. M.; Avansi, W.; Ferrer, M. M.; Andrés, J.; Mastelaro, V. R.; Varela, J. A.; Longo, É. *J. Phys. Chem. C* **2012**, *116*, 24792.
24. Clark, I. J.; Takeuchi. T.; Ohtori, N.; Sinclair, D, C. *J. Mater. Chem.* **1999**, *9*, 83.
25. Zhang, J.; Liu, S.; Yu, J.; Jaroniec, M. *J. Mater. Chem.* **2011**, *21*, 14655.
26. Souza, A. E.; Teixeira, S. R.; Santos, C. M.; Schreiner, W. H.; Lisboa Filho, P. N.; Longo, E. *J. Mater. Chem. C* **2014**, *2*, 7056.
27. Dhahri, K.; Bejar, M.; Dhahri, E.; Graça, M. F. P.; Zaoui, A. *Chem. Phys. Lett.* **2015**, *635*, 228.
28. Kröger, F. A.; Vink, H. J. *Solid State Phys.* **1956**, *3*, 307.
29. Deb, S. K. *Sol. Energy Mater. Sol. Cells* **2008**, *92*, 245.
30. Xu, J.; Ao, Y.; Fu, D. *Appl. Surf. Sci.* **2009**, *256*, 884.
31. Tauc, J.; Grigorovici, R.; Vancu, A. *Phys. Status Solidi* **1966**, *15*, 627.
32. Wagner, D.; Muilenberg, G. E. *Handbook of X - ray Photoelectron Spectroscopy: A Reference Book of Standard Data for Use in X- ray Photoelectron Spectroscopy, Physical Electronics Division, Perkin- Elmer Corp*., **1979**.
33. Sun, W.; Shi, Z.; Liu, M.; Bi, L.; Liu, W. *Adv. Funct. Mater.* **2014**, 24, 5695.
34. Raj, A. K. V; Rao, P. P.; Sreena, T. S.; Sameera, S.; James, V.; Renju, U. A. *Phys. Chem. Chem. Phys.* **2014**, *16*, 23699.
35. Dai, Z.; Qin, F.; Zhao, H.; Ding, J.; Liu, Y.; Chen, R. *ACS Catal.* **2016**, *6*, 3180.
36. Kumar, A.; Babu, S.; Karakoti, A. S.; Schulte, A.; Seal, S. *Langmuir* **2009**, *25*, 10998.
37. Zhang, C.; Lin, J. *Phys. Chem. Chem. Phys.* **2011**, *13*, 3896.
38. Khan, M. M.; Ansari, S. A.; Pradhan, D.; Han, D. H.; Lee, J.; Cho, M. H. *Ind. Eng. Chem. Res.* **2014**, *53*, 9754.
39. Jaiswar, S.; Mandal, K. D. *J. Phys. Chem. C* **2017**, *121*, 19586.
40. Wang, J.; Yu, Y.; Li, S.; Guo, L.; Wang, E.; Cao, Y. *J. Phys. Chem. C* **2013**, *117*, 27120.
41. Drouilly, C.; Krafft, J. M.; Averseng, F.; Casale, S.; Bazer-Bachi, D.; Chizallet, C.; Lecocq, V.; Vezin, H.; Lauron-Pernot, H.; Costentin, G. *J. Phys. Chem. C* **2012**, *116*, 21297.
42. Sanyal, K.; Pathak, N.; Yadav, A. K.; Kanrar, B.; Kadam, R. M.; Jha, S. N.; Bhattacharya, D.; Misra, N. L. *Dalton Trans.* **2016**, *45*, 7650.

43. Cavalcante, L. S.; Longo, V. M.; Zampieri, M.; Espinosa, J. W. M.; Pizani, P. S.; Sambrano, J. R.; Varela, J. A.; Longo, E.; Simões, M. L.; Paskocimas, C. A. *J. Appl. Phys.* **2008**, *103*, 063527.

44. Matta, J.; Lamonier, J. F.; Abi-Aad, E.; Zhilinskaya, E. A.; Aboukaïs, A. *Phys. Chem. Chem. Phys.* **1999**, *1*, 4975.

45. Naldoni, A.; Allieta, M.; Santangelo, S.; Marelli, M.; Fabbri, F.; Cappelli, S.; Bianchi, C. L.; Psaro, R.; Dal Santo, V. *J. Am. Chem. Soc.* **2012**, *134*, 7600.

46. Xu, Y.; Schoonen, M. A. A. *Am. Mineral.* **2000**, 85, 543.

47. Gogoi, G.; Arora, S.; Vinothkumar, N.; De, M.; Qureshi, M. *RSC Adv.* **2015**, *5*, 40475.

48. Bao, N.; Shen, L.; Takata, T.; Domen, K. *Chem. Mater.* **2008**, *20*, 110.

49. Xiao, G.; Huang, X.; Liao, X.; Shi, B. *J. Phys. Chem. C* **2013**, *117*, 9739.

Chapter 6

Synergistic Effect of Upconversion Luminescent Carbon Dots and Oxygen Vacancies in Enhancing the Photocatalytic Efficiency of Stable $BaZrO_{3-\delta}$ Hollow Nanospheres.

This Chapter illustrates a hybrid nanomaterial of carbon dots (CDs)–barium zirconate hollow spheres ($BaZrO_{3-\delta}$), xCDs_ $BaZO_{3-\delta}$ (x = 0 – 4) and their photocatalytic activity. Presence of oxygen vacancies, disordered states and upconversion photoluminescence property of CDs shift the absorbance onset of $BaZO_{3-\delta}$ towards longer wavelength. Compared to bare $BaZrO_{3-\delta}$, CDs incorporated onto $BaZrO_{3-\delta}$ shows enhancement in hydrogen production and efficient methylene blue (MB) dye degradation owing to the upconversion photoluminescence property and high photogenerated charge transfer capability of CDs.

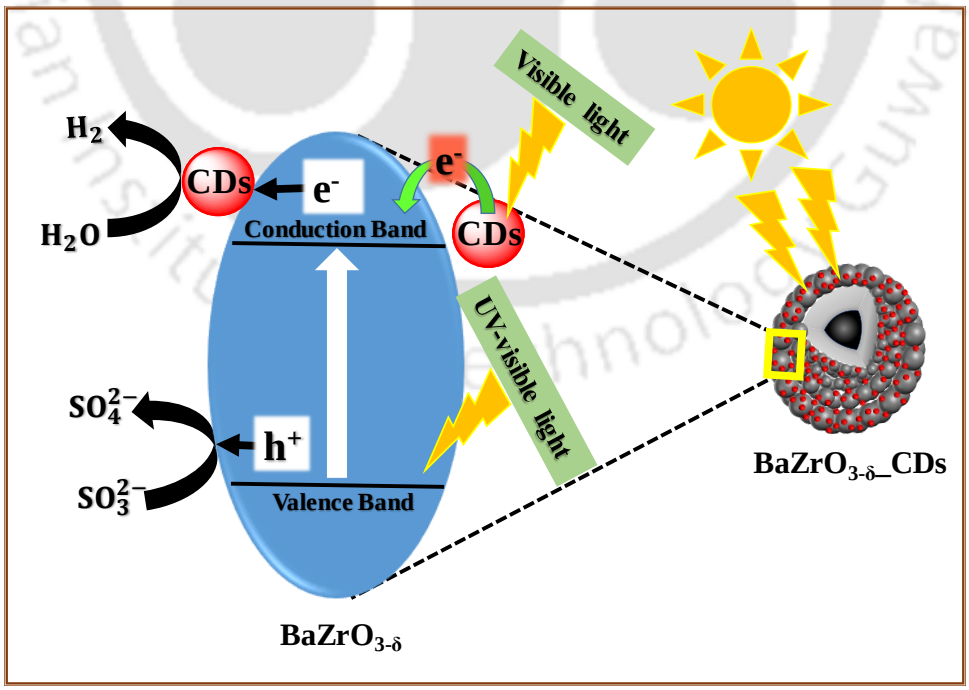

Manuscript under communication

6.1 INTRODUCTION

Recently, fluorescent carbon nanoparticles, referred to as carbon dots (CDs) herein, a new class of carbon-based zero-dimensional (< 10 nm) material have gained massive attention in numerous research areas like photocatalysis, photovoltaics, sensing, bioimaging, optoelectronics etc. owing to its ease in synthesis, processing and functionalization, low cost, low toxicity, high water solubility, exceptional photoinduced electron transfer ability, high surface area and so on.[1–7] Because of these properties, CDs have been considered as a suitable replacement for organic dyes and semiconductor quantum dots.[8] CDs show tuneable absorbance and luminescence properties because of its surface modification. Apart from general downconversion fluorescence properties, where the photoluminescence (PL) emission wavelength is longer than the excitation wavelength, some CDs also exhibit special type of optical properties called upconversion photoluminescence (UCPL) wherein it emits at shorter wavelength when excited at longer wavelength.[9] Owing to its UCPL properties, CDs can enhance the light absorption of a semiconductor to visible or even near-IR region.[10] From preceding works, it has been found that the introduction of CDs onto a photocatalyst can enhance its light absorption as well as photogenerated charge carrier separation.[11] To date, there are several reports of enhanced photocatalytic activity of CDs incorporated photocatalysts, such as, Yu *et al.* showed enhanced photocatalytic H_2 production by carbon quantum dots/TiO_2 composites, Song *et al.* reported enhanced photocatalytic rhodamine B dye degradation by carbon nano dots/WO_3 photocatalysts, Wang *et al.* reported enhanced overall water splitting and dye degradation by carbon dots/TiO_2 nanotube arrays, Tang *et al.* showed enhanced methylene blue dye degradation by carbon dots/$BiVO_4$ composites.[12–15]

The first step in photocatalysis involves light assisted excitation process, therefore, by improving the light absorbance in the visible region of the solar spectrum and efficiently separating the photogenerated carriers, the photocatalytic efficiency of wide band gap materials like $BaZrO_3$ could be improved. It is known that carbon-based nanomaterials can pave an efficient way to channelize the flow of photogenerated carriers owing to their superior electron accepting and transport properties.[11] So, the photocatalytic efficiency of a semiconductor could be increased through the design of a composite with carbon-based nanomaterial. In this chapter, we have synthesized CDs and $BaZrO_{3-\delta}$ (BZO) hollow nanospheres by a facile hydrothermal process and their composites varying the amount of CDs by dispersion method. The best performing hybrid photocatalyst has been assessed by the photocatalytic H_2 generation rate and methylene blue (MB) dye degradation efficiency.

6.2 EXPERIMENTAL SECTION

6.2.1 Preparation of Carbon Dots (CDs)

Water-soluble CDs were prepared by following a facile carbonation process via hydrothermal route.[16] 2.1g of citric acid was dissolved in 20 mL of water in a Teflon made reactor by continuous stirring. After complete dissolution of citric acid in water, 670 µL of ethylene diamine was added dropwise under vigorous stirring. This solution was then placed inside a stainless steel jacket and kept inside a pre-heated electric oven at 200 °C for 5h. After cooling down to room temperature, the brownish red solution was filtered through a 0.4-micron syringe filter to separate larger particles. This filtrate was then dialyzed by using a dialysis bag (Da = 1000) and Milli-Q water for 1 day to remove unreacted reagents. The water was changed in every 4 h. As-synthesized CDs were collected by drying the dialyzed solution at 80 °C overnight.

6.2.2 Preparation of $BaZrO_{3-\delta}$ (BZO)

Barium zirconate hollow spheres were prepared by following a modified hydrothermal method.[17] The reactions were carried out in a stainless-steel autoclave with Teflon liner at 200 °C and autogenous pressure. Initially, 20 M KOH aqueous solution was prepared in a round-bottom flask. This aqueous solution was kept under constant stirring until it attained room temperature. Then, a stoichiometric amount of $BaCl_2 \cdot 2H_2O$ and $ZrOCl_2 \cdot 8H_2O$ were mixed with the as-prepared KOH aqueous solution in a 100 mL Teflon made reactor. The solution was vigorously stirred for 1h and then sealed inside a stainless-steel autoclave and heated inside an electric oven at 200 °C for 24 h. The autoclave was allowed to cool down to room temperature naturally after the reaction. To remove the impurities, the obtained white precipitate of BZO was centrifuged and washed several times by water, dilute acetic acid and ethanol. Finally, the washed BZO was dried at 100 °C inside an electric oven for overnight.

6.2.3 Preparation of CDs_BZO Hybrid Nanomaterials

To prepare *x* wt% CDs_BZO (x = 0 – 4) (hereinafter referred to as "*x*C_BZO") hybrid nanomaterials with a different weight percentage of carbon dots, we have taken a certain amount of BZO in a round-bottomed flask and to it added the calculated amount of CDs. These compounds were then dispersed in ethanol at 45 °C for 2 h by sonication. Ethanol was removed in a rotary evaporator to collect the different hybrid compounds.

6.3 RESULTS AND DISCUSSION

6.3.1 Powder X-ray Diffraction (PXRD) Patterns

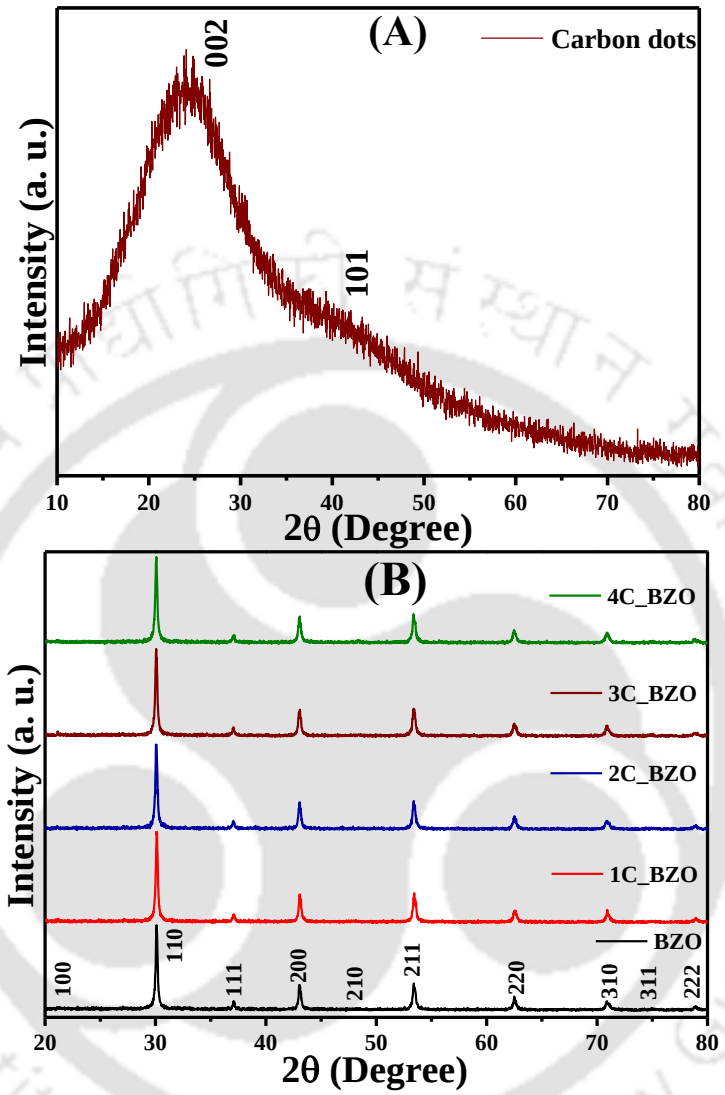

Figure 6.1 Powder X-ray diffractogram of (A) carbon dots and (B) *x*C_BZO (*x* = 0 – 4) hybrid nanomaterials.

Crystal structure and phase of the as-synthesized CDs and *x*C_BZO (*x* = 0 – 4) hybrid nanomaterials were determined by powder X-ray diffraction (PXRD) patterns. The PXRD pattern of CDs are shown in Figure **6.1(A)** and it exhibits one broad peak centered at ~ 25° and one less intense peak at ~ 42° which can be assigned to (002) and (101) planes of a highly disordered graphitic carbon, respectively.[18] Figure **6.1(B)** shows the PXRD pattern of bare BZO and *x*C_BZO (*x* = 1 – 4) hybrid nanomaterials. It is well observed that BZO is free from any impurity peaks and can be indexed to the cubic phase with $Pm\bar{3}m$ space group (no. 221)

[JCPDS file No.06-0399]. In the hybrid compounds, we cannot find any peak of carbon dots, which may be because of very low content of carbon dots in the hybrid compounds and very high crystallinity of BZO compared to CDs.[19] We did not notice any PXRD peak shifting of the bare and hybrid compounds that affirm the phase and structural retention of BZO in the hybrid compounds.

6.3.2 Fourier Transform Infrared (FTIR) Spectrum

The presence of different functional groups in the as-synthesized CDs is confirmed by its FT-IR analysis as shown in Figure **6.2**. A broad peak at ~ 3150 – 3750 cm^{-1} is attributed to the stretching frequency of –O–H and –N–H, peak at ~ 2940 cm^{-1} correspond to the sp^2–C–H stretching frequency Two strong peaks at 1650 cm^{-1} and 1558 cm^{-1} could be because of $\succ$C=O stretching and –N–H bending frequencies of secondary amines respectively. The different weak peaks at 1441 cm^{-1}, 1375 cm^{-1}, 1291 cm^{-1} and 1048 cm^{-1} could be attributed to different functional groups like sp^2 carbon, –C–N and –O–H respectively.

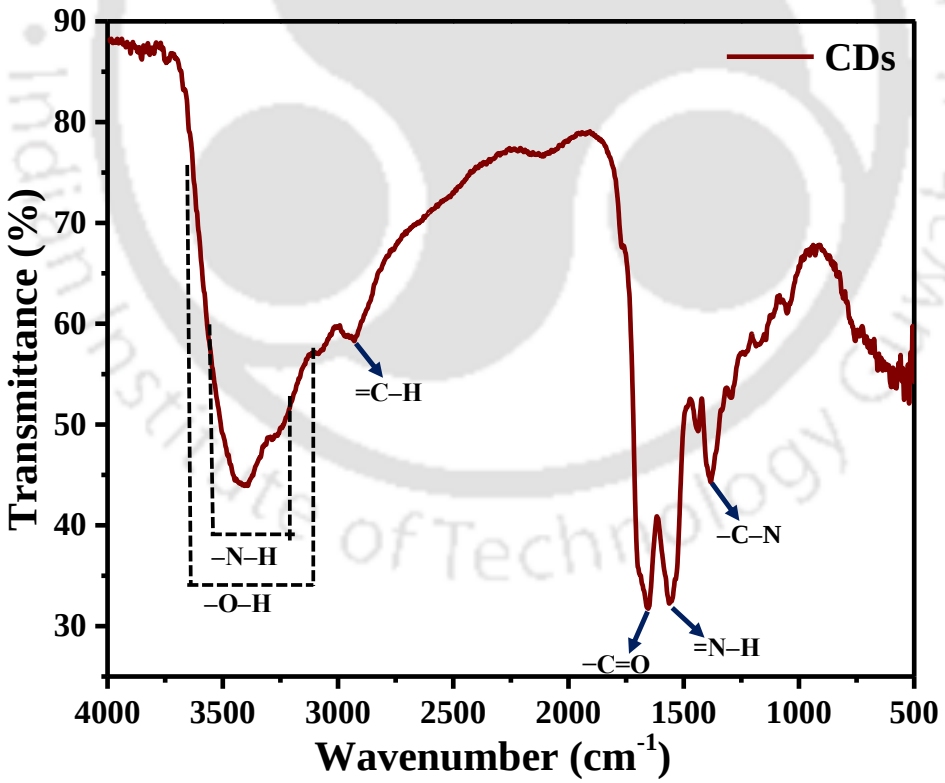

Figure 6.2 Fourier transform infrared spectrum of as-synthesized CDs.

The presence of hydroxyl, amines and carbonyl groups ensure high solubility of CDs in water.[20] Presence of different groups like sp^2 carbon, secondary amines and carbonyl groups prove the formation of polyaromatic structures during the synthesis of CDs.[21]

6.3.3 Raman Spectrum

Raman spectroscopy is a useful technique to differentiate the ordered and disordered phases of CDs. From the Raman spectra in Figure 6.3, we notice two different peaks at 1325 cm^{-1} and 1548 cm^{-1}, corresponding to the D band and G band respectively. The D band appears due to out of plane stretching vibration of sp^3 carbon atoms of the disordered states, whereas the G band arises from in-plane stretching vibration of sp^2 carbon atoms inside the ordered aromatic region.[22] Hence, as the D band corresponds to the amount of disordered states or defect sites and G band correspond to the amount of ordered states inside CDs, a ratio of peak intensities between these two bands, i.e. I_D/I_G can give an idea to evaluate the extent of defects in it.[23] After fitting these two peaks by Gaussian distribution, we have found the ratio of I_D/I_G is 1.17 revealing considerable amount of defects sites in the as-synthesized CDs.

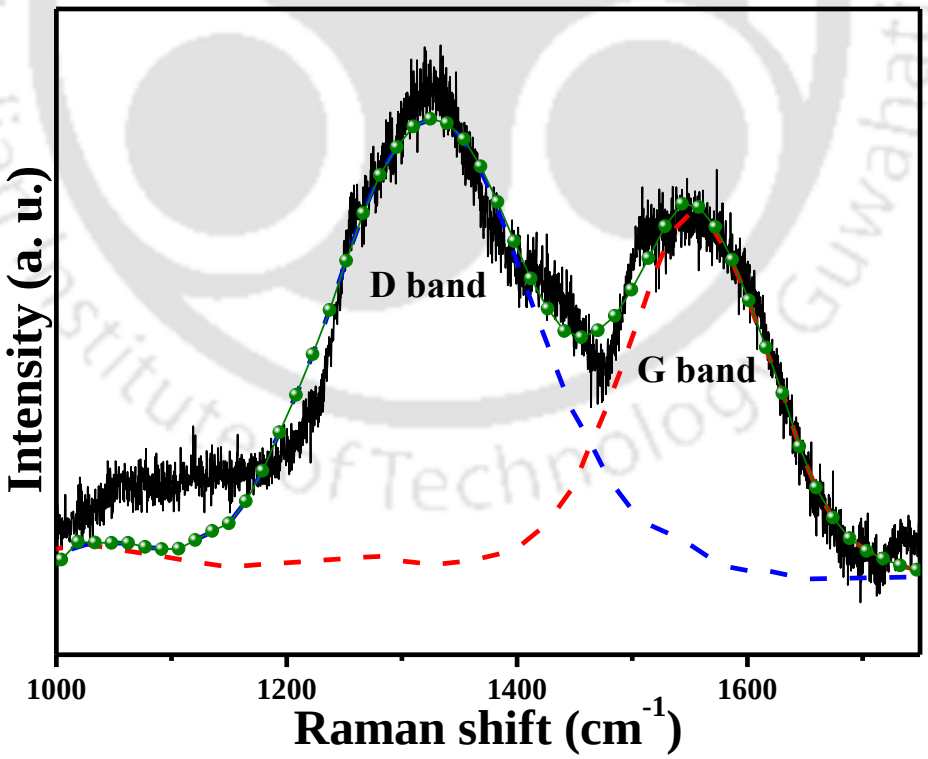

Figure 6.3 Raman spectrum of as-synthesized CDs.

6.3.4 Ultraviolet-visible Absorbance and Photoluminescence Spectra

To investigate the optical absorption profile of CDs, we have analyzed the UV-visible spectrum of the as-synthesized CDs in aqueous solution. From Figure **6.4** it can be seen that the absorption spectrum of CDs consists of three distinct regions, – a strong absorption peak at ~240 nm, another intense strong peak at ~340 nm and a weak and broad band at around 445 nm extended up to 600 nm. The high-energy UV absorption at ~240 nm, less intense peak at 340 nm and the broad band peak extended in the visible region are attributed to the π–π* transition of sp^2 hybridized carbons, n–π* transition of carbon lattice and different surface states of the surface functional groups in the n–π* band gap, respectively.[24, 25] Upon excitation at 340 nm, the aqueous solution shows a strong PL emission peak centered at 460 nm, which indicates that the CDs are fluorescent in nature.

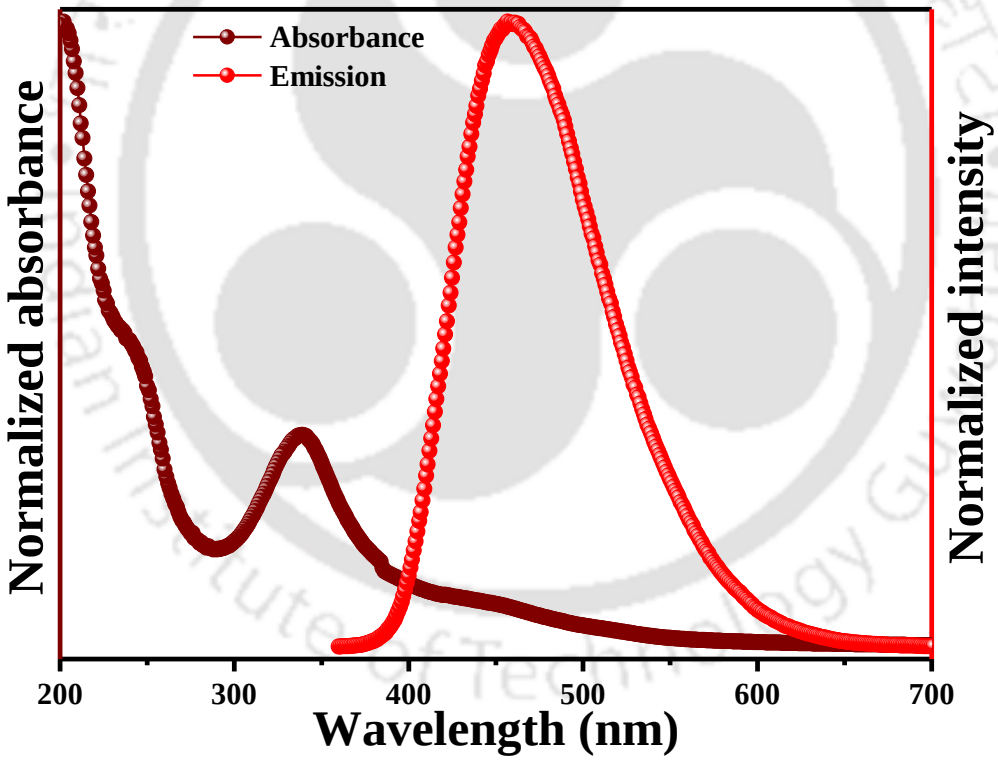

Figure 6.4 Absorbance spectrum and emission spectrum excited at 340 nm wavelength of as-synthesized CDs in aqueous solution.

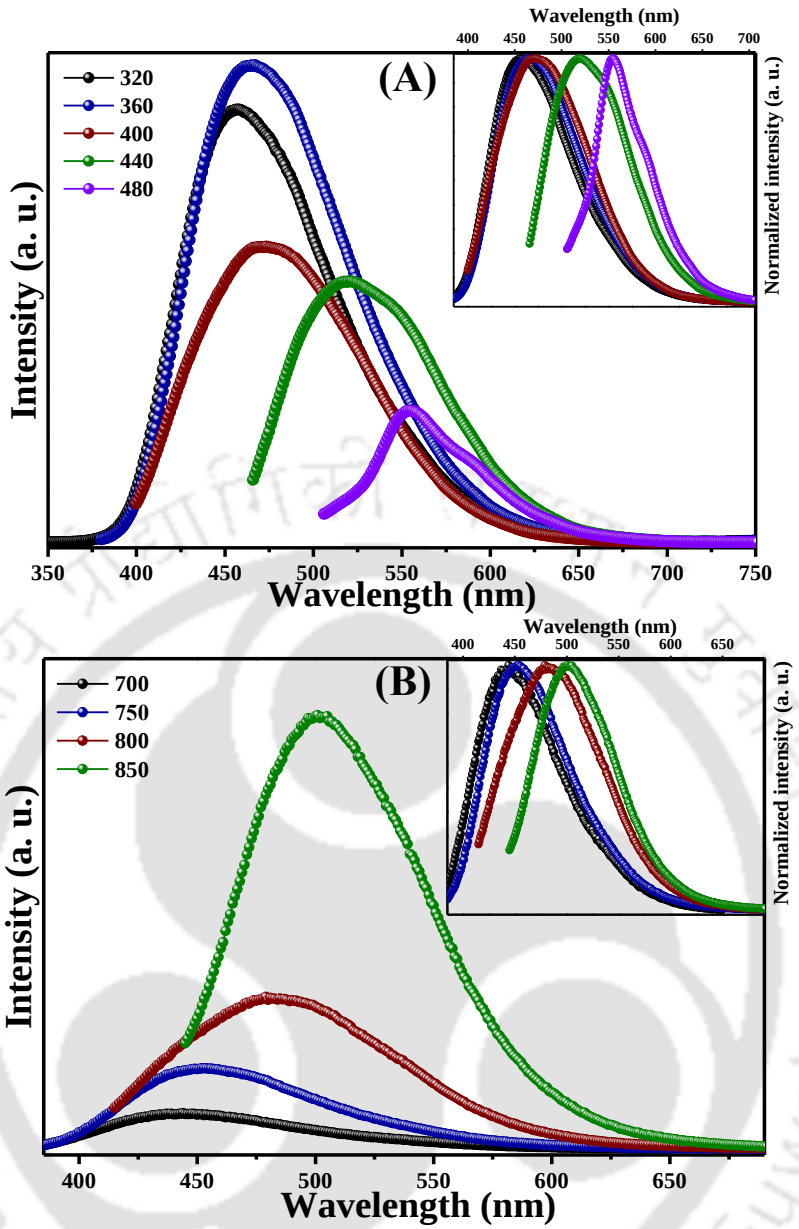

Figure 6.5 (A) Downconversion photoluminescence spectra of CDs with 40 nm increment. Inset to (A) is normalized spectra and (B) Upconversion photoluminescence spectra of CDs with 50 nm increments. Inset to (B) is normalized spectra.

To further investigate the detailed optical properties of the as-synthesized CDs, photoluminescence (PL) studies were performed with variable wavelengths. Figure **6.5(A)** shows the excitation-dependent PL spectra of as-synthesized CDs recorded at different excitation wavelengths (λ_{ex}) with 40 nm increments from 320 nm to 480 nm in water. With the increase in excitation wavelength, the emission maxima progressively shifts towards the longer wavelength and after excitation wavelength exceeds 360 nm, the emission intensity decreases. The reason behind the PL of CDs is not fully understood yet. The excitation wavelength dependent PL of CDs could be due to several reasons, such as different size

distribution, excitons of carbons, emissive traps, free zig-zag sites, the presence of heteroatoms, surface defects etc.[26, 27]

Significantly, apart from strong PL properties, these as-synthesized CDs show remarkable upconversion PL properties. Figure **6.5(B)** shows the PL spectra of CDs when excited by low energy light (700 - 850 nm). It is found that the upconverted emission is located at 445 – 500 nm. Here, this upconversion PL property of CDs could be due to the multiphoton process.[6] Hence, upconversion PL property of as-synthesized CDs could be useful in designing an efficient photocatalyst with a wide band gap material as the coupling of these CDs onto the photocatalyst can utilize a wide spectral range.

6.3.5 Material Morphology and Elemental Analysis

Figure **6.6(A)** shows the Field-emission transmission electron microscopic (FETEM) image of a BZO hollow nanosphere. The contrast difference between dark edge and light core of the BZO sphere proves the hollow nature of the spherical

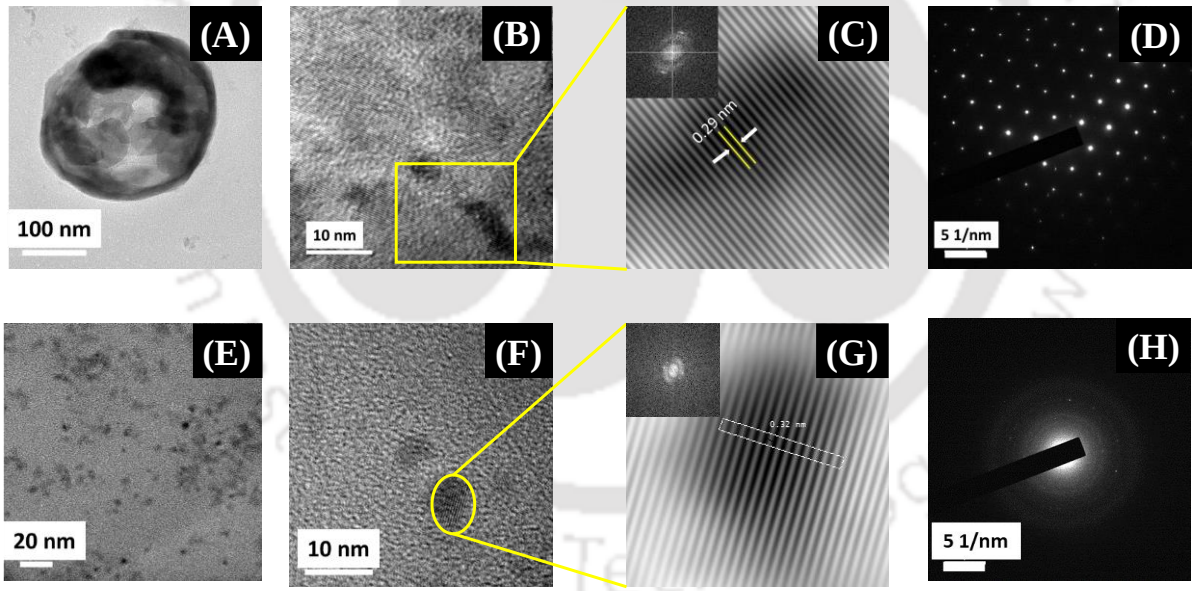

Figure 6.6 FETEM image of (A) BZO hollow nanosphere (B) high-resolution TEM (HRTEM) image of BZO hollow spheres. Inset to (C) is the fast Fourier transformed (FFT) image of the highlighted portion in image (B), (C) shows inverse fast Fourier transformed (IFFT) of the masked FFT shown in the inset to (C). (D) Selected area electron dispersion (SAED) patterns of BZO (E) FETEM image of CDs, (F) HRTEM image of CDs. Inset to (G) is the fast Fourier transformed (FFT) image of the highlighted portion in image (F), (G) shows inverse fast Fourier transformed (IFFT) of the masked FFT shown in the inset to (G) of CDs (H) Selected area electron dispersion (SAED) pattern of CDs.

nanoparticles. In hydrothermal synthesis, under the influence of high alkaline environment, Ostwald ripening process drives the formation of hollow spheres.[17, 28] The formation of hollow structures can be discussed in several different stages, such as hydrolysis, nucleation, and growth process, as reported previously.[29] In the initial stage of the reaction, precursors undergo hydrolysis to form corresponding metal hydroxides in aqueous alkaline condition. With time, the concentration of the metal salts increases owing to more hydrolysis of metal salts and at a particular time and temperature, solution become supersaturated. The reaction between the metal hydroxides in this supersaturated and hot solution favors nucleation and forms tiny particulates by suppressing the grain-growth process. Due to very small size, the particulates have high surface energy and agglomerate under the influence of van der Waals forces to form larger particles with lesser surface energy. This process of agglomeration continues until an electrostatic barrier layer is established.[30] Hence, BZO forms by hydrolysis or decomposition of metal hydroxide monomers in the reaction medium. During the course of the reaction, the dense spheres undergo recrystallization to form crystalline hollow spheres by Ostwald ripening process. In this process, the smaller crystallites from the core of the sphere tend to dissolute more with time and relocate over the larger particles on the surface of the spherical particles. Outward diffusions of the smaller particles from the core of a sphere contribute to the edge thickness, leading to a partial or complete void formation in the core of the sphere.[28] The products are formed in a spherical shape to minimize the surface energy and owing to the high concentration of OH^- ions in the reaction medium.[31] The formation of the BZO products can be explained by following dehydration pathway –

$$[Ba^{2+}(OH)_a^-]^m + [Zr^{4+}(OH)_b^-]^n = BaZrO_3 + 3H_2O$$

The dehydration of the supersaturated solution under high temperature may retain a fraction of OH^- ions and H_2O molecules in their structure and thereby form defective crystals and the dehydration of fraction these retained OH^- ions favors the formation of oxygen vacancies in the lattice of BZO. Figure **6.6(B)** shows the HRTEM image of a selected area of BZO and Figure **6.6(C)** shows the inverse fast Fourier transformed (IFFT) image of the masked FFT shown in the inset to Figure **6.6(C)** of BZO. From the IFFT image, the inter-planar spacing is found to be 0.29 nm corresponding to (110) lattice plane of BZO. SAED pattern of BZO shown in Figure **6.6(D)** proves its single crystalline nature.

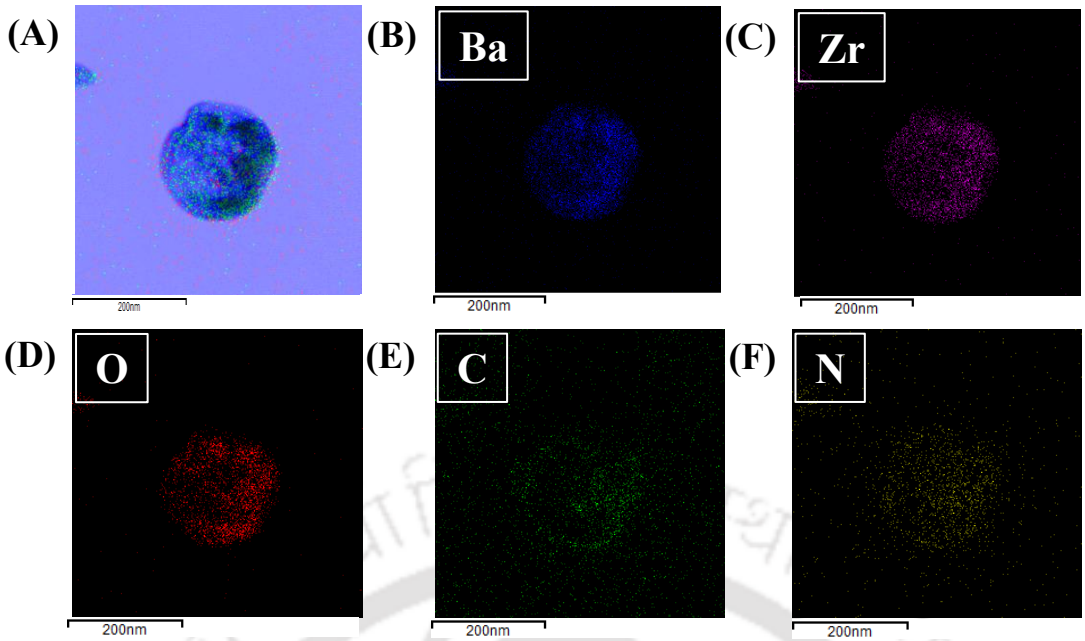

Figure 6.7 (A) Overall mapping in transmission electron microscopic (TEM) images and (B – F) shows the elemental mapping of Ba, Zr, O, C and N elements on a single 3C_BZO hollow nanosphere.

Figure **6.6(E)** shows the FETEM images of as-synthesized carbon dots. Carbon dots are found to be spherical in shape and of 2 – 7 nm in size and dispersed evenly without much significant agglomeration. Figure **6.6(F)** shows the HRTEM image of a single CDs and Figure **6.6(G)** shows the inverse fast Fourier transformed (IFFT) image of the masked FFT shown in the inset to Figure **6.6(G)**. From the IFFT image, the inter-planar spacing is found to be 0.32 nm corresponding to the (002) lattice plane of CDs. The SAED pattern of CDs shown in Figure **6.6(H)** indicates low crystallinity of as-synthesized CDs.

6.3.6 Ultraviolet-visible Diffuse Reflectance Spectra

Among many factors, the efficiency of a photocatalyst is highly dependent upon its ability to absorb light, as the first step is to generate photogenerated charge carriers in a photocatalyst. As shown in Figure **6.8**, the main absorption peak of BZO is at 230 nm, which can be assigned to band-to-band transition. A band tail with an absorption extended beyond 400 nm is observed due to the presence of disordered states or defect states or oxygen vacancies in the compound, as it is known that the impurities or defect state transitions give band tail in absorption spectra in semiconductors.[32] In the *x*C_BZO ($x = 1 – 4$) hybrid nanomaterials, the absorption onset of the compounds is red shifted and the band tail absorption intensity increases in the wavelength range of 350 – 800 nm with progressive increase in CDs amount.

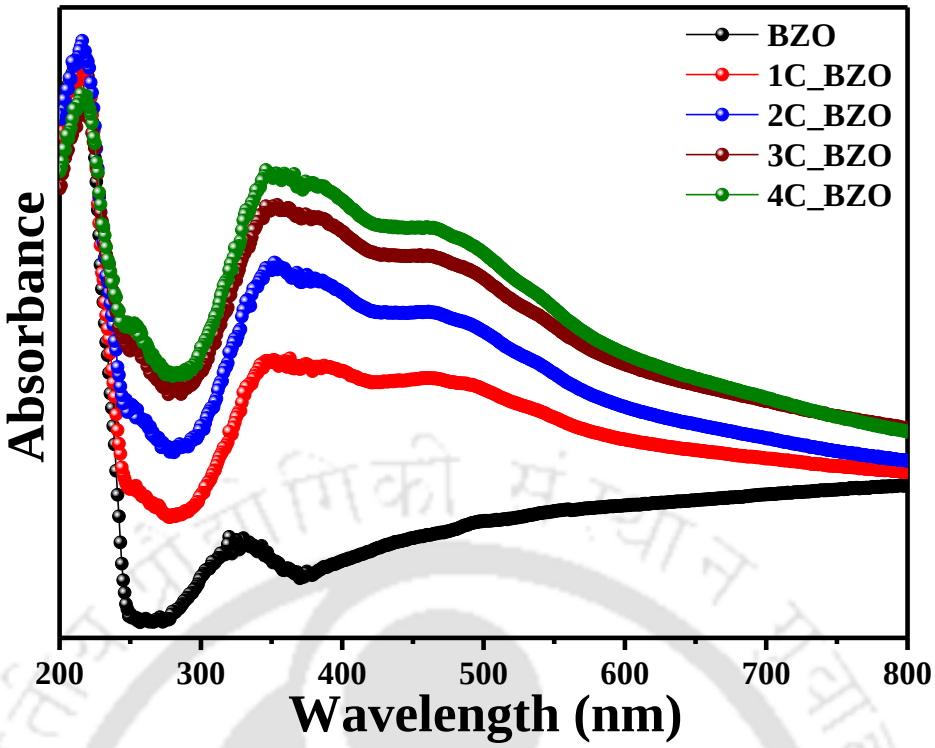

Figure 6.8 UV-visible diffuse reflectance spectra of as-synthesized *x*C_BZO (*x* = 0 – 4) hybrid nanomaterials.

Increased light absorption by a catalyst can increase the population of photogenerated charge carriers, which can in turn increase their photocatalytic efficiency.

6.3.7 X-ray Photoelectron Spectroscopy (XPS) Spectra

Surface properties and the core level electronic structure of the elements for CDs, BZO and 3C_BZO were studied using X-ray photoelectron spectroscopic analysis (XPS). Figure **6.9(A)** depicts the XPS survey spectrum of as-synthesized CDs with three intense peaks at binding energies (B. E.) of 285.6 eV, 400 eV and 531.2 eV corresponding to C 1s, N 1s and O 1s, respectively; indicating that the synthesized products are N-doped CDs. Upon deconvolution of C 1s core level spectra of CDs it could be fitted into three different peaks at B. E. of 284.77 eV, 286.16 eV and 287.83 eV, which are attributed to aliphatic or graphitic (C–C/C=C), oxygenated (C–O/C=O) and nitrous (C–N) carbon atoms, shown in Figure **6.9(B)**.[33]

Figure **6.10(A)** represents the O 1s core level XPS spectra of BZO and 3C_BZO samples. Asymmetric peaks of O 1s spectra of BZO and 3C_BZO upon deconvolution can be fitted into two different peaks at B. E. of 529.3 eV and 531.5 eV for BZO and at B. E. of 529 eV

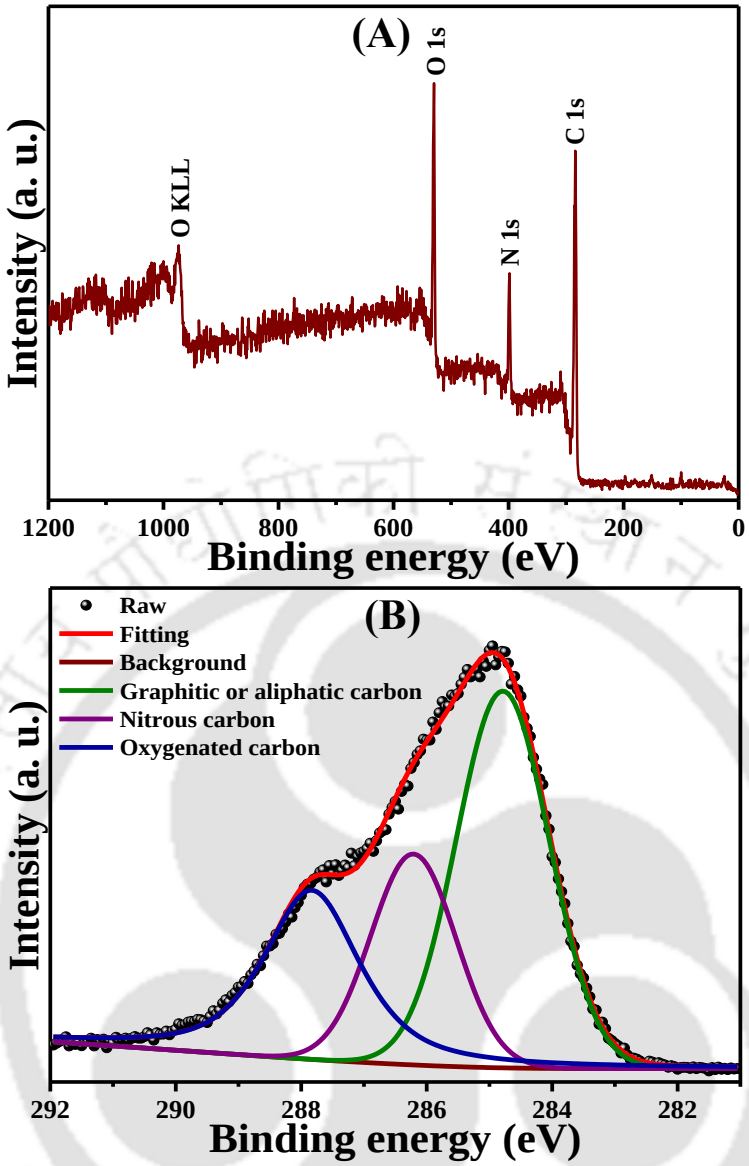

Figure 6.9 (A) XPS survey spectrum and (B) C 1s core level spectrum of as-synthesized CDs.

and 531.2 eV for 3C_BZO. These two O 1s peaks indicate the presence of two surface oxygen species in the compounds. The peak at lower binding energy corresponds to the lattice oxygen ($O_{latt.}$) whereas the peak at higher binding energy is due to surface hydroxyl or oxygen adsorbed on the material surface or organic oxygen moieties ($O_{ads.}$). This ($O_{ads.}$) region is also known to be the signature of oxygen vacancies in a sample.[34] The number of oxygen vacancies in a compound can be evaluated by calculating the relative peak area ratio of $O_{ads.}$ / $O_{latt.}$[34] The value of peak area, relative peak area ratio and peak position of $O_{latt.}$ and $O_{ads.}$ are tabulated in Table **6.1**. From Table **6.1**, we can see that the value of relative peak area ratio of $O_{ads.}$ / $O_{latt.}$ for 3C_BZO is much higher (1.69) than that for BZO (0.92), indicative of increased oxygen vacancies with the incorporation of CDs onto BZO. To get a clear insight on how

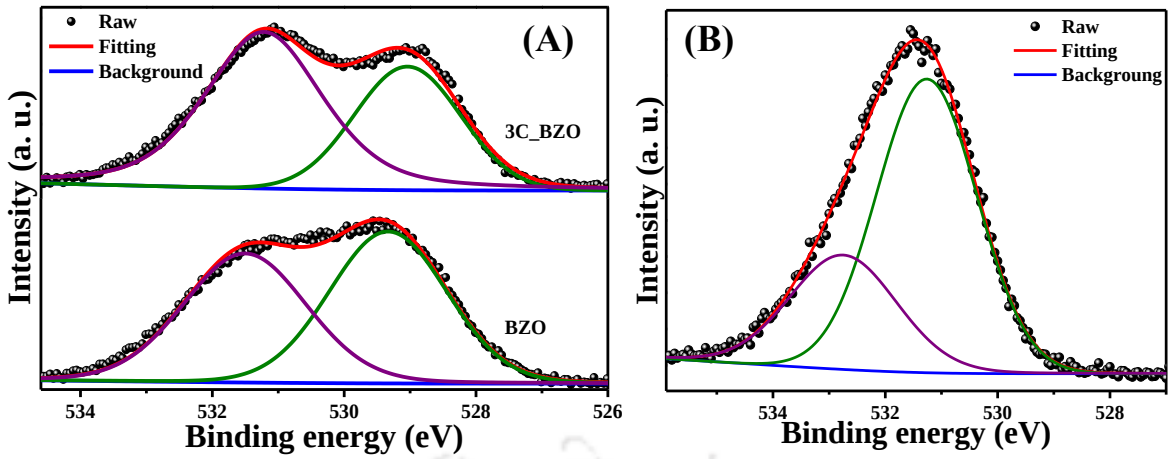

Figure 6.10 O 1s core level XPS spectra of (A) BZO and 3C_BZO, (B) as-synthesized CDs.

CDs increases the number of oxygen vacancies in the hybrid material we have also analysed the O1s core level XPS spectra of CDs. Figure **6.10(B)** shows O1s spectra of CDs, deconvoluted into two asymmetric peaks with a calculated $O_{ads.}$ / $O_{latt.}$ value of 0.58. Hence, it is clear that some of the surface organic groups attached to CDs may also suffer from oxygen vacancies. Incorporation of CDs onto BZO nanospheres thus increases the amount of oxygen vacancies in the hybrid nanomaterials. This phenomenon explains the reason behind an increase in the intensity of the band tail absorption peak of hybrid compounds, as seen in Figure **6.8**.

Table 6.1 Peak position, peak area and relative peak area ratio ($O_{ads.}$ / $O_{latt.}$) of O1s core level XPS spectra for BZO and 3C_BZO hybrid nanomaterials.

Compound	Peaks	Peak position (eV)	Peak area	$O_{ads.}$ / $O_{latt.}$
BZO	$O_{latt.}$	529.33	3089	0.92
	$O_{ads.}$	531.5	2826	
3C_BZO	$O_{latt.}$	529	2352	1.69
	$O_{ads.}$	531.22	3966	

The oxidation state of Ba and Zr have been assessed from Ba 3d and Zr 3d core level spectra of BZO and 3C_BZO. In Figure **6.11(A)**, Ba 3d core level XPS spectra of BZO appears at B. E. of 779.5 eV and 794.8 eV, corresponding to Ba $3d_{5/2}$ and Ba $3d_{3/2}$, respectively. In case of 3C_BZO, Ba 3d core level XPS spectra for Ba $3d_{5/2}$ and Ba $3d_{3/2}$ appears at B. E. of 779.4eV and 794.7 eV, respectively. Difference in binding energy between the two peaks (Δ B. E.) of Ba 3d core level XPS spectra for both the compounds is found to be ~15.3 eV indicating that Ba is present in (+2) oxidation state in both the compounds .[35] The asymmetric Zr 3d core level XPS spectra of BZO and 3C_BZO is depicted in Figure **6.11(B)**. Upon deconvolution,

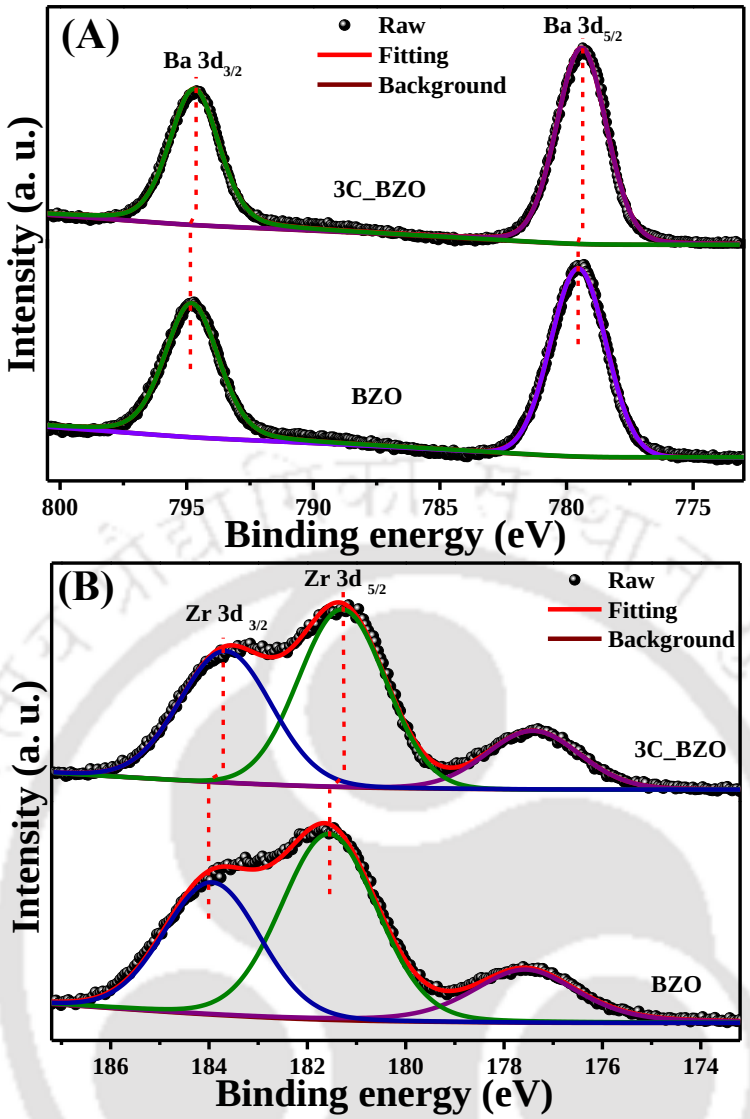

Figure 6.11 (A) Ba 3d core level XPS spectra and (B) Zr 3d core level XPS spectra of BZO and 3C_ BZO hybrid nanomaterials.

we observe three different peaks at B. E. of 177.57 eV, 181.56 eV and 183.93 eV for BZO and at B. E. of 177.21 eV, 181.09 eV and 183.46 eV for 3C_BZO corresponding to Ba $4p_{3/2}$, Zr $3d_{5/2}$ and Zr $3d_{3/2}$ respectively.[35, 36] Binding energy difference (ΔB. E.) between the two peaks of Zr 3d core level XPS spectra for both the compounds is found to be ~2.37 eV which proves (+4) oxidation state of Zr in both the compounds. An energy shift in XPS binding energy in CDs modified BZO hybrid nanoparticles is observed, indicative of a strong electronic interaction between CDs and BZO. XPS valence band spectra of BZO and 3C_BZO hybrid nanomaterials are shown in Figure **6.12**. From Figure **6.12** it is clear that both the spectra have identical valence band edge with a clear band tail. From preceding reports, we know that in

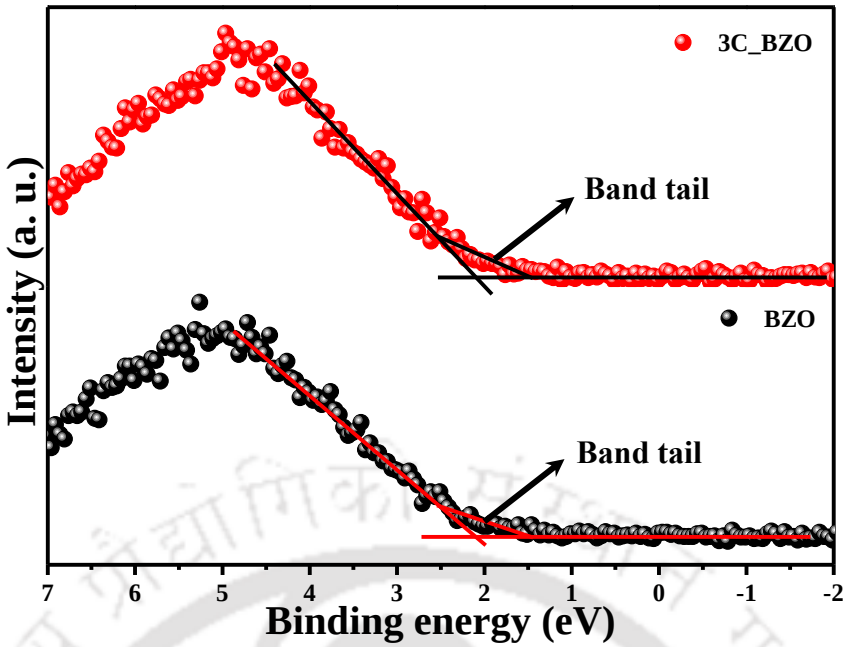

Figure 6.12 XPS valence band spectra of BZO and 3C_ BZO hybrid nanomaterials.

any compound this band tail in valence band spectra signifies the presence of lattice disorder.[37] With incorporation of CDs onto BZO, we could not notice any shift in the valence band position of 3C_BZO. So the enhancement in light absorption in *x*C_BZO hybrid nanomaterials could be explained by the effective electronic transition due to the presence of mid-gap states or disordered states and upconversion photoluminescence of CDs.

6.3.8 Electron Spin Resonance (ESR) Spectra

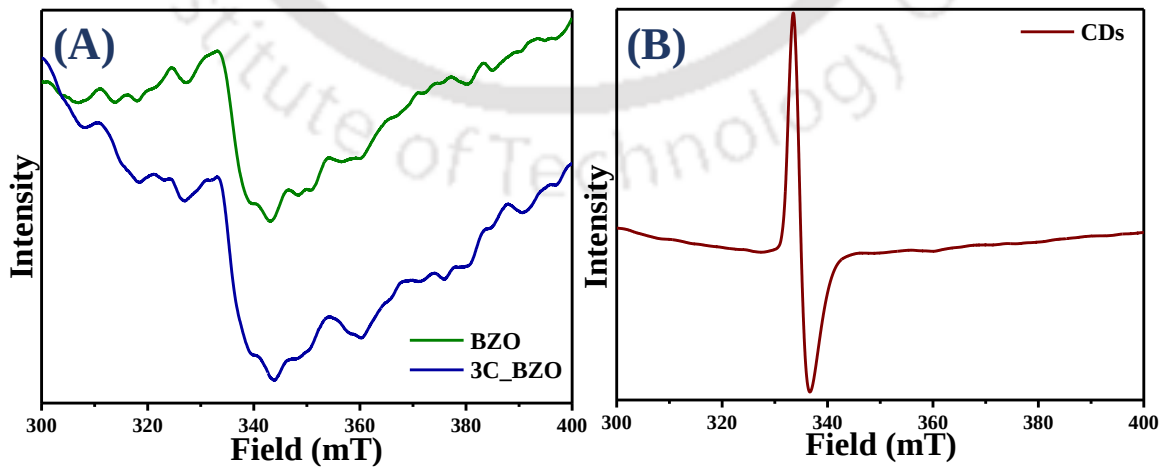

Figure 6.13 ESR spectra of (A) BZO hollow spheres and 3C_BZO hybrid nanomaterials and (B) as-synthesized CDs at room temperature.

In our studied systems, oxygen vacancy is an important parameter proposed for controlling photocatalytic activity; hence, it is significant to understand the nature of oxygen vacancies that are present in BZO and CDs incorporated hybrid nanomaterials. From literature, it is known that three different types of oxygen vacancies such as neutral, singly ionized and doubly ionized can be present in a compound. Among these vacancies, the number of trapped electrons present are two, one and zero in neutral, singly ionized and doubly ionized oxygen vacancies respectively.[38] Owing to their different spin states, ESR technique could be employed to determine the nature of the oxygen species in these compounds. Among these three different types of oxygen vacancies, singly ionized oxygen vacancy gives a strong ESR signal as it has only one unpaired electron, and neutral oxygen vacancy with two unpaired electrons gives a triplet in ESR analysis. If the neutral oxygen vacancy has paired electrons, then it cannot give any ESR signal. From Figure **6.13(A)**, we observe that the BZO and 3C_BZO show a broad peak at around g − tensor value of 2.005, which is due to singly ionized paramagnetic oxygen vacancies ($V_O^{\bullet}$).[39] Figure **6.13(B)** shows the ESR spectra of as-synthesized CDs in room temperature and it shows an intense ESR signal at g tensor value of 2.005. As seen from FTIR and Raman analysis, CDs have nitrous groups and surface defects on it. Hence, the origin of its ESR spectra may be due to the presence of unpaired electrons in surface defects and nitrous groups. Hence, from the UV-visible DRS study, XPS analysis and ESR study we can say that all the studied compounds have a certain amount of oxygen vacancies and disordered states in their structures, which could be beneficial for their photocatalytic activities.

6.3.9 Photoluminescence (PL) and Time–resolved Photoluminescence (TRPL) Spectra

To observe the charge transfer and charge recombination processes in a photocatalyst, photoluminescence (PL) spectra has been widely used. It is notable from the PL spectra shown in Figure **6.14(A)** that upon excitation at 256 nm, both BZO and 3C_BZO hybrid nanomaterials emit at 396 nm. Bare BZO has high PL intensity which attributes to the lattice disorder and trap states in BZO.[40] In 3C_BZO, the PL intensity at 396 nm drops significantly. This phenomenon could be due to reduction in photogenerated electron–hole recombination. On introduction of CDs onto BZO, the photogenerated electrons in the conduction band of BZO move efficiently to the CDs particles as CDs are excellent charge carriers thereby preventing its recombination with the photogenerated holes present in the valence band of BZO.[4] Hence owing to efficient charge transfer, in the hybrid nanomaterials a sharp drop in

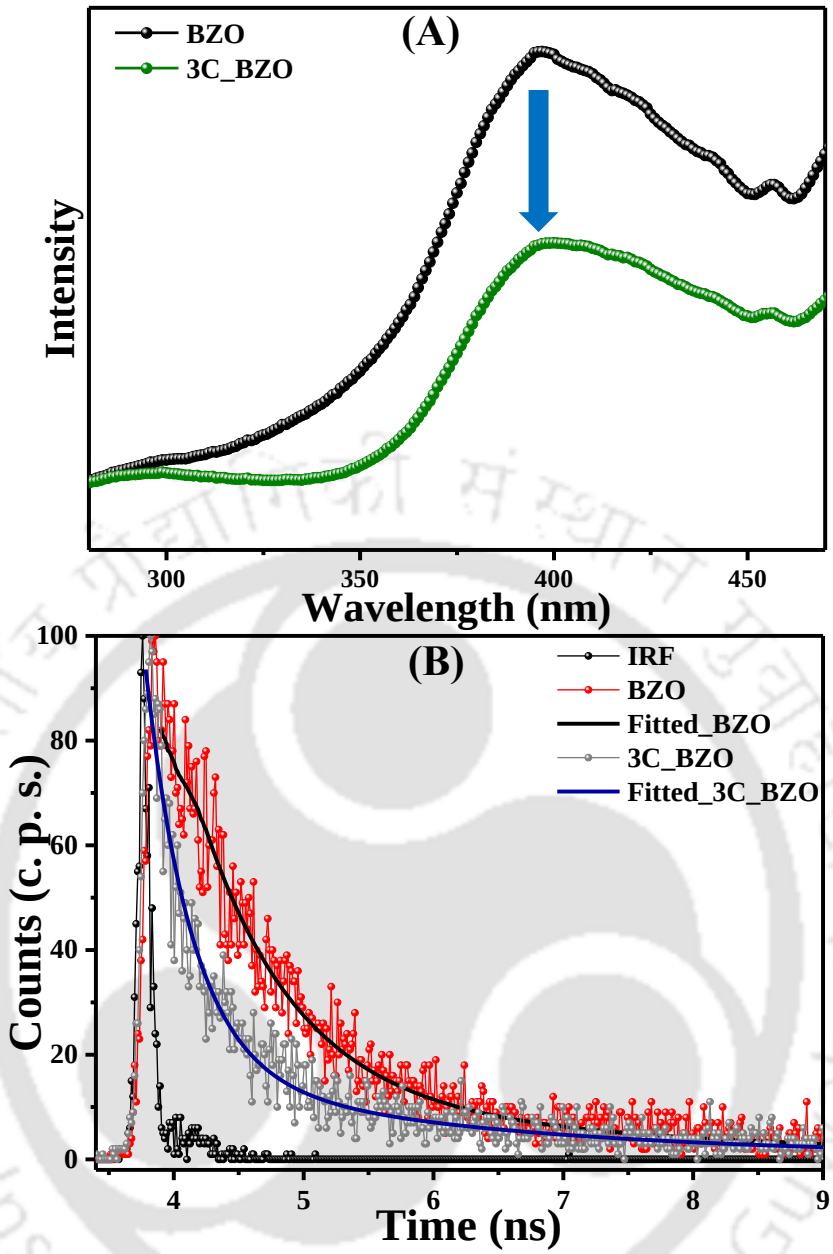

Figure 6.14 (A) Steady state photoluminescence at an excitation of 256 nm and (B) time-resolved photoluminescence spectra of BZO and 3C_ BZO hybrid nanomaterials at an excitation of 375 nm and emission observed at 450 nm.

photoluminescence proves decreased recombination, which can in turn enhance its photocatalytic activity.

Time-resolved photoluminescence (TRPL) spectroscopic analysis was performed to further get an insight of the charge transfer process between BZO and CDs in the best performing 3C_BZO catalyst. For comparison, TRPL was also performed for BZO. The samples were excited at a wavelength of 375 nm and the emission observed at 450 nm and shown in Figure **6.14(B)**. PL decay profiles are fitted with a bi-exponential function to calculate the exciton

lifetime, ⟨τ⟩. The decay profile exhibit bi-exponential decay patterns, which infer to multiple processes involved during the decay of emissive excitons or the radiative transitions. The fitting parameters (χ^2) and detailed spectroscopic results, exciton lifetimes (τ_1, τ_2), pre-exponential factors (α_1, α_2) and average exciton lifetimes (<τ>) are summarized in Table **6.2**.

Table 6.2 Fitting parameter (χ^2), initial intensity (α_1, α_2), excited-state lifetime (τ_1, τ_2), and average exciton lifetime (⟨τ⟩ ns) for CDs, BZO and 3C_BZO hybrid nanomaterials.

Compound	α_1	α_2	τ_1	τ_2	$<\tau>$	χ^2
CDs	0.1082	0.0051	0.752	4.831	1.700	0.921
BZO	0.1038	0.0126	0.732	3.445	1.718	0.951
3C_BZO	79.2237	16.5278	0.355	2.323	1.490	0.908

The average lifetime of the compounds were calculated by using the following equation[41]

$$<\tau> = \frac{(\alpha_1 \times \tau_1^2 + \alpha_2 \times \tau_2^2)}{(\alpha_1 \times \tau_1 + \alpha_2 \times \tau_2)}$$

From the average lifetime values, a decrease in average exciton lifetimes for 3C_BZO is observed compared to BZO. Exciton lifetime for 3C_BZO (1.49 ns) is found to be lower than that of bare BZO (1.72 ns), indicating that the photogenerated electrons in the conduction band of BZO transfer efficiently to the CDs. Faster average PL lifetime proves a strong excited state electronic interaction and facile charge transport from BZO to CDs in the hybrid nanomaterials.[42]

6.3.10. Photocatalytic Hydrogen Production

Photocatalytic H_2 evolution from water by *x*C_BZO (*x* = 0 – 4) hybrid nanomaterials under UV-visible light were analyzed in the presence of 0.25 M Na_2SO_3/0.35 M Na_2S mixture as sacrificial hole scavenger and shown in Figure **6.15**. In bare BZO, the valence band maxima and the conduction band minima are more positive than the H_2O/O_2 redox potential and more negative than the H_2/H^+ redox potential, respectively.[8] In photocatalytic H_2 evolution reaction, a sacrificial reagent can enhance the catalytic efficiency of a photocatalyst as the sacrificial reagent can trap the photogenerated holes of the semiconductor and leave the photogenerated electrons in the conduction band, which in turn decreases the charge carrier recombination and thus boosts the charge separation.[43, 44] The role of sacrificial reagent (0.25 M Na_2SO_3/0.35 M Na_2S) in the photocatalytic H_2 production can be explained by the following equations[44] –

$$\text{Photocatalyt} + \text{light} \rightarrow h^+_{VB} + e^-_{CB} \quad (1)$$

$$2H_2O + 2e^-_{CB} \rightarrow H_2 + 2OH^- \quad (2)$$

$$SO_3^{2-} + 2h^+_{VB} + 2OH^- \rightarrow SO_4^{2-} + 2h^+ \quad (3)$$

$$2S^{2-} + 2h^+_{VB} \rightarrow S_2^{2-} \quad (4)$$

$$S_2^{2-} + SO_3^{2-} \rightarrow S_2O_3^{2-} + S^{2-} \quad (5)$$

$$SO_3^{2-} + S^{2-} + 2h^+_{VB} \rightarrow S_2O_3^{2-} \quad (6)$$

When the semiconductor is photo excited by a light with energy more or equal to its band gap energy, electrons are excited to the conduction band leaving an equivalent number of holes in the valence band as shown in equation 1. With high lifetime and charge mobility, these photogenerated charge carriers may reach the surface of the semiconductor where they can undergo redox reactions with the reactants adsorbed onto the semiconductor surface. As shown in equation 2, electrons can produce H_2 by reducing water. While the holes can produce S_2^{2-} and SO_4^{2-} ions by oxidizing the sacrificial ions, $S^{2-}$and SO_3^{2-}, respectively (equations 3 & 4). As described in equation 5, S^{2-} ions form optically transparent $S_2O_3^{2-}$ions by reacting with SO_3^{2-} ions in solution. In this process, colourless $S_2O_3^{2-}$ ions are formed by the reaction of S^{2-} and SO_3^{2-} ions with photogenerated holes, as described in equation 6.

In the present work, the amount of H_2 gas produced by as-synthesized BZO is 290 µmol per hour per gram. Compared to bare BZO, the CDs modified photocatalysts exhibit superior catalytic activity, inferring the vital role of CDs in BZO. The improved H_2 production efficacy can be attributed to the enhanced light absorption of the catalysts in the visible light regime after CDs loading and faster charge transfer to CDs. From Figure **6.15** we note that 3 wt% is the optimal CDs loading concentration for the highest amount of H_2 gas evolution (670 µmol/h/g), whereas, 1C_BZO, 2C_BZO, and 4C_BZO produces 385 µmol/h/g, 480 µmol/h/g and 405 µmol/h/g of H_2 gas respectively. The calculated AQY of BZO and 3C_BZO is ~2% and ~4%, respectively. It is observed that beyond 3 wt% CDs loading, the H_2 gas production efficacy decreases. This could be due to the presence of surplus CDs on the surface of BZO, which can effectively block the active sites for photogenerated charge carriers to react with surface adsorbed species.[45] These excess CDs then act as charge carrier recombination centers which reduce the photocatalytic efficiency of BZO. Thus, 3 wt% of CDs loading on BZO is optimal for efficient photocatalytic activity.

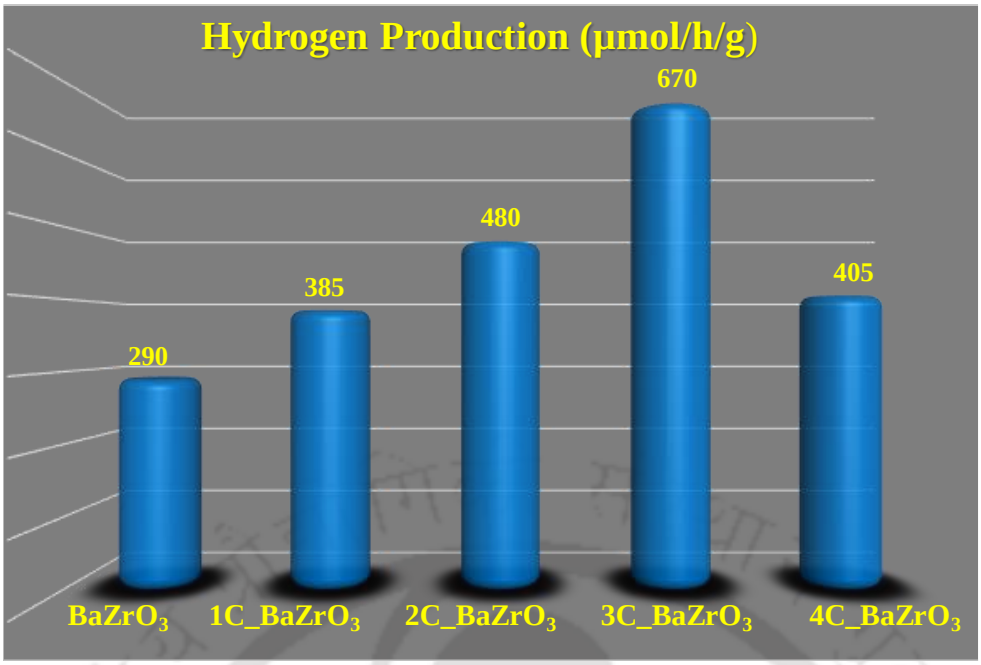

Figure 6.15 Rate of photocatalytic H_2 production from *x*C_BZO (*x* = 0 – 4) hybrid nanomaterials under UV-visible light irradiation with 0.25 M Na_2SO_3/0.35 M Na_2S mixture as sacrificial reagent.

6.3.11 Photocatalytic Dye Degradation

Besides hydrogen production, *x*C_BZO (*x* = 0 – 4) hybrid nanomaterials also show effectiveness in degrading organic dyes commonly found in industrial waste water. Here, to examine the degradation efficiency we have chosen methylene blue as the model system. Figure **6.16(A)** shows MB dye degradation of best performing hybrid catalyst 3C_BZO at p^H 13. Monitoring the peak at 664 nm of MB, intensity of the peak got supressed with time and within 1 h the intensity reduced to more than 90%. Degradation efficiency of the catalysts was evaluated by comparing the initial concentration of the dye (C_0) with the final concentration (C) of the dye. Figure **6.16(B)** shows the degradation efficiency of *x*C_BZO (*x* = 0 – 4) hybrid nanomaterials. It has been found that 3C_BZO has highest degradation efficiency of ~90% whereas degradation efficiency of BZO, 1C_BZO, 2C_BZO, and 4C_BZO are ~78%, ~85%, ~89% and ~80%, respectively. The enhancement in dye degradation efficiency of *x*C_BZO hybrids compared to bare BZO could be owing to the enhanced light absorptivity and superior charge transfer ability of the carbon dots.

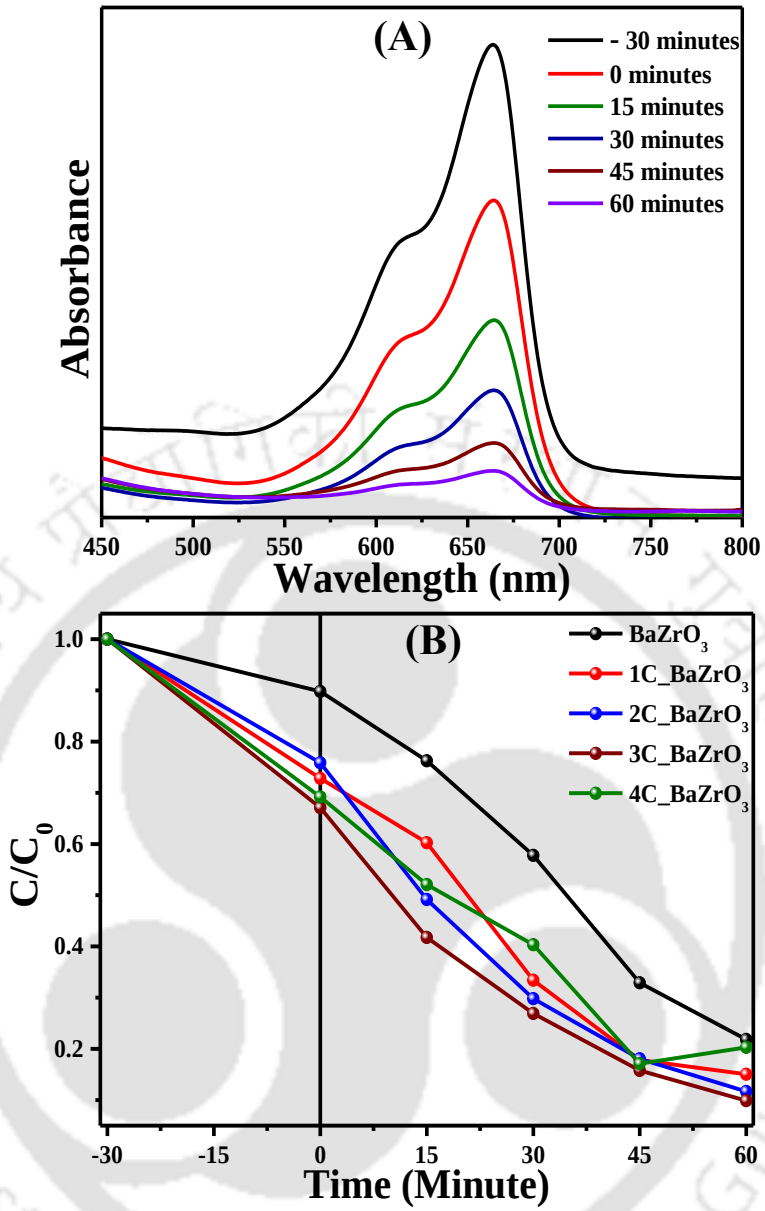

Figure 6.16 (A) Chronological absorption spectral patterns of methylene blue dye over 1 h during the photodegradation process in the presence of 3C_BZO under UV-Visible light and (B) plot of (C/C_0) with respect to time (minute) for BZO, and *x*C_BZO (x = 1 – 4) hybrid nanomaterials.

6.4 CONCLUSIONS

In summary, we have synthesized $BaZrO_3$ and carbon dots by facile hydrothermal synthesis. 1 – 4 wt% of C_BZO hybrid catalysts are synthesized by dispersing CDs and BZO together. The synthesized products are found to be the efficient catalyst for photocatalytic H_2 production and methylene blue dye degradation. Synthesized samples were analyzed with the help of several analytical techniques and found that presence of defect states, oxygen

vacancies and the addition of CDs onto BZO leads to an increment of visible light absorption by the photocatalysts and owing to the high charge transfer rate of CDs, the photogenerated charge carrier recombination is reduced. We have observed that 3 wt% CDs loaded onto BZO shows the highest efficiency in both photocatalytic H_2 production and MB dye degradation. The AQY of 3C_BZO (~4%) is doubled than that of the BZO (~2%). In brief, this work proves that CDs can considerably enhance the photocatalytic activity of a wide band gap material such as BZO that provides a facile scheme to develop hybrid materials that could be utilized in energy harvesting and environmental renovation.

6.5 REFERENCES

1. Yeh, T.; Teng, C.; Chen, S.; Teng, H. *Adv. Mater.***2014**, *26*, 3297.
2. Liu, J.; Liu, Y.; Liu, N.; Han, Y.; Zhang, X.; Huang, H.; Lifshitz, Y.; Lee, S.; Zhong, J.; Kang, Z. *Science*, **2015**, *347*, 970.
3. Martindale, B. C. M.; Hutton, G. A. M.; Caputo, C. A.; Reisner, E. *J. Am. Chem. Soc.* **2015**, *127*, 6018.
4. Mirtchev, P.; Henderson, E. J.; Soheilnia, N.; Yip, C. M.; Ozin, G. A. *J. Mater. Chem.* **2012**, *22*, 1265.
5. Liu, C.; Chang, K.; Guo, W.; Li, H.; Shen, L.; Chen, W.; Yan, D. *Appl. Phys. Lett.* **2014**, *105*, 073306.
6. Cao, L.; Wang, X.; Meziani, M. J.; Lu, F.; Wang, H.; Luo, P. G.; Lin, Y.; Harruff, B. A.; Veca, L. M.; Murray, D.; Xie, S.; Sun, Y. *J. Am. Chem. Soc.* **2007**, *129*, 11318.
7. Wang, Y.; Hu, A. *J. Mater. Chem. C* **2014**, *2*, 6921.
8. Liu, J.; Liu, X.; Luo, H.; Gao, Y. *RSC Adv.* **2014**, *4*, 7648.
9. Li, H.; Kang, Z.; Liu, Y.; Lee, S. *J. Mater. Chem.* **2012**, *22*, 24230.
10. Guo, Y.; Yao, P.; Zhu, D.; Gu, C. *J. Mater. Chem. A* **2015**, *3*, 13189.
11. Xu, X.; Bao, Z.; Zhou, G.; Zeng, H.; Hu, J. *ACS Appl. Mater. Interfaces* **2016**, *8*, 14118.
12. Yu, H.; Zhao, Y.; Zhou, C.; Shang, L.; Peng, Y.; Cao, Y.; Wu, L.; Tung, C.; Zhang, T. *J. Mater. Chem. A* **2014**, *2*, 3344.
13. Song, B.; Wang, T.; Sun, H.; Shao, Q.; Zhao, J.; Song, K.; Hao, L.; Wang, L.; Guo, Z. *Dalton Trans.* **2017**, *46*, 15769.
14. Wang, Q.; Huang, J.; Sun, H.; Zhang, K.; Lai, Y. *Nanoscale* **2017**, *9*, 16046.
15. Tang, D.; Zhang, H.; Huang, H.; Liu, R.; Han, Y.; Liu, Y.; Tong, C.; Kang, Z. *Dalton Trans.* **2013**, *42*, 6285.
16. Zhu, S.; Meng, Q.; Wang, L.; Zhang, J.; Song, Y.; Jin, H.; Zhang, K.; Sun, H.; Wang, H.; Yang, B. *Angew. Chem. Int. Ed.* **2013**, *52*, 3953.

17. Dong, Z.; Ye, T.; Zhao, Y.; Yu, J.; Wang, F.; Zhang, L.; Wang, X.; Guo, S. *J. Mater. Chem.* **2011**, *21*, 5978.
18. Das, A.; Gude, V.; Roy, D.; Chatterjee, T.; De, C. K.; Mandal, P. K. *J. Phys. Chem. C* **2017**, *121*, 9634.
19. Zhang, Y.-Q.; Ma, D.-K.; Zhang, Y.-G.; Chen, W.; Huang, S.-M. *Nano Energy* **2013**, *2*, 545.
20. Peng, J.; Gao, W.; Gupta, B. K.; Liu, Z.; Romero-aburto, R.; Ge, L.; Song, L.; Alemany, L. B.; Zhan, X.; Gao, G.; Vithayathil, S. A.; Kaipparettu, B. A.; Marti, A. A.; Hayashi, T.; Zhu, J.; Ajayan, P. M. *Nano Lett.* **2012**, *12*, 844.
21. Ding, H.; Yu, S.; Wei, J.; Xiong, H. *ACS Nano*, **2016**, *10*, 484.
22. Bhattacharyya, S.; Ehrat, F.; Urban, P.; Döblinger, M.; Feldmann, J.; Urban, A. S.; Teves, R.; Wyrwich, R.; Stolarczyk, J. K. *Nat. Commun.* **2017**, *13*, 1.
23. Zheng, F.; Yang, Y.; Chen, Q. *Nat. Commun.* **2014**, *5*, 1.
24. Reckmeier, C. J.; Wang, Y.; Zboril, R.; Rogach, A. L. *J. Phys. Chem. C* **2016**, *120*, 10591.
25. Schneider, J.; Reckmeier, C. J.; Xiong, Y.; Seckendor, M. von; Susha, A. S.; Rogach, A. L. *J. Phys. Chem. C* **2017**, *121*, 2014.
26. Bandi, R.; Gangapuram, B. R.; Dadigala, R.; Eslavath, R.; Singh, S. S.; Guttena, V. *RSC Adv.* **2016**, *6*, 28633.
27. Zong, J.; Zhu, Y.; Yang, X.; Shen, J.; Li, C. *Chem. Commun*. **2011**, *47*, 764.
28. Zou, Y.; Luo, Y.; Wen, N.; Ye, T.; Xu, C.; Yu, J.; Wang, F.; Li, G.; Zhao, Y. *New J. Chem.* **2014**, *38*, 2548.
29. Ye, T.; Dong, Z.; Zhao, Y.; Yu, J.; Wang, F.; Guo, S.; Zou, Y. *Langmuir* **2011**, *27*, 8878.
30. Brinker, C. J.; Scherer, G. W. Sol-Gel Science: The Physics and Chemistry of Sol-Gel Processing. Academic Press, San Diego, CA 1990. p 462.
31. Moreira, M. L.; Longo, V. M.; Avansi, W.; Ferrer, M. M.; Andrés, J.; Mastelaro, V. R.; Varela, J. A.; Longo, É. *J. Phys. Chem. C* **2012**, *116*, 24792.
32. Zhang, J.; Liu, S.; Yu, J.; Jaroniec, M. A *J. Mater. Chem.* **2011**, *21*, 14655.
33. Liu, S.; Tian, J.; Wang, L.; Zhang, Y.; Qin, X.; Luo, Y.; Asiri, A. M.; Al-Youbi, A. O.; Sun, X. *Adv. Mater.* **2012**, *24,* 2037.
34. Jaiswar, S.; Mandal, K. D. *J. Phys. Chem. C* **2017**, *121*, 19586.
35. Wagner, D.; Muilenberg, G. E. *Handbook of X - ray Photoelectron Spectroscopy: A Reference Book of Standard Data for Use in X-ray Photoelectron Spectroscopy, Physical Electronics Division, Perkin-Elmer Corp., 1979*.
36. Sun, W.; Shi, Z.; Liu, M.; Bi, L.; Liu, W. *Adv. Funct. Mater.* **2014**, 24, 5695.
37. Naldoni, A.; Allieta, M.; Santangelo, S.; Marelli, M.; Fabbri, F.; Cappelli, S.; Bianchi, C. L.; Psaro, R.; Dal Santo, V. *J. Am. Chem. Soc.* **2012**, *134*, 7600.
38. Sanyal, K.; Pathak, N.; Yadav, A. K.; Kanrar, B.; Kadam, R. M.; Jha, S. N.; Bhattacharya, D.; Misra, N. L. *Dalton Trans.* **2016**, *45*, 7650.

39. Matta, J.; Lamonier, J. F.; Abi-Aad, E.; Zhilinskaya, E. A.; Aboukaïs, A. *Phys. Chem. Chem. Phys.* **1999**, *1*, 4975.
40. Moreira, M. L.; Buzolin, P. G. C.; Longo, V. M.; Nicoleti, N. H.; Sambrano, J. R.; Li, M. S.; Varela, J. A.; Longo, E. *J. Phys. Chem. A* **2011**, *115*, 4482.
41. Zhang, Y.; Tang, Y.; Liu, X.; Dong, Z.; Hng, H. H.; Chen, Z.; Sum, T. C.; Chen, X. *Small* **2013**, *9*, 996.
42. Wang, X.; Liow, C.; Bisht, A.; Liu, X.; Sum, T. C.; Chen, X.; Li, S. *Adv. Mater.* **2015**, *27*, 2207.
43. Gogoi, G.; Arora, S.; Vinothkumar, N.; De, M.; Qureshi, M. *RSC Adv.* **2015**, *5*, 40475.
44. Bao, N.; Shen, L.; Takata, T.; Domen, K. *Chem. Mater.* **2008**, *20*, 110.
45. Zhang, Z.; Lin, S.; Li, X.; Li, H.; Cui, W. *RSC Adv.* **2017**, *7*, 56335.

Chapter 7

THESIS OVERVIEW AND FUTURE SCOPE

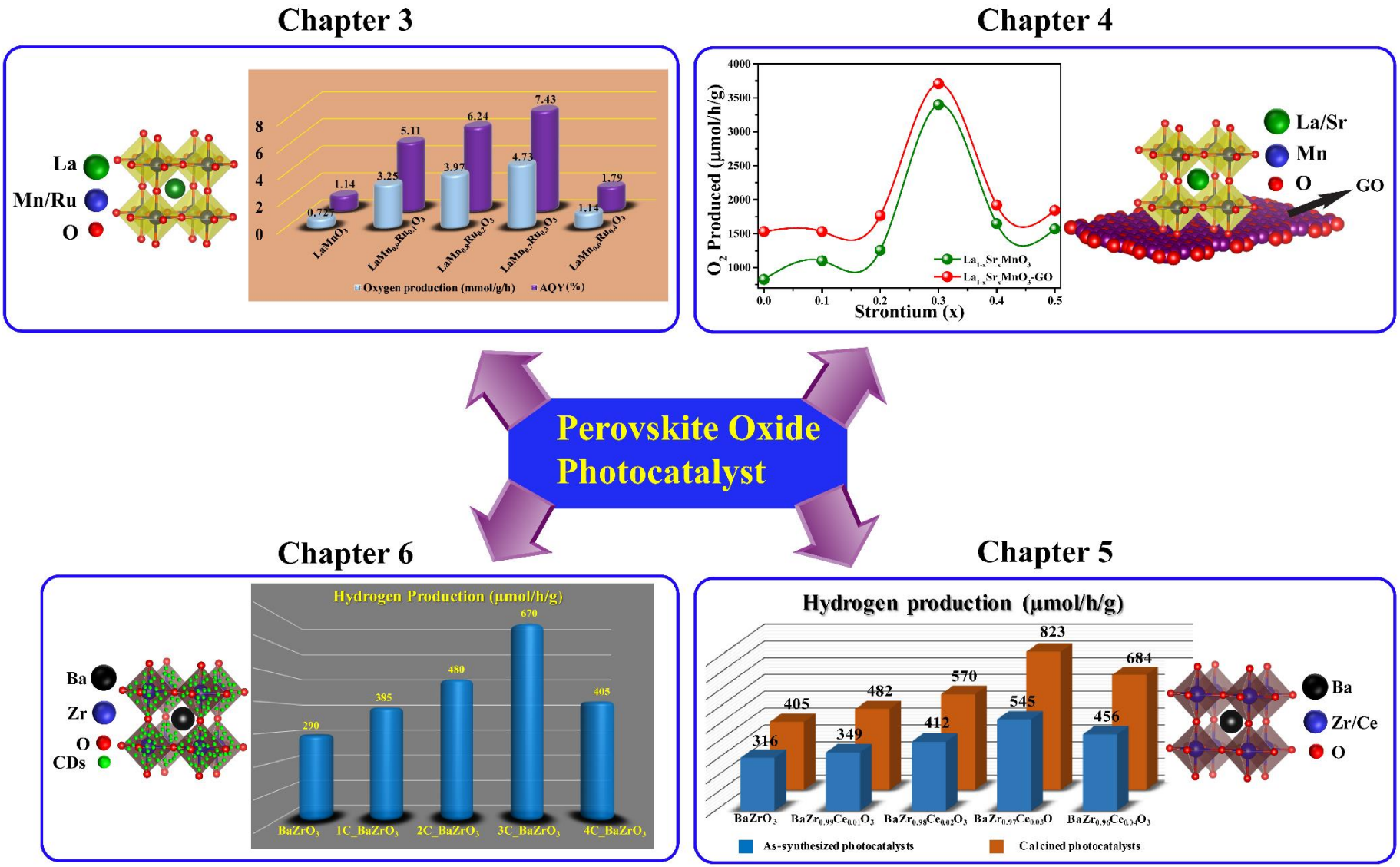
Chapter 3
La
Mn/Ru
O
Oxygen production (mmol/g/h)
AQY(%)
Chapter 4
O2 Produced (μmol/h/g)
Strontium (x)
La/Sr
Mn
O
GO
Perovskite Oxide Photocatalyst
Chapter 6
Ba
Zr
O
CDs
Hydrogen Production (μmol/h/g)
Chapter 5
Hydrogen production (μmol/h/g)
Ba
Zr/Ce
O
As-synthesized photocatalysts
Calcined photocatalysts

Overall Summary and Salient Features of the Thesis:

The present thesis describes a number of new prospects related to environmentally benign energy harvesting from photocatalytic water oxidation/reduction process and water remediation by industrial dye degradation. First part of this chapter recaps the complete conclusions drawn from the research works presented in this thesis and the second part of this chapter is focused on the research scope that can be done in future.

In chapter **3**, we have presented the synthesis of a series of novel 'B' site doped $LaMnO_3$ (LMO), $LaMn_{1-x}Ru_xO_3$ (x = 0.0 – 0.4) compounds and their use as a photocatalyst for water oxidation as well as dye degradation. Powder X-ray diffraction (PXRD) analysis indicate that the doped compounds have both rhombohedral and cubic phases. Rietveld refinement studies of the PXRD patterns of the compounds confirm the presence of both rhombohedral and cubic phases and reduction of lattice distortion as well increase in Mn–O–Mn bond angle to 180° with a progressive increase in ruthenium doping, which helps in the increased charge carrier movement of the catalysts. Variations in band gap, as well as different redox reactions taking place due to doping are studied. $LaMn_{0.7}Ru_{0.3}O_3$ having lowest bandgap among all the synthesized catalysts and consisting of 80% cubic and 20% rhombohedral phase, shows the highest efficiency of oxygen production (at a rate of 4.73 mmol/h/g) with an AQY of 7.43 % and methyl orange (MO) dye degradation.

In chapter **4**, we have reported the synthesis of stable and robust novel 'A' site doped $LaMnO_3$ (LMO), $La_{1-x}Sr_xMnO_3$ (x = 0.0 – 0.5) and its graphene oxide (GO) composites, $La_{1-x}Sr_xMnO_3$ (x = 0.0 – 0.5) – GO and its use as a photocatalyst for water oxidation. Sr doping in LMO creates holes or Mn (IV) in $La_{1-x}Sr_xMnO_3$ (x = 0.0 – 0.5) lattice. Owing to doping of larger Sr ions in La site, the crystal phase of $La_{1-x}Sr_xMnO_3$ (x = 0.0 – 0.5) changes from rhombohedral to cubic in higher Sr doping concentration and thereby makes the Mn–O–Mn angle ~180° in doped compounds. Formation of holes or Mn (IV) and ~180° of Mn–O–Mn bond angle facilitates the charge transport in these compounds. As $La_{0.7}Sr_{0.3}MnO_3$ photocatalyst has lowest resistivity among all $La_{1-x}Sr_xMnO_3$ (x = 0.0 – 0.5) photocatalysts, it gives highest amount of O_2 evolution from water oxidation (3.398 mmol/h/g, AQY ~ 7.2%). A blending of GO with $La_{1-x}Sr_xMnO_3$ (x = 0.0 – 0.5) shows further enhancement in photocatalytic O_2 evolution from water due to the good charge carrier transport property of GO and $La_{0.7}Sr_{0.3}MnO_3$ – GO shows highest photocatalytic activity in oxygen production at a rate of 3.707 mmol/h/g with ~ 8% of AQY.

In chapter **5**, $BaZrO_{3-\delta}$ (BZO) and Ce doped BZO hollow nanospheres have been successfully synthesized using a low-temperature template-free hydrothermal method. All the compounds show cubic phase with a high range of crystallinity. The as-synthesized compounds produced hydrogen upon illumination without any co-catalysts but in the presence of sacrificial donor reagents. As found from UV-Vis DRS, XPS and ESR analysis, the presence of disordered lattice, oxygen vacancies and cerium doping play a critical role in enhancing the photocatalytic activity in the ultraviolet-visible region. $BaZr_{0.97}Ce_{0.03}O_3$ among all the as-synthesized compounds, $BaZr_{1-x}Ce_xO_3$ (x = 0.00 – 0.04), shows the highest efficiency in hydrogen gas production concomitant with oxidation of a sacrificial donor.

In chapter **6**, we have synthesized $BaZrO_{3-\delta}$ (BZO) and carbon dots (CDs) by facile hydrothermal synthesis. 1 – 4 wt% of C_BZO hybrid catalysts are synthesized by dispersing CDs and BZO together. The synthesized products are found to be the efficient catalyst for photocatalytic H_2 production and methylene blue dye degradation. Synthesized samples were analyzed with the help of several analytical techniques and found that presence of defect states, oxygen vacancies and the addition of CDs onto BZO leads to an increment of visible light absorption by the photocatalysts and owing to the high charge transfer rate of CDs, the photogenerated charge carrier recombination is reduced. We have observed that 3 wt% CDs loaded onto BZO shows the highest efficiency in both photocatalytic H_2 production and MB dye degradation. The AQY of 3C_BZO (~4%) is doubled than that of the BZO (~2%). In brief, this work proves that CDs can considerably enhance the photocatalytic activity of a wide band gap material such as BZO that provides a facile scheme to develop hybrid materials that could be utilized in energy harvesting and environmental renovation.

From our aforementioned findings, we have found that manganite based perovskite oxides are superior photocatalyst than zirconium based perovskite oxides in terms of water oxidation owing to their small band gap and suitable band positions. On the other hand, zirconium based perovskite oxides are capable of both water oxidation and reduction and act as overall water splitting photocatalyst. Hence, in terms of photocatalytic oxygen production from water, which is indeed “bottleneck” of photocatalytic hydrogen evolution efficiency from water, manganite based perovskite oxides are certainly promising candidate whereas, in terms of future environmentally benign energy carrier production (H_2), zirconium based perovskite oxides are only capable among these two different types of perovskite oxides.

Future prospects:

A good number of research findings are obtained from this thesis in terms of preparation, characterization and photocatalytic applications. The photocatalysts studied in this thesis are mainly synthesized via two well-known routes, such as solid-state synthesis and hydrothermal routes. Although, all these materials are synthesized and studied in laboratory scale but they can easily be utilized in large-scale processes with redesigned photoreactor setup. As solid state synthesis route is commercially viable for large scale production of desired compounds, BZO and doped BZO can also be synthesized in this route.

Indeed, in this field many areas merit further extensive research attention. Few research areas for future work base on our investigations are presented as follows:

- To modulate the electronic structure and enhance catalytic activity, different transition metals or non-metals can be doped either in 'A' or 'B' sites or two different elements simultaneously in both 'A' and 'B' sites of LMO and BZO
- Based on the band positions and nature of the materials (p or n type), to enhance charge separation and light absorption, other semiconductors can be coupled with LMO and BZO
- LMO and BZO could be used in either Z-scheme water splitting systems with suitable band structured materials or making suitable solid solution with other semiconductors for enhanced photocatalytic efficacy
- Enhanced photocatalytic activity of LMO and BZO can be attained by incorporating different O_2 and H_2 evolution co-catalysts
- The role of lattice disorder and different vacancies in perovskite oxides in photocatalytic application can be studies in-depth by the help of theoretical calculations, XPS and X-ray absorption fine structure (XAFS) techniques
- Apart from photocatalytic water oxidation and/reduction application, these materials can be used in photoelectrochemical water oxidation/reduction systems, fuel cells etc.

LIST OF PUBLICATIONS
AND
CONFERENCES ATTENDED

Journal Articles

(1). Highly Efficient One-Dimensional ZnO Nanowire Based Dye-Sensitized Solar Cells using a Metal-Free D-π-A Type, Carbazole Derivative with more than 5% Power Conversion. Barpuzary, D.; **Patra, A. S**.; Vaghasiya, J. V.; Solanki, B. J.; Soni, S. S.; Qureshi, M. *ACS Appl. Mater. Interfaces* **2014**, *6*, 12629.

(2). Strontium Doped Lanthanum Manganites for Efficient and Robust Photocatalytic Water Oxidation Coupled with Graphene Oxide. **Patra, A. S.**; Vinothkumar, N.; Barpuzary, D.; De, M.; Qureshi, M. *Mater. Lett.* **2014**, *131*, 125.

(3). Modulating the Electronic Structure of Lanthanum Manganite by Ruthenium Doping for Enhanced Photocatalytic Water Oxidation. **Patra, A. S.**; Gogoi, G.; Sahu, R. K.; Qureshi, M. *Phys. Chem. Phys. Chem.* **2017**, *19*, 12167.

(4). Efficient Charge Transfer in a Noble-Metal-Free-Hybrid of g-C_3N_4 and MoS_2 Integrated onto $Cd_{0.5}Zn_{0.5}S$ for Enhanced Photocatalytic Activity. Gogoi, G.; Keene, S.; **Patra, A. S.**; Sahu, T. K.; Ardo, S.; Qureshi, M. *ACS Sustainable Chem. Eng.* **2018**, *6*, 6718.

(5). Synergistic Effect of Cerium Doping and Oxygen Vacancies in Photocatalytic Hydrogen Production Efficiency of $BaZrO_{3-\delta}$ Hollow Nanospheres. **Patra, A. S.**; Keene, S.; Gogoi, G.; Ardo, S.; Qureshi, M. (*Manuscript under communication*)

(6). Carbon Dot Modified $BaZrO_{3-\delta}$ Hollow Nanospheres for Enhanced Photocatalytic Activity. **Patra, A. S.**; Gogoi, G.; Qureshi, M. (*Manuscript under communication*)

Conferences Attended

(1). National Conference on Frontiers in Chemical Sciences (**FICS-2014**), 4-6 December, 2014, Indian Institute of Technology Guwahati, Guwahati, India (Poster presented).

(2). 4th International Conference on Advanced Nanomaterials and Nanotechnology (**ICANN-2015**), 8-11 December, 2015, Indian Institute of Technology Guwahati, Guwahati, India (Attended).

(3). International Conference on Advances in Nanomaterials and Nanotechnology (**ICANN-2016**), 4-5 November, 2016, Jamia Millia Islamia, New Delhi, India (Poster presented).

(4). National Conference on Frontiers in Chemical Sciences (**FICS-2016**), 8-10 December, 2016, Indian Institute of Technology Guwahati, Guwahati, India (Poster presented).

(5). International Conference on Sophisticated Instruments in Modern Research (**ICSIMR-2017**), 30th June-1st July, 2017, Indian Institute of Technology Guwahati, Guwahati, India (Oral presentation).

(6). 5th International Conference on Advanced Nanomaterials and Nanotechnology (**ICANN-2017**), 18-21 December, 2017, Indian Institute of Technology Guwahati, Guwahati, India (Poster presented).

(7). Conference on Advances in Catalysis for Energy and Environment (**CACEE-2018**), 10-12 January, 2018, Tata Institute of Fundamental Research (TIFR), Mumbai, India (Poster presented).